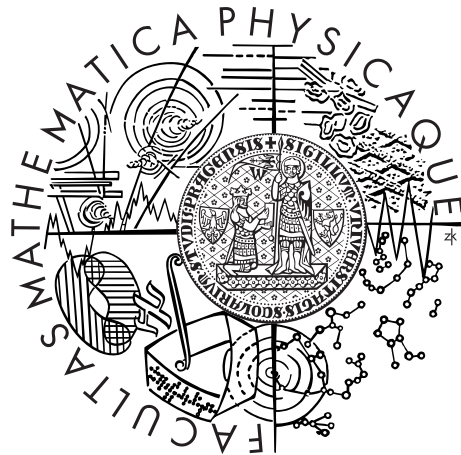


Charles University in Prague
Faculty of Mathematics and Physics

DOCTORAL THESIS



RNDr. Michaela Poková

Microstructure and properties of enhanced twin-roll cast aluminium alloys

Department of Physics of Materials

Supervisor: Doc. RNDr. Miroslav Cieslar, CSc.

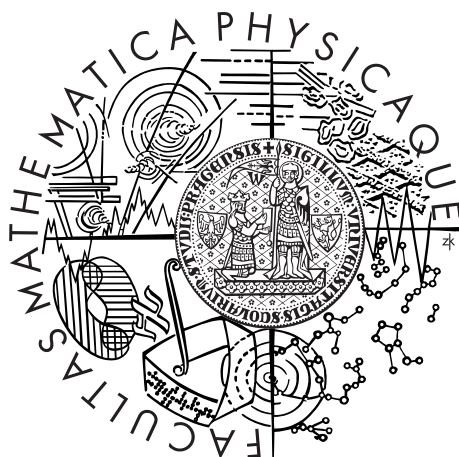
Study programme: Physics

Specialization: Physics of Condensed Matter and Materials Research

Prague 2014

Univerzita Karlova v Praze
Matematicko-fyzikální fakulta

DISERTAČNÍ PRÁCE



RNDr. Michaela Poková

Mikrostruktura a vlastnosti moderních plynule odlévaných hliníkových slitin

Katedra fyziky materiálů

Školitel: Doc. RNDr. Miroslav Cieslar, CSc.

Studijní program: Fyzika

Studijní obor: Fyzika kondenzovaných látek a materiálový výzkum

Praha 2014

Na tomto místě děkuji především mému školiteli Miroslavu Cieslarovi za rady, náměty a pomoc při vypracovávání této práce i prací minulých. Dále Janě Kálalové a Martě Čepové za pomoc v chemické laboratoři, Pavlu Beranovi za pomoc při ECAPování vzorků a Přemyslu Málkovi za provedení tahových zkoušek.

Dále děkuji mým rodičům a dalším členům rodiny za podporu ve studiu a Martinu Šlapákovi za podporu a pomoc s technickými problémy.

V neposlední řadě také děkuji všem spolužákům za cenné rady a společnost na konferencích při prezentování výsledků.

Firmě AL Invest Břidličná, a.s. děkuji za dodání všech studovaných slitin a za poskytnutí stipendia.

Furthermore, I would like to thank to Ladislava Mansfeldová and Jaroslav Izavčuk who taught me English at grammar school.

Finalement, je voudrais remercier Jacques Lacaze, qui supervisait mon thèse pendant mes études en France et Koenraad Theuwissen, Roxana Ghergu and Mariana Morcoana, mes collègues de la laboratoire et également Rami Hamdan, qui ont fait mon séjour en Toulouse plus agréable.

Je remercie l'Ambassade de France en République Tchèque pour la bourse pour effectuer mes études en Université de Toulouse.

Děkuji vám.

Thank you.

Merci beaucoup á tous.

I declare that I carried out this doctoral thesis independently, and only with the cited sources, literature and other professional sources.

I understand that my work relates to the rights and obligations under the Act No. 121/2000 Coll., the Copyright Act, as amended, in particular the fact that the Charles University in Prague has the right to conclude a license agreement on the use of this work as a school work pursuant to Section 60 paragraph 1 of the Copyright Act.

Prohlašuji, že jsem tuto disertační práci vypracovala samostatně a výhradně s použitím citovaných pramenů, literatury a dalších odborných zdrojů.

Beru na vědomí, že se na moji práci vztahují práva a povinnosti vyplývající ze zákona č. 121/2000 Sb., autorského zákona v platném znění, zejména skutečnost, že Univerzita Karlova v Praze má právo na uzavření licenční smlouvy o užití této práce jako školního díla podle §60 odst. 1 autorského zákona.

In Prague, 22th July 2014

RNDr. Michaela Poková

Název práce: Mikrostruktura a vlastnosti moderních plynule odlévaných hliníkových slitin

Autor: RNDr. Michaela Poková

Katedra: Katedra fyziky materiálů

Školitel: Doc. RNDr. Miroslav Cieslar, CSc., Katedra fyziky materiálů

Abstrakt: V této práci byly studovány tři hliníkové slitiny ze série AA3003 modifikované přídavkem zirkonia. Byl vyhodnocen vliv složení, tepelného zpracování a deformace válcováním za studena nebo protlačováním pravouhlým kanálem na vývoj mikrostruktury a mechanických vlastností. Během žíhání při teplotách 300 °C až 500 °C se v materiálech vytvořilo velké množství precipitátů fáze α -Al(Mn,Fe)Si. Částice fáze Al_3Zr vyprecipitovaly během žíhání na teplotě 450 °C s pomalým náběhem. Odolnost vůči rekrystalizaci byla zvýšena buď částicemi Al_3Zr , které byly v materiálu přítomné před deformací, nebo částicemi fáze α -Al(Mn,Fe)Si, které se tvořily současně během rekrystalizace.

Klíčová slova: Hliníkové slitiny, elektronová mikroskopie, precipitace, rekrystalizace, ECAP

Title: Microstructure and properties of enhanced twin-roll cast aluminium alloys

Author: RNDr. Michaela Poková

Department: Department of Physics of Materials

Supervisor: Doc. RNDr. Miroslav Cieslar, CSc., Department of Physics of Materials

Abstract: Three aluminium alloys from AA3003 series modified by zirconium were prepared by twin-roll casting. The role of composition, heat treatment and deformation by cold-rolling or equal channel angular pressing on evolution of microstructure and mechanical properties were studied. High density of α -Al(Mn,Fe)Si precipitates formed during annealing between 300 °C and 500 °C. Coherent Al_3Zr particles precipitated during annealing at 450 °C with slow heating rate. Recrystallization resistance of deformed alloys was enhanced by either Al_3Zr precipitates formed before deformation or by α -Al(Mn,Fe)Si particles nucleating simultaneously with recrystallization.

Keywords: Aluminium Alloys, Electron Microscopy, Precipitation, Recrystallization, ECAP

Contents

I	Introduction	5
1	Literature review	9
1.1	Aluminium alloys	9
1.1.1	Manganese	9
1.1.2	Iron	9
1.1.3	Silicon	11
1.1.4	Al-Mn-Fe-Si	11
1.1.5	AA3003 alloy	12
1.2	Heat treatment	14
1.2.1	Primary particles transformation	14
1.2.2	Precipitation	19
1.2.3	Homogenization	22
1.3	Recrystallization	24
1.3.1	Grain boundaries	24
1.3.2	Recrystallization and grain growth	25
1.3.3	Experimental data	28
1.4	Zirconium	30
1.5	Chromium	33
1.6	Twin-roll casting	34
1.7	Equal channel angular pressing	37
1.7.1	ECAP process	37
1.7.2	Pure aluminium	38
1.7.3	Aluminium alloys	39
1.7.4	Annealing	41
1.7.5	Superplasticity	42
2	Materials	45
2.1	Studied materials	45
2.2	Equal channel angular pressing	45
3	Experimental	47
3.1	Heat treatment	47
3.2	Electrical resistivity	47
3.3	Differential thermal analysis	48
3.4	Microhardness	50
3.5	Tensile tests	50
3.6	Light optical microscopy	50
3.7	Scanning electron microscopy	50
3.8	Transmission electron microscopy	51
II	Material characterization	53
4	Electrical Resistivity	55

5	Differential thermal analysis	57
5.1	Heating rate 10 K/min	57
5.2	Heating rate 5 K/min	57
5.3	Heating rate 1 K/min	58
5.4	Influence of heating rate	58
5.5	DTA vs. electrical resistivity	58
6	Vickers Microhardness	61
6.1	Initial states	61
6.2	Isochronal annealing	61
7	Light optical microscopy	63
7.1	Phases	63
7.2	Grains	65
8	Scanning electron microscopy	67
8.1	Back-scattered electrons	67
8.2	Chemical analysis	69
8.3	Electron back-scatter diffraction	71
8.3.1	Phases	71
8.3.2	Grains	71
9	Transmission electron microscopy	77
9.1	Initial states	77
9.2	Annealing	77
9.3	In-situ heating	79
10	Discussion	81
III	Zirconium addition	83
11	Two-step annealing	85
12	One-step annealing	87
12.1	Mechanical properties	87
12.2	Microstructure	87
13	Discussion	91
IV	Equal channel angular pressing	93
14	Equal channel angular pressing	95
14.1	Processing	95
14.2	Mechanical properties	95
14.3	Microstructure	96

15 Isochronal annealing	99
15.1 Vickers microhardness	99
15.2 Grain structure	99
15.3 Electrical resistivity	101
15.4 Transmission electron microscopy	103
15.4.1 In-situ annealing	103
15.4.2 Post-mortem observations	104
16 Isothermal annealing	107
16.1 Vickers Microhardness	107
16.2 Microstructure	107
17 High temperature deformation	111
17.1 Mechanical properties	111
17.2 Microstructure	111
18 Discussion	115
V Conclusion	121
19 Discusion	123
19.1 Precipitation	123
19.2 Recrystallization	123
19.3 Zirconium and chromium	124
20 Conclusion	125
A DVD content	137

Part I

Introduction

To minimise the impact of human activities on the environment and reduce the cost of constructions, recent aim is to decrease the size and weight of system components. Search for new metallic materials with higher strength, formability, better heat and creep resistance and produced by energy saving methods still continues.

Twin-roll casting is a casting method which provides high solidification rate and produces highly supersaturated materials with better mechanical properties.

Further strength increase may be achieved by the reduction of the grain size. Severe plastic deformation leads to production of materials with submicron grain size which exhibit higher strength at lower temperatures and better formability at elevated temperatures, resulting often in superplasticity. Equal channel angular pressing can be used for production of relatively large pieces of ultra-fine grained bulk materials.

Zirconium is added to aluminium alloys in order to postpone recovery and recrystallization processes. Dense dispersion of coherent Al_3Zr particles can retard movement of lattice dislocations and grain boundaries and contribute to better stability of the microstructure at elevated temperatures.

In the present study three materials based on the AA3003 type alloy prepared by twin-roll casting are studied. The precipitation processes of Al-Mn-Fe-Si phases during isochronal annealing are investigated and the optimal conditions for Al_3Zr particles formation are sought. Afterwards, materials are subjected to equal channel angular pressing, their thermal stability at elevated temperatures is evaluated and high temperature deformation is tested.

Lets go and explore the "Path of Aluminium"!



Figure 1: "Chemin de l'Aluminium" in Arcachon, France.

1. Literature review

1.1 Aluminium alloys

Thanks to the low density and good strength, formability, thermal conductivity, corrosion resistance, weldability, recyclability etc., aluminium and its alloys belong to the most widely used materials in many branches of industry, mainly aircraft, automobile and food industry. Basic physical properties of pure aluminium are listed in Table 1.1 and its FCC crystal lattice is depicted in Figure 1.1.

According to the norm EN 573-3 aluminium alloys are labeled with four numbers, first of them corresponding to the main alloying element. List of the alloy groups is given in Table 1.2. The role of manganese, iron and silicon are described further.

1.1.1 Manganese

Manganese is the main alloying element in alloys of the 3XXX series.

Manganese in combination with aluminium forms eutectic binary alloy with eutectic temperature $T_e = 660$ °C and eutectic concentration $c_e = 1.9$ wt.% Mn. The equilibrium intermetallic phases in this system are Al_6Mn (1.9-4.1 % Mn) and Al_4Mn . Metastable phase Al_{12}Mn is stabilized by addition of Cr and its formation is suppressed by iron and silicon.

Alloys with more than 1 wt.% Mn are considered as non-heat treatable. In general, Mn increases strength of wrought alloys by solution and dispersion hardening at both room and elevated temperatures, but decreases ductility if present as undissolved intermetallic compound. Moreover, it reduces susceptibility to intergranular and stress corrosion [1], improves tensile strength elongation, high temperature strength, weldability, ductility and creep resistance and increases recrystallization temperature. When dissolved in the aluminium matrix, it influences resistivity more strongly than iron and silicon.

Diffusion coefficient of Mn in aluminium at 500 °C is $1 \cdot 10^{-16}$ m²/s [4] and its specific contribution to electrical resistivity is $5.97 \mu\Omega\text{cm/at.}\%$ [5]. Its contribution to microhardness is 13.4 HV/wt.% if dissolved in solid solution [6].

In pure Al-Mn alloys decomposition of supersaturated solid solution is very sluggish and can be sped up by addition of iron or silicon, as they decrease solubility of manganese in aluminium.

Manganese reduces negative effect of iron via modification of morphology and type of intermetallic phases in the matrix.

1.1.2 Iron

Iron is the most common impurity in all commercial aluminium alloys. It forms an eutectic phase diagram with aluminium with $T_e = 655$ °C and $c_e = 2.2$ wt.%. Its solubility in Al is very low: 0.052 wt.% and, thus, in aluminium alloys it is present in a form of intermetallic phases. The equilibrium ones are Al_3Fe with 40.7 wt.% Fe and Al_7Fe_2 (37.3 wt.% Fe). In rapidly cooled alloys metastable phase Al_6Fe can be found [1].

Table 1.1: Basic properties of pure aluminium [1, 2].

Atomic number	13
Atomic weight	26.98
Electron configuration	$1s^2 2s^2 2p^6 3s^2 3p^1$
Stable isotope	^{27}Al
Bravais lattice	Face-centered cubic (FCC)
Atoms in unit cell	4
Lattice constant	$4.049596 \cdot 10^{-10}$ m
Atomic diameter	$2.86 \cdot 10^{-10}$ m
Density (solid)	2697.72 kg/m ³
Density (liquid)	2350 kg/m ³
Melting point	933.47 K, 660.32 °C
Boiling point	2767 K, 2519 °C
Coefficient of expansion	$23 \cdot 10^{-6}$ K ⁻¹
Thermal conductivity	237 W/mK
Electrical resistivity	$2.6548 \cdot 10^{-8}$ Ωm
Heat of fusion	397 J/g
Heat capacity	0.9 J/gK
R _{p0.2}	150 MPa
Young's modulus	70.7 GPa
Shear modulus	26.4 GPa

Table 1.2: Division of aluminium alloys by the main alloying elements [2].

Designation by norm EN 573-3	Major alloying element
1XXX	Pure Al, min. 99.0 %
2XXX	Cu
3XXX	Mn
4XXX	Si
5XXX	Mg
6XXX	Mg, Si
7XXX	Zn
8XXX	others

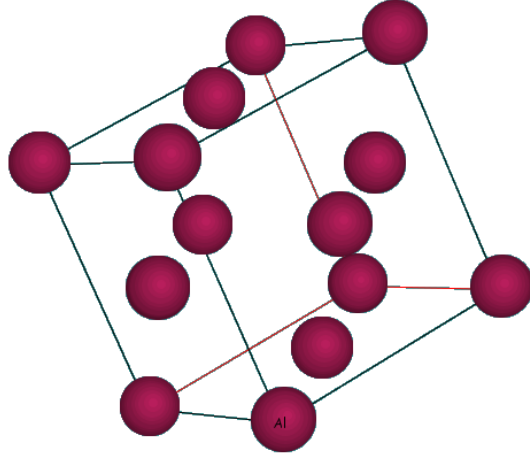


Figure 1.1: Face-centred cubic structure of aluminium [3].

At higher concentrations iron degrades mechanical properties like corrosion resistance and brittleness.

Specific contribution of iron to electrical resistivity of aluminium was measured as $5.30 \mu\Omega\text{cm/at.}\%$ [5]. Its contribution to microhardness if dissolved in solid solution reported in [6] is $4.16 \text{ HV/wt.}\%$.

1.1.3 Silicon

Silicon is another impurity commonly present in aluminium. It forms a simple eutectic phase diagram with Al with eutectic temperature $580 \text{ }^\circ\text{C}$ and concentration $12.5 \text{ wt.}\%$ Si. The maximal solid solubility of Si in Al is $1.65 \text{ wt.}\%$. It does not form any intermetallic phase with Al. Commercial importance of Al-Si alloys is based on low shrinkage and high fluidity in casting, welding and brazing applications [1].

Diffusion coefficient of Si in aluminium at $500 \text{ }^\circ\text{C}$ is $1.4 \cdot 10^{-13} \text{ m}^2/\text{s}$ [4] and specific contribution to electrical resistivity is $0.65 \mu\Omega\text{cm/at.}\%$ [5]. According to Pettersen et. al. [7] silicon does not have strong influence on conductivity in the as-cast state.

Silicon in solid solution has higher hardening effect than iron [8], which is in correspondance to its higher solubility. According to [6], its contribution to microhardness is $13.4 \text{ HV/wt.}\%$ if dissolved in solid solution.

Increasing the silicon content in aluminium alloys strongly increases the solidification interval, but it also gives a finer structure.

1.1.4 Al-Mn-Fe-Si

Several different phases were reported in quaternary system Al-Mn-Fe-Si [9]. The most common are $\text{Al}_6(\text{Mn,Fe})$ and $\text{Al}_{15}\text{Mn}_3\text{Si}_2$.

The phase $\text{Al}_6(\text{Mn,Fe})$ has an orthorhombic crystal structure with parameters $a = 0.7498 \text{ nm}$, $b = 0.6495 \text{ nm}$, $c = 0.8837 \text{ nm}$ and is isomorphic to the Al_6Fe and Al_6Mn phases. Manganese substitutes for iron in the Al_6Fe up to $\text{Al}_{12}\text{MnFe}$ (12.8% Fe, 12.6% Mn).

A broad range of solid solutions based on the compound $\text{Al}_{15}\text{Mn}_3\text{Si}_2$ exists [9]. Iron can be substituted for manganese in the ternary compound to the composition 31 % Fe, 1.5 % Mn, 8 % Si and the broad region of homogeneity is treated as formation of quaternary phase $\text{Al}_{15}(\text{Mn,Fe})_3\text{Si}_2$.

Solid solution of iron in $\text{Al}_{15}\text{Mn}_3\text{Si}_2$ phase has a cubic structure with lattice parameter a from 1.252 nm for 0 % Fe to 1.25 nm for 31.1 % Fe.

However, some studies support theory given by Mondolfo [10], that no quaternary compound is present in Al-Fe-Mn-Si phase diagram, but there is a wide range of the $\text{Al}_{15}(\text{Mn,Fe})_3\text{Si}_2$ phase [11].

The solubility of manganese in (Al) in the as-cast state decreases with the increasing Fe and Si concentrations and a significant part of it is bound in the $\text{Al}_{15}(\text{Mn,Fe})_3\text{Si}_2$ phase during solidification.

The effect of temperature on the structure of an alloy is determined by the ratio between the equilibrium and non-equilibrium solubilities in solid aluminium, which depends on the alloy composition and cooling rate. The non-equilibrium concentration of manganese in (Al) in the as-cast state determines the amount of dispersoids formed during annealing at temperatures above 300-350 °C.

1.1.5 AA3003 alloy

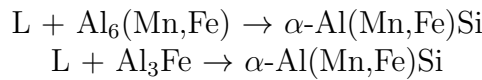
Aluminium-manganese alloy AA3003 is commonly used as fins in automotive heat exchangers [12]. Its standard composition is given in Table 1.3.

Two main phases which are present in AA3003 series are cubic $\alpha\text{-Al}(\text{Mn,Fe})\text{Si}$ and orthorhombic $\text{Al}_6(\text{Mn,Fe})$. α -phase has higher hardness than $\text{Al}_6(\text{Mn,Fe})$ and is preferable for commercial applications due to its effect on galling resistance [4]. Which of these two phases is dominant depends mainly on the content of silicon and thermal history of the alloy. A summary of phases observed by different authors is given in Tables 1.4, 1.5, 1.6 and 1.7.

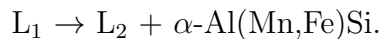
The exact structural formula of the $\alpha\text{-Al}(\text{Mn,Fe})\text{Si}$ differs in the literature sources and usually varies between $\text{Al}_{15}(\text{Mn,Fe})_3\text{Si}_2$ and $\text{Al}_{12}(\text{Mn,Fe})_2\text{Si}$. Several crystallographic phases were described – simple cubic, body-centered cubic and hexagonal. See Tables 1.4-1.7 for details.

The final composition of the particles is governed by diffusion of manganese, iron and silicon. Cooling rate determines initial crystallography, morphology and chemical composition of the phases [13].

α -phase can be product of a peritectic reaction from a liquid [14]:



or can be formed by nucleation and growth as an equilibrium phase from liquid



The phase composition of a AA3003 alloy can be analyzed using isothermal and polythermal sections of the Al-Mn-Si phase diagram. Due to high solubility of silicon in (Al), ternary compound $\text{Al}_{15}\text{Mn}_3\text{Si}_2$ can be formed both during solidification and also during annealing in a form of dispersoids.

At low temperatures, the AA3003 alloy can contain two- or three-phase regions involving phases Al_6Mn , $\text{Al}_{15}\text{Mn}_3\text{Si}_2$ and (Si).

Combined effects of all three alloying elements (Mn, Fe, Si) on the phase composition can be analyzed only by using quaternary phase diagram. Presence of iron and silicon usually leads to the formation of $\text{Al}_{15}(\text{Mn,Fe})_3\text{Si}_2$ phase.

Nonequilibrium solidification causes decrease in the solidus temperature. The as-cast structure contains $\text{Al}_6(\text{Mn,Fe})$ and $\text{Al}_{15}(\text{Mn,Fe})_3\text{Si}_2$ phases (amount of this phase increases with silicon concentration). High concentration of Si can lead to formation of free (Si) and decrease of solidus to 573 °C.

In rapidly cooled materials the $\alpha\text{-Al}(\text{Mn,Fe})\text{Si}$ phase is predominant as nucleation of $\text{Al}_6(\text{Mn,Fe})$ is suppressed [15].

Lower Si level in Al-Mn strips can change phase ratio in favour of $\text{Al}_6(\text{Mn,Fe})$ phase, which promotes particle simulated nucleation and, thus, may lead to fine-grained structure [15].

Petterson et. al. [7] studied mould cast AA3103 alloy and their work focused on the role of silicon. If the alloy contains 0.1 wt.% of silicon, 95 % of the particles present in the alloy after casting will be $\text{Al}_6(\text{Mn,Fe})$. With 0.3 wt.% of Si it will be 61 % of $\text{Al}_6(\text{Mn,Fe})$, 37 % of $\alpha\text{-Al}(\text{Mn,Fe})\text{Si}$ and the rest will be spherical intergranular Si-clusters and eutectic cell boundary Si-phase. 0.5 wt.% of silicon corresponds to 14 % of $\text{Al}_6(\text{Mn,Fe})$, 78 % of $\alpha\text{-Al}(\text{Mn,Fe})\text{Si}$ phase and 8 % of Si particles. Finally, in the alloy with 1 wt.% of Si 18 % of detected particles are Si and the rest are of $\alpha\text{-Al}(\text{Mn,Fe})\text{Si}$ phase. No $\text{Al}_6(\text{Mn,Fe})$ particles form in alloy with higher Si content.

The presence of iron in Al-Mn-Si alloys plays an important role in the precipitation process and influences final morphology of the particles. Warmuzek et. al. [16] observed in an Al-3Si-6Mn alloy change of the morphology from irregular profile to the chinese script with addition of 0.5 wt.% of iron and to polyhedra with 2 wt.% of iron. If an alloy contains more than 0.2 wt.% of iron, it will exhibit high density of coarse particles in whose vicinity fine secondary precipitates may be absent [8].

Regarding Mn:Fe ratio in primary particles and precipitates, it increases with homogenization time as Mn-rich precipitates dissolve and manganese deposits on primary particles [17]; iron concentration in intermetallic phases is higher at lower annealing temperatures [16]. Content of manganese is lower in primary particles than in precipitates [17].

The structure of $\alpha\text{-Al}(\text{Mn,Fe})\text{Si}$ depends on the Mn:Fe ratio. It has been found that with the increasing ratio, particles transform from body-centered cubic Im3 to simple cubic Pm3 [18]. In the work of Li et. al. [19] it was also measured by EDS, that the Mn:Fe ratio in dispersoids is very high at low temperatures and decreases with increasing temperature: 18.5 at 500 °C, 3.8 at 550 °C and 2.5 at 600 °C. The situation in the primary particles is opposite, the ratio increases from 0.57 at the room temperature to 0.59 at 600 °C. This implies that diffusion of manganese from Mn-rich dispersoids to Fe-rich primary particles occurs.

After seven hours of homogenization at 600 °C the Mn:Fe ratio drops in the precipitates from 2.5 to 1.7 and grows from 0.59 to 0.79 in the primary particles. The structure of some precipitates changes from simple cubic to body-centered cubic [19].

As annealing temperature increases, the amount of Mn increases and of Fe decreases in the $\text{Al}_6(\text{Mn,Fe})$ particles. On the contrary, in the $\alpha\text{-Al}(\text{Mn,Fe})\text{Si}$ particles the amount of Fe increases with the temperature and the Mn content

Table 1.3: Composition of commercial AA3003 alloy

AA3003	Mn	Fe	Si	Cu	Zn
[wt.%]	1.0-1.5	≤ 0.7	≤ 0.6	0.05-0.2	≤ 0.2

decreases [13].

Dehmas et. al. [20] also reported, that in the $\text{Al}_6(\text{Mn,Fe})$ particles the iron content lowers during annealing with holding time on the expense of manganese. After a short-time annealing, the iron concentration in $\text{Al}_6(\text{Mn,Fe})$ particles is high; after approximately two days at elevated temperature the iron and manganese concentrations are balanced. The transfer of iron is quicker at higher temperatures.

Regarding $\alpha\text{-Al}(\text{Mn,Fe})\text{Si}$ particles, the silicon amount does not change during heat treatment as the diffusivity of Si in aluminium is high and the equilibrium can be reached after a short time [20].

1.2 Heat treatment

After solidification aluminium matrix may be in a non-equilibrium state and phase transformations may take place during heat treatment. Two main processes in AA3003 alloys are primary phases transformation and precipitation of new secondary particles.

1.2.1 Primary particles transformation

Primary particles are those second phase particles, which are present in the matrix right after casting and solidification, without further heat treatment. They usually form interdendritic eutectic networks.

When subjected to heat treatment, some primary particles may increase their size, spheroidize, or non-equilibrium interdendritic eutectics may dissolve [13, 20].

During heat treatment composition of primary particles changes and some of them may transform from one phase to another. One example of such transformation is "6-to- α " transformation from $\text{Al}_6(\text{Mn,Fe})$ to $\alpha\text{-Al}_{15}(\text{Mn,Fe})_3\text{Si}_2$ [21]. According to Li et. al. [17] $\text{Al}_6(\text{Mn,Fe})$ particles appear darker in a light microscope than $\alpha\text{-Al}_{15}(\text{Mn,Fe})_3\text{Si}_2$ and the transformation starts around 400 °C. If we compare the data from other authors (Table 1.8), we can conclude that the temperature of the transformation depends on alloy composition and on heating rate.

As shown by Dehmas et. al. [26], temperature of the transformation depends on the heating rate: during heating at 20 K/min no transformation was detected, at 1 K/min it started around 475 °C.

The formation of the α -phase is promoted by augmented concentration of silicon or by shortening of diffusion path [13, 28].

During the transformation α -phase nucleates at the interface between the aluminium matrix and an $\text{Al}_6(\text{Mn,Fe})$ particle and then grows through the $\text{Al}_6(\text{Mn,Fe})$ particles as an eutectoid reaction front without presence of any intermediate phase; thus it forms a duplex particle [20, 28]. Warmuzek et. al. [13] observed

Table 1.4: Phases in AlMn alloys I.

Phase	Structure	Alloy	Mn	Fe	Si	Mg	State	Reference
(Si)								
$Al_{12-15}(Mn,Fe)_3Si_{1-2}$			1.0	0.32	0.62		TRC, CR	Cieslar et. al. [21]
$Al_{12-15}(Mn,Fe)_3Si_{1-2}$ $Al_6(Mn,Fe)$			1.1	0.32	0.11		TRC, CR	Cieslar et. al. [21]
$Al_{15}(Mn,Fe)_3Si_2$ Al_8Fe_2Si	cubic hexagonal	3003	0.9	0.6	0.5		TRC, CR	Cieslar et. al. [22]
$Al_{15}(Mn,Fe)_3Si_2$ $Al_6(Mn,Fe)$	cubic orthorhombic	3003	0.9	0.6	0.1		TRC, CR	Cieslar et. al. [22]
$Al_6(Mn,Fe)$		3003	1.15	0.58	0.20		DC	Li et. al. [17, 23]
$Al_{15}(Mn,Fe)_3Si_2$								
$Al_{15}(Mn,Fe)_3Si_2$ β - $Al_{15}(Mn,Fe,Cr)Si$	BCC		0-0.5	0.4-1.2	12.7			Shabestari [24]
$Al_6(Mn,Fe)$		3XXX	1.0	0.5	0.2		DC	Alexander et. al. [4]
$Al_{15}(Mn,Fe)_3Si_2$								
$Al_6(Mn,Fe)$	orthorhombic	3003	1.18	0.58	0.2		rod	Dehmas et. al. [5]
α - $Al(Mn,Fe)Si$	SC Pm3							
$Al_{12}(Mn,Fe)_2Si$ $Al_6(Mn,Fe)$	cubic orthorombic		1.10	0.32	0.13		TRC	Karlık et. al. [8, 25]
$Al_{12}(Mn,Fe)_2Si$ $Al_{15}(Mn,Fe)_3Si_2$	cubic hexagonal		1.06	0.18	0.49		TRC	Karlık et. al. [8, 25]
$Al_6(Mn,Fe)$		AA3003					rod	Dehmas et. al. [26]
α - $Al(Mn,Fe)Si$								
α - $Al(Mn,Fe)Si$ $Al_6(Mn,Fe)$			1.59	0.29	0.09		CR, 400 °C	Hansen et. al. [27]
quasi-crystalline	icosahedral							
$Al_{12-13}(Mn,Fe)_3Si_{1,2-2}$	BCC, SC	AA3003	1.15	0.58	0.20		DC	Li et. al. [19]

Table 1.5: Phases in AlMn alloys II.

Phase	Structure	Alloy	Mn	Fe	Si	Mg	State	Reference
Al ₆ (Mn, Fe) Mg ₂ Si	orthorombic	3004	0.9, 1.12	0.5	0.3, 0.4	1.1	cast ingot	Sun et. al. [28]
Al ₁₂ (Mn, Fe) ₃ Si	Pm3 BCC <i>a</i> = 1.263 nm							
β -AlMnSi			6	0.5, 2	3		synthetic	Warmuzek et. al. [16]
α -Al(Mn, Fe)Si	incoherent	3003	1	0.6	0.2		TBCC ^a	Liu et. al. [29]
α -Al(Mn, Fe)Si Al ₆ (Mn, Fe)	Fe:Mn=2 primary orthorhombic precipitates		1.192	0.605	0.163		TBCC 3 mm	Birol [15]
α -Al(Mn, Fe)Si			0.471	1.658	0.260		TBCC 3 mm	Birol [30]
Al ₁₂ (Mn, Fe) ₃ Si	cubic	3003	1.192	0.605	0.163		TBCC 6 mm	Birol [31]
Al ₆ (Mn, Fe)			1.10	0.19	0.08			Tierce et. al. [32]
Al ₆ (Mn, Fe)			1.10	0.16	0.08			Lacaze et. al. [33]
α -Al(Mn, Fe)Si Al ₆ (Mn, Fe)	cubic orthorombic	AA 8006	0.4	1.5	0.16		TBCC, CR	Slánová et. al. [34, 35]
Al ₃ Fe	monoclinic							
Al ₆ Mn Al ₃ Mn		3003	0.944	0.353	0.222		450 °C/3 h	Khakbaz et. al. [36, 37]
Al ₆ Mn	spherical		1.0-1.6	0.7	0.6	0.05		Wei et. al. [38]
Al ₁₅ (Mn, Fe) ₃ Si ₂ Si	cubic <i>a</i> = 1.26 nm cubic <i>a</i> =0.543 nm	3003	0.90	0.53	0.50		TBCC	Veselý [39]
Al ₈ Fe ₂ Si Al ₁₅ (Mn, Fe) ₃ Si ₂ Al ₆ (Mn, Fe)	hexagonal <i>a</i> = 1.23 nm, <i>c</i> = 26.3 nm cubic <i>a</i> = 1.26 nm orth. <i>a</i> = 0.65 nm, <i>b</i> = 0.75 nm, <i>c</i> = 0.88 nm cubic <i>a</i> =0.543 nm	3003	0.86	0.61	0.10		TBCC	Veselý [39]
Si								

^aTBCC = twin-belt continuous cast

Table 1.6: Phases in AlMn alloys III.

Phase	Structure	Alloy	Mn	Fe	Si	Mg	State	Reference
$Al_{15}(Mn,Fe)_3Si_2$	$Im\bar{3}$ BCC $a = 1.25$ nm	3003	1.0-1.5	0.7	0.6		TRC, CR	Lukáš [40]
$Al_{15}(Mn,Fe)_3Si_2$	$Pm\bar{3}m$ SC $a = 1.25$ nm							
$Al_6(Mn,Fe)$	$CmCm$ $a = 0.76$ nm, $b = 0.65$ nm, $c = 0.89$ nm	8006	0.3-0.1	1.2-2.0	0.4		TRC, CR	Lukáš [40]
$Al_{15}(Mn,Fe)_3Si_2$	$Im\bar{3}$ BCC $a = 1.25$ nm							
$Al_{15}(Mn,Fe)_3Si_2$	$Pm\bar{3}m$ SC $a = 1.25$ nm							
Al_6Mn		1561	0.5	0.014	0.12	5.4	DC, 440 °C	Nikulín et. al. [41]
$Al_{19}(Mn,Fe)_5Si_2$	$Im\bar{3}$ $a = 1.256$ nm		0.13	0.16	11.7			Kral et. al. [42]
$Al_3(Mn,Fe)Si_2$	$I4/mcm$ $a = 0.607$ $c = 0.95$ nm							
$Al_{19}(Mn,Fe)_5Si_2$	$Im\bar{3}$ $a = 1.25$ nm	3003 + 4343						Dehmas et. al. [18]
$Al_3(Mn,Fe)Si_2$	$I4/mcm$ $a = 0.61$ $c = 0.95$ nm							
$Al_3(Mn,Fe)Si_2$	$Pbcn$ $a = 0.61$ $c = 0.95$ nm							
Al_4FeSi_2								
Al_6Fe				0.932	0.245		TRC	Biol [43]
$\alpha-Al_{12}Fe_3Si$							TRC, 560 °C	
$Al_6(Mn,Fe)$			0.97	0.53	0.152		DCC	Wang et. al. [44]
$\alpha-Al(Mn,Fe)Si$								
$Al_6(Mn,Fe)$			1.262	0.012	0.008		CR	Vlach et. al. [45]
$Al_6(Mn,Fe)$			1.25	0.48	0.14	0.019	DCC	Jaradeh et. al. [46]
$Al_{15}(Mn,Fe)_3Si_2$		3003						
$Al_6(Mn,Fe)$			1.69	0.209	0.58	0.002	DCC	Jaradeh et. al. [46]
$Al_{16}(Mn,Fe)_4Si_3$	FCC $a = 1.252 \pm 0.04$ nm		0-4	0-3	10-14			Zakharov et. al. [47]

Table 1.7: Phases in AlMn alloys IV.

Phase	Structure	Alloy	Mn	Fe	Si	Mg	State	Reference
Al ₆ (Mn,Fe)	Orthorombic BCC Im3		1.05	0.14	0.10		Strip cast	Warmuzek et. al. [13]
Al ₁₂ (Mn,Fe) ₃ Si								
Al ₁₉ (Mn,Fe) ₅ Si ₂								
Al ₆ (Mn,Fe)	cubic	AA 3105	0.40	0.55	0.25	0.60	TRC, CR	Gras et. al. [48]
α -Al(Mn,Fe)Si Mg ₂ Si								
α -Al ₁₂ Fe ₃ Si Al ₃ Fe	cubic			0.966	0.191		TRC	Biroi [49]
Al ₁₅ (Mn,Fe) ₃ Si ₂	BCC		2.0	4.0	6.0		Chill cast	Gao et. al. [50]
α -Al(Mn,Fe)Si	cubic	3xxx	0.99	0.50	0.48		DC	Muggerud et. al. [51]
α -Al(Mn,Fe)Si		AA3003	1.27	0.54	0.1			Chen et. al. [52]
Al ₆ (Fe,Mn)								
α -AlMnSi	cubic	3xxx	1.5		0.8		TRC	Yoshino et. al. [53]
AlMnSi		AA3xxx	1.5	0.19-0.50	0.06-0.40	0.1		
AlMnFeSi								
α -Al ₁₂ Fe ₃ Si		3003	1.09	0.5	0.1			Huang et. al. [55]
Al ₆ (Fe,Mn)								
Al(Fe,Mn)Si		3003	1.19	0.56	0.28			Wu et. al. [56]
Al ₆ (Fe,Mn)								
Al ₆ (Mn,Fe)			1.47	0.056	0.025		ingot cast, 18 h/610 °C	Očenašek [57]
Al(Mn,Fe,Si)								
Al ₆ (Mn,Fe)		5083	0.65	0.20	0.14	4.62		Sato et. al. [58]

that a layer of α -phase forms at the matrix/ $\text{Al}_6(\text{Mn,Fe})$ interface and due to diffusion of Si, Mn and Fe the structure gradually transforms. After the transformation, Al-spots may be present inside the α -phase particles [28].

The transformation can be described by a reaction



During α -to-6 transformation the α -phase inherits high amount of iron from $\text{Al}_6(\text{Mn,Fe})$ [20].

The transformation starts rapidly and volume fraction of the transformed α -phase x follows simple relaxation in time t [4]:

$$x = x_f - (x_f - x_0) \cdot \exp(-kt). \quad (1.1)$$

x_0 stands for initial and x_f for final fraction of the α -phase, k is constant.

During holding at constant temperature, the amount of α -phase in the matrix increases. This increment is very quick at the beginning of annealing and afterward it stabilizes. Dehmas et. al. [20] reported that the amount of the α -phase reaches its equilibrium after holding for 40 hours at 400 °C, 10 hours at 500 °C or 7 hours at 600 °C. The highest number density was observed at 500 °C; during annealing at 600 °C the diameter of the particles raises, but their density drops.

The α -to-6 transformation is affected by precipitation: due to precipitation the amount of silicon in the solid solution, which is necessary for the transformation, is reduced [20]. However, at higher temperatures the smaller precipitates dissolve back to the solid solution and newly freed silicon atoms may migrate to primary particles and increase the amount of the α -particles.

The transformation is slower in alloys with addition of Mg since Mg_2Si is a dominant phase and silicon is consumed for its formation [4].

Sun et. al. [59] studied the amount of α -phase and $\text{Al}_6(\text{Mn,Fe})$ particles during annealing in two 3004 alloys. In the initial state the alloy with higher manganese and lower silicon content (composition is given in the Table 1.5) contains 10 % of α -particles. In the second one, 20 % of the particles present in the material are the α -phase. After 5 hours at 595 °C the first alloy is composed of 75 % of α -phase, the second one of 90 %. Further annealing up to 20 hours increases the fraction of α -particles by 10 %, which means that in the alloy with lower manganese and higher silicon all particles are of the α -phase.

Birol [43] reported similar transformation Al_6Fe to $\text{Al}_{12}\text{Fe}_3\text{Si}$ between room temperature and 560 °C in alloy without Mn.

Vesely [39] also reported transformation from hexagonal $\text{Al}_8\text{Fe}_2\text{Si}$ to cubic $\text{Al}_{15}(\text{Mn,Fe})_3\text{Si}_2$ at temperature below 320 °C in an AA3003 alloy with low silicon content. Moreover, both primary particles and precipitates transformed during annealing to 620 °C from cubic $\text{Al}_{15}(\text{Mn,Fe})_3\text{Si}_2$ to orthorombic $\text{Al}_6(\text{Mn,Fe})$.

1.2.2 Precipitation

During heat treatment supersaturated solid solution decomposes and precipitates (sometimes called also secondary particles) nucleate in the matrix.

Precipitates of suitable size and separation formed during processing can pin moving grain boundaries and hinder grain coarsening, thus strenghten the alloy. In order to acquire required microstructure and properties, alloying composition

Table 1.8: Temperatures of β -to- α transformation

Temperature	Alloy	Mn	Fe	Si	State	Reference
400 °C	3003	1.15	0.58	0.20	DC	Li et. al. [17]
350 °C	3003	1.18	0.58	0.2	rod, 50 K/h	Dehmas et. al. [5]
500 °C					rod, 20 K/min	Dehmas et. al. [20]
450 °C		0.10	0.32	0.13	TRC, CR	Karlík et. al. [8]
465 °C		1.05	0.14	0.10	strip cast	Warmuzek et. al. [13]

and processing parameters have to be carefully adjusted. Coarser precipitates negate the favorable pinning effect of smaller particles, but they can induce formation of finer grains.

Precipitation of new phases is influenced by many factors like time, temperature, composition, manufacturing route and thermal history of the material. Increasing the aging temperature (decreasing the supersaturation) in any precipitation reaction reduces the chemical driving force for nucleation leading to: (i) larger precipitates (because the critical radius for nucleation is larger); and (ii) a reduced equilibrium volume fraction of precipitates [60]. Precipitation is firstly controlled by nucleation and growth and at higher temperatures by coarsening [19].

Different temperature intervals of precipitation reported on a range of materials by variety of authors are summarized in Table 1.9. Usually the precipitation in Al-Mn alloys takes place between 300 °C and 450 °C.

Precipitation kinetics is influenced by temperature [61]. The lower is the annealing temperature, the finer is the dispersion of the particles [62]. As the annealing temperature rises, the number of precipitates firstly increases and then (around 450 °C) it starts to decrease due to dissolution. However, the average diameter of the particles continues to grow [19]. The number density of precipitates at a given temperature increases with the silicon content [7].

During isochronal aging precipitates nucleate at the lowest possible aging temperature, where the solute supersaturation and chemical driving force are greatest, resulting in: (i) smaller precipitates, since the critical radius for nucleation is reduced; (ii) larger volume fraction of precipitate-rich dendrites since the supersaturation is greatest at lower temperatures.

According to Dehmas et. al. [5] the α -phase precipitates in AA3003 alloys are isostructural with the primary particles, as no additional peaks in RTG spectra were observed after precipitation.

At temperatures higher than 450 °C two processes regarding precipitates were reported [17, 21, 22, 34]:

- dissolution,
- coarsening.

Smaller precipitates dissolve back to the solid solution thanks to the higher solubility of manganese at elevated temperatures. Due to the re-enrichment of the solid solution the remaining particles may coarsen and increase their diameter;

area fraction of secondary particles decreases [13,25]. Also primary particles may increase their diameter on the expense of precipitates [5,19].

In binary Al-Mn alloy heat-treated at 250 °C and 450 °C precipitates are distributed homogeneously [8]. Addition of silicon and iron leads to the formation of coarse primary phases and also to coarsening of precipitates. Their distribution is then less homogeneous. Density of coarser particles increases with the amount of alloying elements.

Karlík et. al. [8] also compared the precipitation process during one-step annealing at 450 °C and two-step annealing at 250 °C and 450 °C in twin-roll cast sheets. The two-step annealing yields higher density of particles in the middle of the sheet in Al-Mn, Al-Mn-Si and Al-Mn-Si-Fe alloys. Only in Al-Mn-Fe alloy the precipitates density is higher after one-step annealing. Addition of iron to the Al-Mn-Si alloy results in reduced particle density.

In step annealing the solution quantity is determined by temperature of the last step [62]: at lower temperatures precipitates may re-occur, at higher temperatures they dissolve. When the second temperature is lower than the first one, new particles may heterogeneously nucleate on dispersed particles that precipitated at higher temperatures, but the particle density corresponds to the higher temperature. In the case when the second temperature is higher, number density of particles decreases, but also the amount of atoms in the solid solution decreases: unstable finer precipitates dissolve and then they advance growth and spheroidization of remaining larger particles via Ostwald ripening.

In TRC sheets after cold-rolling and annealing at 550 °C for 3 hours the density of precipitates remained constant in alloy with higher silicon content (0.49 wt.%): the nucleation and dissolution rate were equivalent, and the number of coarser particles increased. On the other hand, in the Fe-rich alloy (0.32 wt.%) the precipitates density was reduced on the expense of further coarsening of coarser particles [8].

The distribution of secondary particles is dependent on the cooling rate after annealing: in the work of Engler [63] it was shown that in an Al-Fe-Si alloy large constituent particles with size over 1 μm are present in the matrix when the material is water quenched from 550 °C. After slow cooling the size and volume fraction of the particles increase; as the spatial density remains the same as after quenching, it can be concluded that no new particles precipitate and only the existing ones coarsen during cooling down from high temperature.

In the vicinity of primary particles atoms of alloying elements are consumed on formation of the primary particles and solid solution supersaturation is lower than in the regions out of the range of the primary particles. Due to the low supersaturation less precipitates nucleate here and "precipitates free zones" – PFZ may form: area without precipitates near the primary particles [13,19].

Petterson et. al. [7] shown that the extent of the PFZ increases with time and annealing temperature, as manganese is drained further to the primary particles.

Regarding influence of deformation induced by cold-rolling on precipitation kinetics, implying deformation to the matrix before the heat treatment, driving force for precipitation increases and nucleation sites like dislocations, subgrain and grain boundaries are preferred.

Birol [64] reported that in TRC Al-Mn-Fe-Si alloy the precipitation starts around 350 °C regardless the extent of the deformation; on the other hand, pre-

precipitation is first promoted by the strain induced by cold-rolling as the precipitation is heterogeneous and requires defects and dislocations. However, at the strains higher than 1.6 recovery takes place before precipitation and, thus, reduces defects density in the matrix, which could serve as nucleation sites for precipitates.

The number and size of particles precipitated during recovery and recrystallization increases with decreasing temperature [65].

1.2.3 Homogenization

Homogenization treatment can be applied during thermo-mechanical processing to reduce chemical and structural heterogeneities. It may also promote precipitation of α -phase and " α -to-6" transformation [20]. During homogenization alloy is heated to temperature around 600 °C, held at this temperature and cooled down back to room temperature. At the elevated temperature manganese migrates from solid solution to particles, primary particles transform to stable phases and grow, precipitates nucleate, grow and dissolve.

After casting the solute atoms are distributed inhomogeneously in the matrix and particles form preferentially on surfaces of dendrites [7,13,28]. Due to homogenization primary particles grow, new coarse particles form and chain structure may be replaced by individual, well-spaced particles [28,59,68].

During homogenization size of precipitates increases with holding time and temperature. However, their number density decreases with time due to their dissolution back to the solid solution [7,19]. Li et. al. [19] reported, that up to 4 hours at 600 °C the size of precipitates increases and then it starts to decrease. After 24 hours no precipitates are observed.

Birol [15] reported that during homogenization at 560 °C new particles of $\text{Al}_6(\text{Mn,Fe})$ phase with ratio $\text{Mn:Fe} > 2$ precipitate and the number of α -particles remains relatively constant, only the manganese content raises as it is incorporated from supersaturated matrix. At 600 °C the $\text{Al}_6(\text{Mn,Fe})$ particles coarsen, the size of α particles does not vary.

During annealing of homogenized materials, no new particles nucleate, atoms from solid solution enrich already existing particles, which formed during homogenization, and cause their coarsening [69].

In homogenized materials recrystallization starts and is completed at lower temperatures and the final grain size is lower [70]. Due to the higher density of dispersoids, non-homogenized materials soften more sluggishly and more discontinuously, even if the deformation induced by rolling is higher [69].

In non-homogenized cold-rolled sheets the recrystallization is influenced by precipitation and the final structure after annealing is coarse-grained. Recrystallization is slower and takes place at higher temperatures. If the homogenization is applied, the precipitation capacity is exhausted and recrystallization can pass more easily, as it is not hindered by small precipitates and final grains are finer [15].

Table 1.9: Temperatures of precipitation processes

Temperature	Phase	Alloy	Mn	Fe	Si	Mg	State	Reference
260-440 °C			1.0	0.32	0.62		TRC, CR	Cieslar et. al. [21]
270-450 °C			0.9	0.6	0.1, 0.5			Cieslar et. al. [22]
200-440 °C		3003	0.9	0.53	0.5		TRC, CR	Poková et. al. [66]
300-530 °C		3003	1.15	0.58	0.20		DC	Li et. al. [17]
250-450 °C			1.4	0, 0.22	0, 0.23		DC, CR	Karlík et. al. [8]
350 °C	α -Al(Mn,Fe)Si	3003	1.18	0.58	0.2		rod	Dehmas et. al. [5]
400-460 °C	Al ₆ (Mn,Fe)	3003	1.09	0.5	0.1		DC	Huang et. al. [62]
350-500 °C	α -Al(Mn,Fe)Si	AA3003					rod	Dehmas et. al. [26]
300-530 °C		AA3003	1.15	0.58	0.20		DC	Li et. al. [19]
300 °C	quasicrystal, icosahedral							
500 °C	Al ₁₂₋₁₃ (Mn,Fe) ₃ Si _{1.2-2} , SC							
500-550 °C		AA3103	1.0	0.57	0.12-0.98	0.015	cast in cradle mould	Petterson et. al. [7]
290-465 °C	α -Al(Mn,Fe)Si		1.05	0.14	0.10		strip cast	Warmuzek et. al. [13]
350 °C	Al ₁₅ (Mn,Fe) ₃ Si ₂		1.19	0.61	0.16		TRC, CR	Birol et. al. [64]
275-400 °C				0.48	0.65		TRC, CR	Benum et. al. [65]
340 °C	cubic Al ₁₂ (Mn,Fe) ₃ S	AA 8006	0.4	1.5	0.16		TRC, CR 96 % TRC, CR 33 %	Slámová et. al. [34]
430 °C								
320-450 °C	Al ₁₅ (Mn,Fe) ₃ Si ₂	3003	0.86	0.61	0.10		TRC, CR	Veselý [39]
300-400 °C		3003	1.0	0.19-0.83	0.6		TRC, CR	Slámová et. al. [67]
320-500 °C	Al ₆ (Mn,Fe)		1.262	0.012	0.008		CR	Vlach et. al. [45]
250-445 °C			1.0	0.6	0.6		TRC, CR	Slámová et. al. [67]

1.3 Recrystallization

1.3.1 Grain boundaries

Grain boundaries separate regions within the material which contain the same phase and crystal structure but different orientation. They constitute the contact area of the internal surfaces of adjacent grains. Generally as high angle grain boundaries (HAGB) are considered those with misorientation $>15^\circ$, low angle grain boundaries (LAGB) have misorientation $< 15^\circ$ [71].

A displacement of a grain boundary is equivalent to the growth of one crystalline at the expense of the shrinking neighbor. Grain boundary velocity v can be expressed as

$$v = M \cdot P, \quad (1.2)$$

where P is driving force for boundary motion and M is a grain boundary mobility, which depends on temperature, lattice constant, Debye frequency and migration free energy [71].

Generally it can assumed that the driving force occurs whenever a grain boundary displacement leads to a decrease in the total free energy of the system. The most important phenomena influencing the driving force are

- excess density of defects,
- energy of high angle boundaries,
- pressure difference on sides of a grain.

An excess density of defects (mainly of dislocations) in one of grains is a powerful source of a driving force. It is highly reproducible, easy to fabricate and provides a wide range of driving forces, up to 10 MPa by orders of magnitude. Due to it the instability of the driving force during recrystallization can be easily explained (recovery, local variations of dislocation density, etc.). As for the energy of high angle boundaries, it is considered as relatively reproducible and stable and reaches values of $4 \cdot 10^{-4}$ MPa. Driving force exerted by the pressure difference Δp on both sides of the grain boundary is given by a surface tension γ and main radii of curvature R_1, R_2

$$P = \Delta p = \gamma \left(\frac{1}{R_1} + \frac{1}{R_2} \right). \quad (1.3)$$

Due to an interaction energy between boundary and impurity atoms, solute atoms tend to segregate on the boundary. When the grain boundary moves, the segregated atoms will attempt to remain at the boundary, which means that the boundary has to drag the impurity alongside and its velocity is lowered to the speed of the impurity. The drag force P_v is proportional to the number of foreign atoms per unit area of the boundary n and attractive force f between the atoms and the grain boundary:

$$P_v = n \cdot f. \quad (1.4)$$

The drag force acts against the driving force and decelerates the grain boundary motion. If the driving force increases, impurities will no longer be able to keep up with the boundary and the boundary will detach from them and move as free [71].

1.3.2 Recrystallization and grain growth

During deformation of a metal by hot or cold working, dislocations are generated and stored in the material. Dislocations are non-equilibrium lattice defects and, thus, material tends to remove them in order to achieve thermodynamic equilibrium. However, dislocation arrangement of a deformed crystal is mechanically stable. Dislocation structure can be unstabilized by introducing a sufficient heat treatment. The two possible ways how to reduce the energy stored in the material by dislocations are:

- recovery,
- recrystallization.

Recovery comprises of all processes which lead to annihilation or rearrangement of dislocations into low-energy dislocation structures. On the other hand, recrystallization leads to generation of new grain boundaries and their movement. Moving grain boundaries eliminate dislocation substructure and, finally, new strain-free structure is formed.

Recovery and recrystallization are competing processes as both are driven by stored deformation energy. Once the recrystallization has taken place, the recovery can not appear. Extent of recovery depends on the ease of recrystallization and is easier in metals with high stacking fault energy. Recovery releases deformation energy and lowers driving force for recrystallization. Thus, recovery increases recrystallization resistance [64]. Both recovery and recrystallization are influenced by the annealing temperature.

After recrystallization, material contains grain boundaries that are (like dislocations) thermodynamically non-equilibrium. Grain growth thus occurs in fine-grain structures where the driving force is given by the decrease of the grain boundary energy. Two types of grain growth are generally observed: continuous and discontinuous. During continuous grain growth grains grow while some of them shrink. The average grain size increases and grain size distribution remains self-similar. When it comes to discontinuous grain growth, only few grains grow at the expense of other non-growing grains. As this phenomena resembles recrystallization in some points of view, it can be called secondary recrystallization.

Driving force P for recrystallization is given by reduction of the Gibbs free energy G of the solid, which is induced by a displacement of a grain boundary:

$$P = -\frac{dG}{dV}. \quad (1.5)$$

Here dV denotes volume swept by the boundary during its movement. The driving force for primary recrystallization is the strain energy of stored dislocations. In the case, when these dislocations are consumed by a moving grain boundary, driving force can be expressed in terms of dislocation density ρ and shear modulus μ

$$P = \frac{1}{2}\rho\mu b^2, \quad (1.6)$$

where $E_v = \frac{1}{2}\mu b^2$ is energy per unite length of dislocation. For $\rho = 10^{16} \text{ m}^{-2}$, $\mu = 5 \cdot 10^4 \text{ MPa}$ and $b = 2 \cdot 10^{-10} \text{ m}$ we get $P \sim 10 \text{ MPa}$.

The driving force for grain growth which is provided by the energy of grain boundaries γ can be expressed for the discontinuous case as

$$P = \frac{3\gamma}{\delta}. \quad (1.7)$$

For subgrain size $\delta = 10^{-4}$ m and $\gamma = 1$ J/m², $P = 0.03$ MPa. This clearly shows that the driving force for recrystallization is much bigger than the one for grain growth. As a consequence grain growth proceeds much more slowly and at higher temperatures than recrystallization.

For the continuous grain growth (which is driven by curvature R of the boundary) we get

$$P = \frac{2\gamma}{R}. \quad (1.8)$$

Since radius of curvature usually exceeds the grain size by an order of magnitude, the driving force for continuous grain growth is about an order of magnitude smaller than for secondary recrystallization.

Nucleation

Potential recrystallization nucleus can be a crystallite which is partially surrounded by mobile high angle boundaries formed during deformation or as an effect of recovery. It can be a subgrain in contact with a deformation heterogeneity or with an old grain boundary. It will be a successful nucleus when it is sufficiently large to overcome condition given by Gibbs-Thompson relationship [65, 72]:

$$\lambda_c = \frac{2\gamma}{P_D - P_Z}, \quad (1.9)$$

where λ_c is a critical nucleus size, P_Z restraining Zener pressure and P_D driving pressure given by stored energy:

$$P_D = \frac{1}{2}\rho\mu b^2 + \alpha\frac{\gamma}{\delta}, \quad (1.10)$$

with α a constant $\sim 2-3$.

Recrystallization

When a deformed material is annealed at sufficiently high temperature, it usually recrystallizes. Grains which are almost defect free are formed and they further grow and consume the deformed microstructure until the material is fully recrystallized. This phenomena is called discontinuous recrystallization. During this process, the microstructure is heterogeneous and can easily be divided into regions which have already recrystallized and others, which are still deformed. The fraction of recrystallized material increases from 0 to 1 during the transformation.

However, under certain conditions continuous recrystallization can take place. Highly deformed metal may transform during annealing to a microstructure of approximately equiaxed defect-free grains, which are predominantly bounded by high angle grain boundaries by relatively localized boundary migration. This process is relatively homogeneous and parts which have already recrystallized

and parts, which are still deformed (unrecrystallized), cannot be distinguished during the transformation [73].

The continuous phenomena includes recovery by subgrain growth, continuous recrystallization and normal grain growth. Discontinuous phenomena incorporates discontinuous subgrain growth, primary recrystallization and abnormal grain growth [74, 75].

The kinetics of discontinuous recrystallization describes change of recrystallized volume fraction X in time t . It is determined by thermal activation of the recrystallization mechanisms, nucleation and nucleus growth and can be described by Avrami-Johnson-Mehl-Kolmogorov equation

$$X = 1 - \exp \left\{ - \left(\frac{t}{t_R} \right)^q \right\}, \quad (1.11)$$

with q as an Avrami exponent and t_R characteristic time for recrystallization (when 63.2 % is recrystallized) [71]. For constant and homogeneous nucleation rate \dot{N} and isotropic growth rate v_G it holds

$$X = 1 - \exp \left(- \frac{\pi}{3} \dot{N} v_G^3 t^4 \right). \quad (1.12)$$

Thus, recrystallized grain size d

$$d = 2v_G t_R \cong 2 \left(\frac{3}{\pi} \frac{v_G}{\dot{N}} \right)^{1/4}. \quad (1.13)$$

Recrystallized grain size is a result of a competition between nucleation and growth rate. On the contrary, recrystallization time is a effect of both nucleation and growth and is governed by grain boundary migration rate.

Grain growth

After primary recrystallization grain boundary surface area can be reduced by arranging grain boundaries in planar positions. Curvature of a boundary results in driving force to straighten the boundary: the boundary tends to move towards the center of the curvature. In two dimensional case, grains with more than six sides have concavely curved boundaries and expand, those with less than six sides have convexly curved boundaries and shrink. Large grains are in contact with many smaller ones and are composed of many concavely shaped segments and expand.

If the grain size becomes comparable with the smallest specimen dimension, grain growth is reduced. Grain coarsening can be also restricted in strongly textured materials.

In the presence of inclusions of the second phase, the grain boundary motion is hindered. Pinning from precipitates Z (Zener drag) can be expressed by formula:

$$Z = \frac{3}{2\pi} \frac{f_p}{r_p^2} 2\bar{R}^2, \quad (1.14)$$

where f_p is volume fraction of precipitates, r_p is their diameter and \bar{R} is an average radius of subgrains. During annealing Z firstly decreases as the precipitates radius increases, afterwards it increases with the augmenting subgrain size.

Grain coarsening ceases when the driving force for increasing the grain size is balanced by the Zener drag. The final grain size D_f is expressed by radius of curvature R and average grain diameter D as

$$D_f = \frac{4r_p R}{3f_p D}. \quad (1.15)$$

1.3.3 Experimental data

Many aluminium alloys recrystallize during high temperature forming operations or during annealing which comes after deformation at low temperature. Recrystallization leads to a deterioration of mechanical properties such as strength, and in some cases the fracture toughness may be considerably reduced. Addition of alloying elements like Mn, Zr and Sr increases the recrystallization resistance by forming dispersoids that exert a drag force on moving subgrain boundaries. Table 1.10 summarizes results of several authors with regard to the recrystallization temperature in Al-Mn-Fe-Si alloys.

Deformation energy stored in the material can be reduced before recrystallization by recovery. Lens et. al. [61] reported that in Al-Si alloy the drop of the stored energy was 20 % in an alloy with 0.1 wt.% of Mn and 26 % in an alloy with 0.3 wt.% of Mn.

As reported by Kang et. al. [76] recrystallization resistance can be enhanced by two step annealing. At lower annealing temperature the recovery takes place and the dislocations are removed, thus, reducing the driving force for recrystallization, when the material is exposed to higher temperature.

When the deformation induced by cold-rolling is higher, the extent of recrystallization is smaller due to heavier in-situ deformation recovery – as-rolled foils are already partially recovered and, thus, the driving force for recrystallization is lowered [70].

Large particles promote recrystallization by providing additional nucleation sites – this process is called particle simulated nucleation (PSN); finely dispersed precipitates strongly retard recrystallization when they are present in as-deformed state or precipitate during recrystallization annealing. In the case of bimodal particle structure, complex interaction between particles of all sizes and deformed structure may occur [63].

High temperature treatment increases number of potential sites for PSN by coarsening constituent particles and by dissolving of the finest particles, which could hinder formation of viable recrystallization nuclei [59].

If fine precipitates are present in the material before deformation, after deformation they will stabilize dislocation network and make nucleation process more difficult [30].

Recrystallization may be significantly influenced when it takes place simultaneously with precipitation [15,29,59,64,77,78]. Newly nucleated particles interact with dislocations and, thus, retard recrystallization. During annealing at lower temperatures the precipitation takes place before or during the onset of recrystallization, recrystallization is retarded and new grains are coarse and elongated. If the annealing temperature is higher (according to Liu et. al. [29] approximately 430 °C) the recrystallization is not affected as the precipitation occurs when new

grains are already formed. Due to the lack of interaction of precipitates with growing grains, the final grains are finer [29].

In twin-belt continuous cast AA3003 alloy Liu et. al. [29] reported an inhomogeneous distribution of particles within the sheet thickness. This fact significantly influenced the recrystallization: after 9 hours at 371 °C the surface of the sheet is recrystallized and in the central part only partial recrystallization occurs. However, after 3 hours at 399 °C the recrystallization starts in the center, where coarse elongated grains are formed. At 427 °C the recrystallization is almost homogeneous, new grains are formed after 15 minutes and they are finer than those which nucleated at lower temperatures. Liu et. al. [29] also estimated the Avrami exponent from JMAK equation (eq. 1.11): 3 for 371 °C and 0.8 for 427 °C. According to other literature resources, this number should not vary with the temperature. Activation energy for recrystallization was estimated as 465 kJ/mol.

In thin TRC strips with inhomogeneous structure, the recrystallization of grains near the surface of the foil is realized by the growth of grains which nucleated in the central part. The grain boundaries in the center are highly mobile unlike those near the surface, which are pinned by very fine dispersoids formed during earlier stages of annealing [30]. The particle simulated nucleation near the surface can be neglected as the particle size there is too small [65].

In twin-roll cast alloys with Mn, Fe and Si [8, 25] after cold-rolling and annealing for 3 hours at 550 °C the grain structure is highly dependent on the iron and silicon content. The iron rich (0.32 wt.%) alloy exhibits very fine grains from 50 to 100 μm long in the central part and from 200 to 300 μm long near the surfaces of the strip. However, in the alloy with 0.49 wt.% of silicon the grains are coarse with length of several hundreds of μm . The difference is caused by particle simulated nucleation in the Fe-rich alloy, which contains higher density of coarse primary particles. Moreover, the density of small particles (from 30 to 200 nm), which may block movement of subgrain and grain boundaries by Zener drag, is higher in the Si-rich alloy.

Overall grain size after recrystallization can be reduced by slow cooling: excess manganese deposits during cooling on constituent particles and the solid solution supersaturation is lowered. Due to it, less precipitates are formed during annealing [59].

Opposite process was described by Benum [65]: during rapid solidification coarser particles (1.5 μm) may emerge and subsequently induce particle simulated nucleation.

Sun et. al. [59] investigated the role of homogenization on the course of recrystallization in twin-roll cast AA3105 alloy after cold-rolling. In the non-homogenized material recrystallization is slower due to the concurrent precipitation of large quantities of dispersoids on subgrain boundaries and, as there is only a limited number of nucleation sites, grains are coarse and elongated in the rolling direction. On the other hand, in the homogenized material grains are finer and equiaxed. The higher is the homogenization temperature, the finer are the grains after recrystallization.

These observations are in accordance with results of Birol [64] who reported that the recrystallized grains are finer in the homogenized materials and are coarser in materials with high density of dispersoids. Birol [79] also reported that in homogenized alloy the recrystallization is discontinuous and without the prior

Table 1.10: Temperatures of recrystallization

Temperature	Mn	Fe	Si	State	Reference
250-450 °C	1.4	0, 0.22	0, 0.23	DC, CR	Karlík et. al. [8]
> 280 °C	1.10	0.32	0.13	TRC, CR	Karlík et. al. [25]
>350 °C	1.06	0.18	0.49	TRC, CR	Karlík et. al. [25]
370-430 °C	1.0	0.6	0.2	TBCC ¹ , CR	Liu et. al. [29]
450 °C	1.19	0.61	0.16	TRC, CR	Birol [64]
400 °C	1.192	0.605	0.163	TRC, CR	Birol [15]
350 °C				TRC, hom., CR	
420 °C	0.471	1.658	0.260	TRC, CR	Birol [30]
350 °C	0.9	0.53	0.5	TRC, CR	Poková et. al. [66]
300 °C				TRC, hom., CR	
350-450 °C	1.0	0.19-0.83	0.6	TRC, CR	Slámová et. al. [67]

recovery.

The shape of recrystallized grains is related to the distribution of secondary phases in the matrix. For example if particles nucleate preferentially on grain boundaries and the material is cold-rolled, the recrystallized grains will be aligned in the rolling direction, as the particles will exert Zener drag on the moving grain boundaries and their motion will be limited in direction which is perpendicular to the sheet surface [29].

In an AA 5052 alloy Nah et. al. [80] showed that increasing amount of shear deformation increases refinement of final grain size after recrystallization and that the grain size is controlled by effective strain and is affected by the type of recrystallization texture. According to Birol [79], the increasing strain firstly accelerates recrystallization. Nevertheless, at higher strains (> 3.5) the recrystallization is shifted to higher temperatures. On the other hand, in another work of Birol it was demonstrated that the recrystallized grains are coarser if the strain induced by cold-rolling is increased [64].

Whether the grain growth during recrystallization is continuous or discontinuous depends on the original grain size [69]. The continuous growth dominates when the deformation induced by cold-rolling is higher.

1.4 Zirconium

Zirconium forms with aluminium peritectic phase diagram between aluminium (Al) and Al_3Zr phase with peritectic temperature 600 °C. The Al_3Zr can exist in stable or metastable variant, depending on the thermal history of the alloy. During slow cooling stable form of Al_3Zr nucleates by peritectic reaction, with higher cooling rate non-equilibrium peritectic reaction is preferred and metastable particles form. Supersaturated solid solution of Zr in Al can be received at very high cooling rates [81].

Metastable Al_3Zr particles have cubic structure L1_2 with space group $\text{Pm}\bar{3}\text{m}$ (Figure 1.3a). The lattice constant was measured by convergent electron beam diffraction by Vecchio et. al. [82] as $a = 0.408$ nm, which is near to pure alumi-

um ($a = 0.405$ nm). However, average composition of metastable Al_3Zr particles was found to be ~ 60 % Al and ~ 40 % Zr, which is different from stoichiometric composition 48 % Al and 52 % Zr. This fact indicates that metastable phase field may exist in Al-Zr system [82]. Metastable particles are coherent with the matrix and, thus, they are efficient in pinning grain boundaries, because grain boundaries must change particle-matrix interface from coherent to incoherent, if they want to pass through.

In alloys with higher Zr content or annealed at higher temperatures, stable Al_3Zr phase can be found. It has tetragonal body-centered structure D0_{23} (Figure 1.3b) with space group I4/mmm and lattice parameters $a = 0.4014$ nm and $c = 1.7321$ nm [82,83]. It has been shown [84] that in binary Al-0.5Zr alloy non-equilibrium phase transforms to the equilibrium one after 120 hours of annealing at 500 °C, preferentially on grain boundaries. The high stability of metastable phase can be attributed to the low solubility of precipitates and low driving force for coarsening, which are connected with the fact that the structure and lattice parameter of particles and the matrix are similar and precipitates have low surface energy.

Knipling et. al. [83] reported that transformation from metastable cubic L1_2 structure to stable tetragonal D0_{23} in Al-0.1Zr starts during annealing at 475 °C. Smaller L1_2 particles dissolve and re-precipitate at dislocations, subgrain and grain boundaries as stable D0_{23} , other precipitates coarsen and transform to D0_{23} structure; the D0_{23} precipitates are disc shaped with radius 200 nm and thickness 50 nm and are partially coherent with aluminium matrix – principal axes of tetragonal unit cell are parallel to those of the Al matrix. Karlík et. al. [8] reported in twin-roll cast AA3003 alloy large blocks of primary Al_3Zr phase with diameter more than 30 μm and needles with length around 100 μm .

Thanks to the addition of zirconium, microstructure of aluminium alloys can be stabilized and their recrystallization resistance enhanced [70, 85, 86]. Alloys with addition of zirconium have also generally finer grain structure in the as-cast state [70]. The conditions of precipitation of metastable cubic Al_3Zr and its influence on recrystallization in different aluminium alloys has been deeply studied in recent years [8, 83, 87–90].

Zirconium atoms are distributed inhomogeneously within the aluminium matrix due to the microsegregation [84]. As the Al-Zr binary diagram is peritectic, Zr segregates at dendrite centers during solidification [87]. As a consequence, precipitates of Al_3Zr phase are inhomogeneously arranged and places with low density of these particles are more prone to recrystallization. Jia et. al. [88] tried to eliminate this heterogeneity by homogenization. The applied homogenization helps to minimize the concentration gradients of Zr, however, it also reduces the driving force for nucleation of Al_3Zr due to elimination of local high concentration levels of Zr and no such particles are formed. The reduction of solid solution levels of Mn and Si, whose presence is required for Al_3Zr formation, also hinders their formation. In the same alloy without homogenization treatment, the Al_3Zr particles nucleate heterogeneously and their diameter increases with annealing time from ~ 10 nm to 25 nm. Recrystallization starts around 450 °C whereas in the homogenized sample recrystallization resistance is much lower, first nuclei form at 350 °C.

To enhance homogeneous precipitation of Al_3Zr particles and, thus, recrystal-

lization resistance, Jia et. al. [89] proposed a two-step precipitation annealing for DC cast Al-Mn-Zr alloy. Firstly, the material is annealed at lower temperature and then it is held at higher temperature. The higher temperature was chosen 450 °C, when the precipitates are known to form even during one-step annealing. The highest number density of precipitates is formed when the first annealing is held at 350 °C (4 times higher than just annealing at 450 °C). However, the highest recrystallization resistance and coarser recrystallized grains were reported after annealing at combination 250 °C + 450 °C. Driving force for precipitation increases with decreasing temperature; however, at lower temperature the diffusion rate is smaller and precipitation of fully developed Al₃Zr is suppressed. Thus, the fact that the recrystallization resistance was not the highest after the treatment which gave the highest number of precipitates can be explained by the formation of smaller zirconium clusters, which are under detection limit, however, still inhibiting grain boundary motion. Another positive effect of two-step annealing according to [89] was the improvement of the material strength.

However, Karlík et. al. [90] reported that microhardness and conductivity values do not differ for DC cast alloys for one step 450 °C and two step 250 °C + 450 °C annealing, even the recrystallization resistance is the same for both annealing treatments. Nevertheless, the increased conductivity and the decrease of microhardness during heating from 250 °C to 450 °C suggest that the solid solution is depleted and majority of precipitates is formed in this temperature range.

Jiang et. al. [91] in their work on AA5083 alloy (Al-4.58Mg-0.56Mn-0.08Cr) with addition of 0.16 wt.% of Zr used two-step homogenization process 400 °C/4 h + 475 °C/24 h to form homogeneous distribution of fine Al₃Zr precipitates with size of 50-100 nm.

The size of metastable cubic Al₃Zr varies from less than 10 to 30 nm in average in dependence of the thermal treatment, alloy composition and microsegregation. Knipling et. al. [87] showed that in conventionally solidified Al-0.1Zr alloy smaller precipitates (≤ 10 nm) are homogeneously arranged in the center of the dendrites whereas interdendritic Al₃Zr are heterogeneously distributed with lower number density and average diameter 25 nm.

In DC cast Al-Mn-Fe-Si alloys with addition of Zr annealed for 2 hours at 450 °C [86] the microstructure was stable even at 500 °C, in comparison with the same alloy without Zr, which recrystallized at 420 °C.

In Zr-containing alloys iron and silicon support the formation of Al₃Zr precipitates as they usually nucleate on Fe and Si clusters. Moreover, stability of Al₃Zr is enhanced due to the presence of silicon. Silicon addition to Al-Zr alloy increases hardness, precipitation rate and suppress discontinuous precipitation [92].

Weiland et. al. [93] discovered, that in Al-Zn alloy with Zr addition Al₃Zr particles pin dislocations and subgrain boundaries and, thus, impede nucleation of recrystallization; however, in Al-Cu-Mn despite the enhanced recrystallization resistance, no Al₃Zr were detected: they probably impede the recrystallization by solute drag mechanism.

It has been shown that heating rate is crucial for Al₃Zr precipitates formation [88]. Nes et. al. [86] have reported 5 K/min as a critical heating rate in strip-cast Al-Mn-Fe-Si-Zr alloys, above which the metastable zirconium particles do not form during annealing.

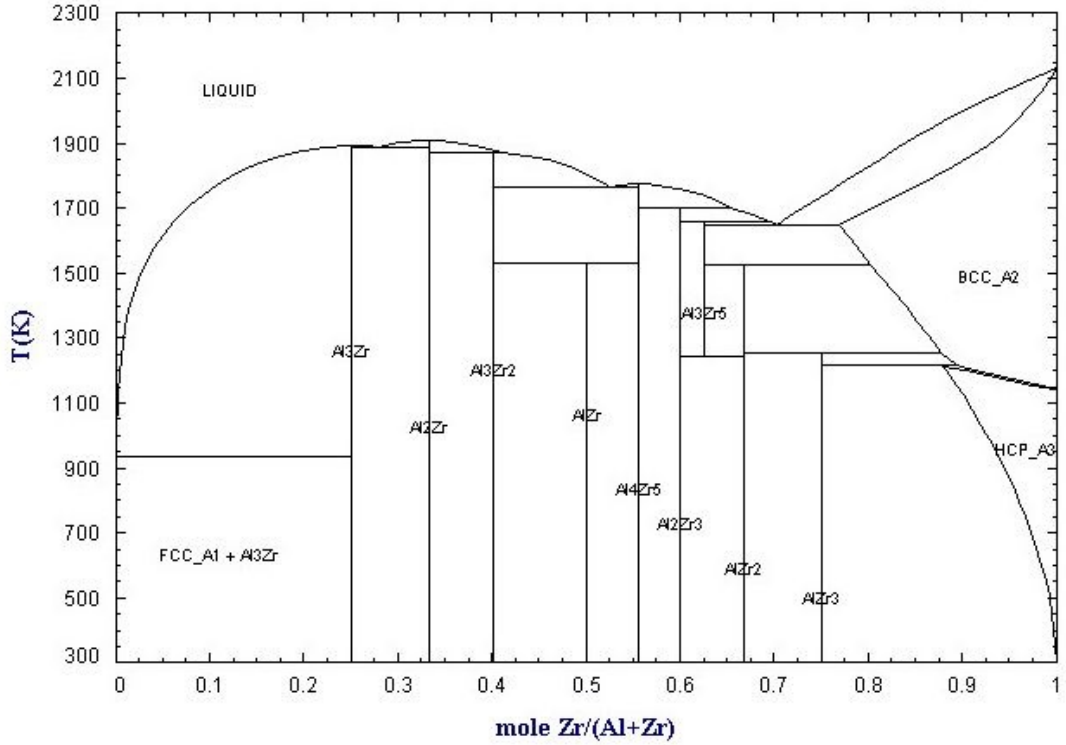


Figure 1.2: Aluminium-zirconium binary phase diagram, from [94].

According to Nes et. al. [86] cold deformation may induce enhanced precipitation at lower temperatures, heterogeneously on dislocations, as they can speed up diffusion of Zr atoms.

1.5 Chromium

In binary Al-Cr alloys the main three precipitating phases are Θ Al_7Cr , η $\text{Al}_{11}\text{Cr}_2$ and Al_4Cr . Equilibrium solubility of chromium in aluminium is 0.38 %; however, due to the rapid cooling up to 6 % of Cr can retain in solid solution [95]. Several stages of decomposition of supersaturated solid solution have been described: formation of coherent clusters, continuous precipitation of Cr-rich particles, discontinuous precipitation and disintegration of large Al grains into small crystallites with Cr atoms segregated to the grain boundaries [95].

Θ phase Al_7Cr (also $\text{Al}_{13}\text{Cr}_2$, $\text{Al}_{47}\text{Cr}_7$) has monoclinic structure with C2/m space group and lattice parameters $a = 2.5256$ nm, $b = 0.7582$ nm, $c = 1.0955$ nm, $\beta = 128.68^\circ$ [96,97]. η $\text{Al}_{11}\text{Cr}_2$ (also Al_5Cr) is monoclinic P2 with $a = 1.2880$ nm, $b = 0.7652$ nm, $c = 1.0639$ nm, $\beta = 122.33^\circ$ and Al_4Cr has monoclinic structure P2/m with $a = 0.8716$ nm, $b = 2.3946$ nm, $c = 1.9386$ nm, $\beta = 199.33^\circ$ [98].

Besides zirconium, chromium is known to inhibit grain coarsening and delay recrystallization in aluminium alloys [99]. In 7000 alloys Li et. al. [100] reported, that alloy with addition of Cr exhibits finer intermetallic particles, smaller average grain size and lower recrystallization resistance than alloy with Zr. According to [101], Cr has quantitatively the same influence on alloy microhardness as manganese.

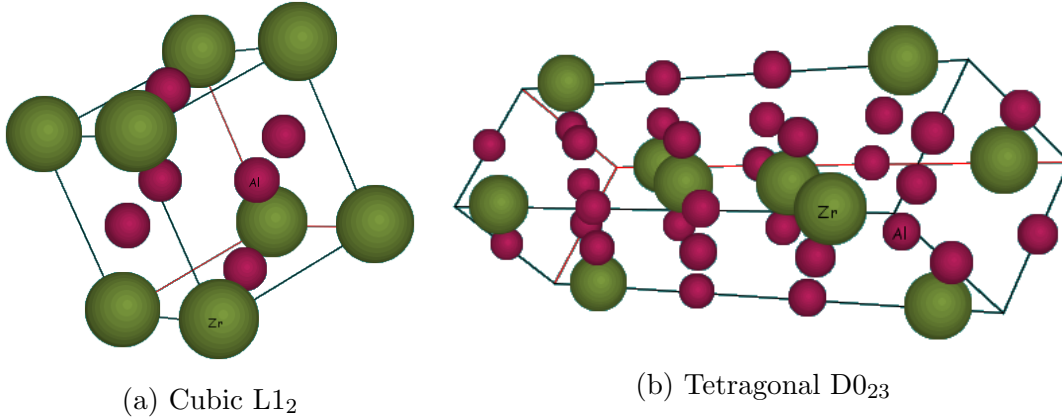


Figure 1.3: Two possible structures of Al_3Zr phase – metastable cubic $L1_2$ and stable tetragonal $D0_{23}$. Al = violet atoms, Zr = green atoms [3].

In ternary Al-Mn-Cr alloys chromium atoms can substitute manganese in Al-Mn intermetallic phases without change of the crystal structure [102]. Precipitation of Cr-containing particles takes place at similar temperatures as of Mn-rich phases, but is more sluggish [103]. In more complex alloys Cr occupies Mn and Fe lattice sites and can form α -phase like $Al_{15}(Mn,Fe,Cr)_3Si_2$ [16, 24, 103–105]. In alloys from 6000 series chromium increases volume fraction of Fe-bearing particles and may be beneficial for formability as it promotes α - $Al_{15}(Fe,Cr)_3Si_2$ formation at the expense of β - $Al_9Fe_2Si_2$ phase [104]. Timelli et. al. [105] reported, that in $AlSi_9Cu_3Fe$ alloy addition of chromium leads to higher volume fraction of intermetallic compounds, more spread size distribution of these compounds and higher microhardness.

1.6 Twin-roll casting

Twin-roll casting (TRC) is one of the methods how to cast a metal. Metal or alloy is melted in a holding furnace and the melt flows through a launder and a cast box to a nozzle, which directs the melt between two water-cooled rolls (see Figure 1.4). These rolls are designed to fill both heat exchanger and rolling function. The metal exiting the nozzle solidifies on the rolls into a strip which is further work-hardened by the rolls. Strip with thickness around 10 mm and width approximately 1 m is thus produced (Figure 1.5). It can be reeled on a coil, which can accommodate up to several tons of material (Figure 1.4).

In comparison with direct-chill casting (DC), twin-roll casting is less demanding on the amount of energy and material used during manufacturing. Thus, production of strips is more economic. However, the initial microstructure of the TRC strips shows some differences and has been carefully studied in recent years [21, 25, 29, 65, 66, 106, 107]; twin-roll cast materials exhibit higher solid solution supersaturation [34] and inhomogeneous structure within the strip thickness: grain size and second phase particles distribution are different in the center of the sheet and near the surface. High solidification rate around 500 °C/s results in microstructure refinement [34], formation of finely distributed primary particles and high solid solution supersaturation. The sheets can suffer from macrosegre-

gation in a form of central eutectic segregates or microsegregation which scales with the dendrites arm spacing [108].

Rapid solidification causes not only the formation of supersaturated solid solution, but metastable and non-equilibrium solidification structures and precipitates of metastable alumides can appear in the material.

The initial microstructure of a sheet is influenced by many parameters, for example:

- casting speed,
- temperature of the melt,
- temperature of cooled rolls,
- lubrication of rolls,
- specific load on rolls,
- chilling speed,
- thickness of the sheet (distance between rolls),
- thickness of the nozzle.

Relationship between dendrite arm spacing d and chilling speed c can be described with the use of two constants A and n , which are specific for each material [109]:

$$d = A \cdot c^n. \quad (1.16)$$

According to Yun et. al. [110] decrease of the specific load at a fixed sheet thickness is equivalent to increase of casting speed; defect free structure can be obtained by combination of high specific load and high sheet thickness. Gras [107] reported that increased load during casting leads to finer structure.

After heat treatment, the size of second phase particles in TRC alloys is lower and number density higher than in DC (maximum diameter of 1 μm vs. 5 μm , respectively); thus, in TRC materials higher dispersion hardening can be achieved, softening kinetics is slower and recrystallized grains are coarser.

Near the surface, where the solidification is more rapid and temperature gradient sharper, primary particles are spherical, finely dispersed, aligned in the rolling direction and solute levels are higher [15]. In the center of the sheet intermetallic particles are coarser and ordered in eutectical colonies. Near the surface the α -particles are rich in iron [15].

If macrosegregation occurs in the center of a sheet. it cannot be reduced by homogenization; it can only be eliminated by controlling of the solidification process. It consists of long solute-rich channels running parallel to the rolling direction and exhibits eutectic features [107]. During solidification the sheet freezes from the surfaces and remaining liquid in the central part shifts its composition to the eutectic range, where it finally solidifies. Materials with long freezing range and higher content of alloying elements are more prone to macrosegregation. Moreover, high cooling rates expand solidification interval and promotes macrosegregation [108].

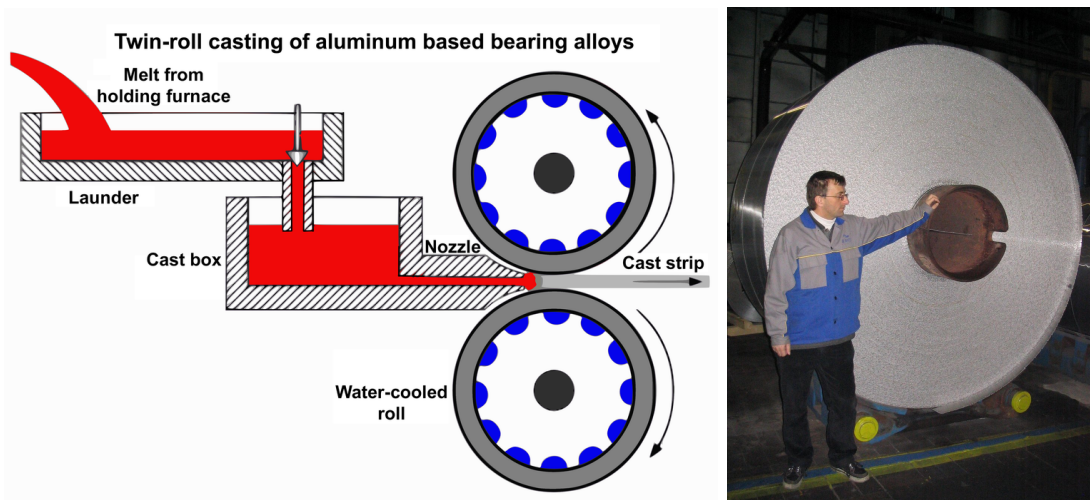


Figure 1.4: Scheme of twin-roll casting and a coil with tons of twin-roll cast aluminium alloy.

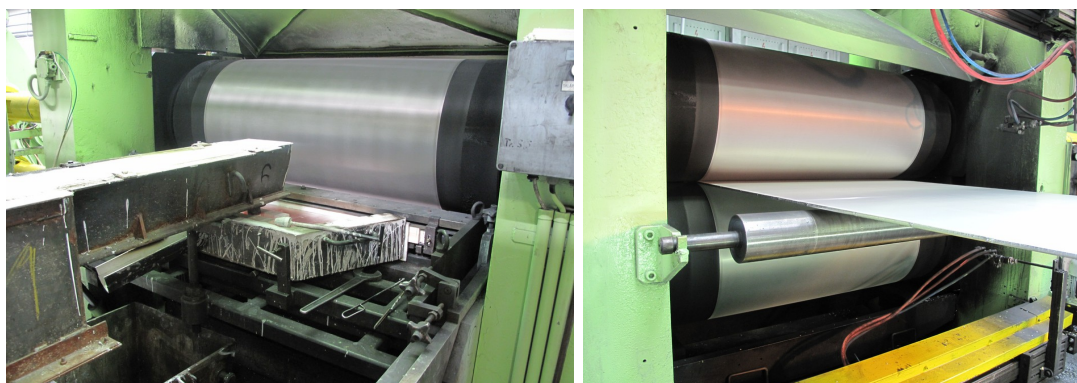


Figure 1.5: Twin-roll casting in factory conditions: pouring of the melt between the rolls and a freshly solidified sheet.

The central eutectic segregates are not affected by cold-rolling, aluminium matrix deforms around them.

Grains after TRC can be inclined from the rolls to the center of the strip [8]. Orientation of the long and fine grains near the sheet surface is a result of coupling between directional solidification and subsequent hot rolling component of twin-roll casting [107]. In the central part of the foil grains are coarser and elongated in the rolling direction [15, 30]. Benum et. al. [65] measured the subgrain size in TRC AlFeSi alloy as $1.8 \mu\text{m}$ with misorientation 18.9° near the surface and $2.5 \mu\text{m}$ with 8.8° in the center.

After recrystallization, the average grain size of twin-roll cast materials is higher than the grain size of direct-chill cast ones [59] and grains are more elongated [106]. The softening kinetics in TRC materials is slower than in conventional ingot-cast ones.

1.7 Equal channel angular pressing

The production of materials with finer grain size is of great importance, as reduction of the grain size results generally in a strength increase at lower temperatures and in a formability enhancement at elevated temperatures. One of the techniques how to refine aluminium alloys are methods of severe plastic deformation (SPD), which can produce grains smaller than 1 μm by imposing a very high plastic strain into the material [111]. The most common SPD techniques are equal channel angular pressing (ECAP), high pressure torsion (HPT) or accumulative roll bonding (ARB).

The application of ultrafine-grained materials is connected with the increased strength of the material. This can be described by a Hall-Petch relation, which states that the strength of a material increases with decreasing average grain size. It can be given in the form of equation

$$\sigma_y = \sigma_0 + K_y d^{-1/2}, \quad (1.17)$$

where σ_y is yield stress, d is average grain diameter and σ_0 and K_0 are coefficients unique for each material (eg. [60]). They may depend on many parameters like temperature of deformation, deformation rate and structural parameters of the material in question. Similar equation may be reformulated for hardness HV with parameters H_0 and K_H [58] as

$$HV = H_0 + K_H d^{-1/2}. \quad (1.18)$$

The slope K_H may be increased by dislocation density, solute atoms and fine particles in the matrix [58].

1.7.1 ECAP process

Equal channel angular pressing is a method of severe plastic deformation, when a billet is pressed by a plunger through a special die consisting of two channels of the same cross section which intersect at an angle Φ ($90^\circ \leq \Phi < 180^\circ$). The scheme of ECAP is given in Figure 2.2 on page 46. During the process material undergoes straining by simple shear [112]. The strain induced in a single pass through the die depends primarily upon the angle Φ and for $\Phi = 90^\circ$ the shear is approximately 1 [113]. The shape of the billet remains nearly unchanged after the pressing. The ECAP procedure can be thus repeated several times and the stored deformation energy can be multiplied, so the required level of strain is acquired. Consequently, ultrafine-grained material with a high fraction of high angle grain boundaries is produced.

During the multiple pressing, four basic pressing routes are possible. During route A material is inserted into the channel with the same orientation for each pass. When route C is applied, material is rotated by 180° along its longitudinal axis after each pass. Concerning route B where the material is rotated by 90° , two variants are possible. In B_C rotation is always $+90^\circ$, in B_A the rotation angle alternates between $+90^\circ$ after an odd pass and -90° after an even pass (eg. [113]). The rotation changes the operative shear plane and shear direction [112].

Shearing patterns which develop during repetitive passages through the ECAP die are connected with the nature of grain refinement at high strains and are

influenced by the processing route. Schemes of the shearing patterns are given in [114]. Route A has two shearing planes intersecting at 90° and route C repeats shearing on the same plane. By contrast, in route B_C two shearing directions lie on planes which intersect at 120° – this duality causes subgrain bands to develop on repetitive pressings along two separate and intersecting sets of planes. This leads to rapid evolution in the boundary structure into a equiaxed array of high angle boundaries. Thus, route B_C is considered to be the preferable route for ECAP processing [114].

A number of processing parameters can affect the grain refinement during ECAP, mainly the number of passes, processing route, the channel intersection angle Φ , pressing speed, processing temperature and internal heating during ECAP [115].

The importance of ECAP technique is the possibility to apply it to large bulk materials. Moreover, no residual porosity forms in the materials. Thus, it provides potential for structural and functional applications [115, 116].

Turba et. al. [117] focused on the microhardness distribution along an ECAPed billet. At more than 10 mm from the edges of the billet microhardness values were lower than in the bulk – so called deformation dead zone. This area may exhibit different mechanical properties and microstructure than the bulk part of the billet.

1.7.2 Pure aluminium

Iwahashi et al. [111] studied ECAP of commercially pure aluminium at room temperature by routes A and C. After a single passage through the die, the grain size is substantially reduced and the microstructure consists of parallel bands of subgrains and the grains have low angle of misorientation. These bands are formed essentially parallel to the top and bottom edges of the pressed sample. With increasing strain the subgrains gradually break up. The elongated nature of grains persists up to six passes. During pressing by route C, the grain elongation is apparent up to three passes, after four passes on the microstructure is more homogeneous. The evolution of the grain size during pressing is similar for both routes.

The subgrain boundaries evolve into high angle grain boundaries due to accumulation of the dislocations introduced by the pressing process, giving ultimately equiaxed microstructure with an average grain size in the order of $1 \mu\text{m}$. The evolution is less rapid when pressing route A is used.

In further work [114] also the pressing by the route B_C was studied. The subgrain band structure is evident after two pressings; however, after three and four pressings the grain structure appears reasonably equiaxed. The boundary misorientation is higher than in any microstructure produced by route A. High angle grain boundaries are established more rapidly than by routes A and C. Two passes by route B_C lead to development of two distinct and intersecting subgrain bands, each lying at approximately 45° to the top and bottom surfaces of the sample. The boundary structure evolves more rapidly into equiaxed array of HAGB during the route B_C .

1.7.3 Aluminium alloys

At ultra-high strains a steady-state grain size may be reached that limits the achievable level of grain refinement. This limit is controlled by the mobility of low and high angle grain boundaries. With increasing strain dynamic recovery takes place, which disables the grain size reduction [37]. To decrease the limiting grain size and allow increase in strength, secondary particles, which effectively pin grain boundaries, can be introduced into the material. Presence of alloying elements in solid solution can reduce the recovery rate and promote additional grain refinement [118].

Horita et. al. [116] studied several aluminium alloys after ECAP by route B_C at room temperature. Firstly, the influence of the sample size was evaluated and no difference was shown regarding compression tests and grain sizes observed in TEM. The microstructures of all studied alloys after ECAP consists of grains with size below 1 μm which are separated by HAGB. Also many dislocations are observed within the grains, which indicates that the microstructures are in a high energy and non-equilibrium state. The grain size is the highest for the alloy with the lowest amount of alloying elements - AA1100.

The 0.2 % proof stress increases with an increase of imposed strain; however, the increase is significant only after the first pressing. With further increase of strain the proof stress rises only moderately. The elongation to failure exhibits behaviour with opposite trend than the proof stress – large drop after first ECAP pass and then a plateau. The proof stress increased with the content of magnesium in the alloy.

Processing at elevated temperature leads to increase of the average grain size, whereas the fraction of high angle grain boundaries shows the opposite trend due to faster recovery and associated decrease in the number of dislocations absorbed into subgrain walls [115, 119].

According to Khakbaz et. al. [36] in dispersoid containing alloy average misorientation of formed cells increases more rapidly with increasing strain during severe plastic deformation, so that the rate of strength improvement increases and high strength can be obtained by fewer SPD passes. On the other hand, dispersoids can expedite dynamic recovery and, thus, cease the rate of mechanical properties enhancement.

Microstructure evolution during ECAP is also determined by chemistry of the alloy and by presence of second phase particles in the matrix before ECAP. Sabirov in his work [115] summarized that grain refinement process can be accompanied by dynamic aging – precipitation of secondary particles, their dissolution, breaking into smaller fragments, improvement in the particle distribution in the matrix or complete elimination of the as-cast dendritic microstructure. The presence of fine non-shearable dispersoids homogenizes slip, retards formation of cellular substructure and inhibits development of microshear bands during ECAP in Al-Sc alloy.

Nikulin et. al [41] found out, that in 1561 alloy after one ECAP pass at 300 °C extended low angle grain boundaries form within interior of the original grains. The deformation bands contain high dislocation density and are subdivided by dislocation walls in transverse direction, which leads to formation of highly elongated subgrains with average misorientation of deformation-induced boundaries $\sim 3^\circ$. Chains of recrystallized grains evolve along separate initial boundaries. Af-

ter four ECAP passes the average dislocation density in deformation bands is $\sim 1.5 \times 10^{14} \text{ m}^{-2}$; in the newly recrystallized grains, which are highly misoriented to each other, the dislocation density is $\sim 5 \times 10^{13} \text{ m}^{-2}$. The formation of uniform UFG microstructure is almost complete after 12 passes in the alloy with Al_6Mn particles of size $\sim 25 \text{ nm}$. In the alloy with larger second phase particles ($\sim 150 \text{ nm}$) the dislocation overall density is lower and deformation bands are larger. After 4 passes three types of grains are present – coarse recrystallized grains free of lattice dislocations, lamellar grains subdivided by low angle grain boundaries and, finally, fine recrystallized grains with moderate number of lattice dislocations. Concerning the size of second phase particles, the fine Al_6Mn particles promote extensive grain refinement by pinning the grains (Zener drag) while the corser particles induce an inhomogeneous structure. In the second case the pinning force from the particles is low and abnormal grain growth leads to bimodal structure.

Naizabekov [120] observed in AlSiMnFe alloy that after ECAP (with partial back pressure) the shape and size of larger particles ($\sim 1 \mu\text{m}$) do not vary; however, the total density of particles in the aluminium matrix increases due to dynamic aging caused by plastic deformation. Particles are situated both on the grain boundaries and in the grain interior. The grain size after ECAP decreases with the number of particles in the alloy.

Ning et. al. [121] studied alloys AA5083 with and without addition of zirconium, treated by two-step homogenization $400 \text{ }^\circ\text{C}/4 \text{ h}$ and $475 \text{ }^\circ\text{C}/24 \text{ h}$. After six ECAP passes at $350 \text{ }^\circ\text{C}$ by route C the ultimate strength is higher in the alloy with Zr, the total elongating is comparable for both alloys; moreover, it is substantially higher for ECAPed materials than for the hot-extruded ones. The present Al_3Zr precipitates efficiently pin motion of dislocations. These precipitates can inhibit recovery during hot deformation and also have precipitation hardening effect leading to enhanced strenghtening. Six ECAP passes allow formation of homogeneous distribution of equiaxed fine grains with average grain size $1 \mu\text{m}$ with predominant presence of high angle grain boundaries. The average grain size in the alloy without Zr reaches $2 \mu\text{m}$, as the rate of recovery is not reduced by Al_3Zr precipitates. The finer grains in the Zr-alloy result in a higher strenght which is in accordance with Hall-Petch equation 1.17. The enhanced tensile elongation in comparison with extruded materials can be attributed to the homogeneous distribution of fine grains with high angle grain boundaries. Then the strain distributes homogeneously during tensile deformation and the stress localization is delayed.

Another effect of Al_3Zr was revealed by Ning et. al. [122] in the microstructures of alloys ECAPed at $350 \text{ }^\circ\text{C}$ by route B_C concerning the treatment right after ECAP. In the alloy without Zr the microstructure after air cooling consists of smaller subgrains in comparison with the microstructure after water quenching. The density of dislocations descreases via static recovery during air cooling, some small grains undergo static recrystallization. On the other hand, the microstructures in the Zr-containing alloy are similar after both water quenching and air cooling. The microstructure during air cooling remains stable due to pinning effect of Al_3Zr particles, which inhibit static recovery and recrystallization. The strength is slightly higher for the Zr-containing alloy due to precipitation strenghtening.

1.7.4 Annealing

After ECAP processing the grains are in non-equilibrium state and the grain boundary energy is increased. Due to very high fraction of HAGB already present in the deformed state, annealing leads to recovery and uniform grain growth or continuous recrystallization rather than discontinuous recrystallization. Non-equilibrium grain boundaries display grain growth at low temperatures as low activation energy is necessary for their migration.

For some applications it is required that the ultrafine-grained structure remains stable at high temperatures. Kang et. al. in their work [76] summarized that, generally, recovery and recrystallization are driven by reduction of dislocation density and grain boundary area. Continuous recrystallization consists of recovery and normal grain growth, the increase of average grain size is slow. During discontinuous recrystallization the grain growth is discontinuous and rapid. The type of recrystallization depends mainly on size, orientation and mobility of grains. In the case of ideal ultrafine-grained materials, the grains are strain-free and surrounded by HAGB. Continuous recrystallization is frequently observed. However, continuous recrystallization may be inhibited e.g. by second phase particles or strong texture and discontinuous process takes place.

The temperature, at which the grain coarsening starts, depends on the amount of deformation energy stored during ECAP, which is higher when the ECAP processing is conducted at lower temperatures.

Recrystallization after continuous confined strip shearing – combination of rolling and ECAP was studied by Kang et. al. [76]. After twelve passes the driving force for grain growth is much higher than after two passes, as the mobility of HAGB is notably higher than of LAGB. Nonetheless, the material after twelve passes reveals higher resistance against discontinuous coarsening and, thus, better thermal stability during annealing at 300 °C and 350 °C. In this material, during early stages of annealing, the remaining LAGB are removed and the grain size does not vary very much. Thus, microstructure stable against coarsening is formed. In the material after two passes the fraction of LAGB is much higher and grain size distribution is broader, the cells or subgrains comprise high dislocation density, so the regular discontinuous process of nucleation and growth prevails. To study more deeply the thermal stability after twelve passes, materials were subjected to two-stage annealing. After 24 hours at 300 °C the dislocation debris are removed and at further annealing at 400 °C the grain growth is very slow and only slight coarsening proceeds continuously. This observation confirms the fact, that well-defined uniform cell structure is a prerequisite for stability against coarsening.

Jiang et. al. [91] studied the microstructure evolution of ECAPed Al-Mg-Mn alloy during annealing. After 6 ECAP passes at 350 °C by route B_C the average subgrain size is 2.5 and 1.5 μm and grain size 9.4 and 4.4 μm in longitudinal and transversal direction, respectively. The ratio of HAGB is 48 %. After annealing for 1 hour at 400 °C the grain size remains the same, the HAGB ratio increases. Annealing at 450 °C leads to increase of subgrain size to 43 and 22 μm and grain size 49 and 30 μm in LD and TD, respectively. The ratio of HAGB is 63 % and the average misorientation 32°. At 425 °C the grain structure is bimodal due to abnormal grain growth or secondary recrystallization. As during annealing dislocation density is reduced and internal stresses are relaxed, the strength of

the material decreases and the elongation increases.

The influence of Al₃Zr particles on the microstructure of ECAPed aluminium alloy during annealing was described by Ning et. al. [122]. After annealing at 410 °C for 1 hour only slight grain growth was observed in the Zr alloy – from 1.6 to 3.7 μm. In the Zr-free alloy abnormal grain growth takes place; due to inhomogeneous distribution of dispersed particles the grain distribution is bimodal. After annealing at 460 °C the average grain size reaches the value comparable with the one before ECAP: ~180 μm. This is accompanied by dramatic decrease in tensile strength.

Málek et. al. [68] studied the role of homogenization 610 °C/18 hours on the microstructure of Al-Mn-Sc-Zr alloy after ECAP. The strength of the non-homogenized alloy is higher due to lower size of the strengthening particles. The microhardness of this material is also slightly higher. After annealing at 400 °C/30 min the HAGB are more developed in comparison with the as-ECAPed state. However, the low angle grain boundaries are still present. The present Al₃(Sc_xZr_{1-x}) particles are attributed for the grain stability.

In AA7075 alloy with Zr and Sc addition studied by Turba et. al. [117] after annealing at 350 °C for one hour, the microstructure is homogeneous with sub-micrometer grain size. However, bands of coarsened grains emerge in a small part of the volume. After annealing to 450 °C pronounced coarsening to ~10 μm appears, although regions with sub-micrometer grains are still present in the matrix. When compared with a similar alloy without Zr and Sc addition [123] which is stable only up to 300 °C, the stability is attributed again to the addition of Zr and Sc.

1.7.5 Superplasticity

Superplasticity is an ability to exhibit very high uniform elongation (hundreds of %) without failure. Superplasticity can be characterized by strain rate sensitivity parameter m , which is defined as

$$m = \frac{\delta \log \sigma}{\delta \log \dot{\epsilon}}, \quad (1.19)$$

where σ represents the true stress and $\dot{\epsilon}$ the true strain rate. For superplastic behaviour $m \geq 0.3$.

Numerous aluminium alloys exhibit superplastic behaviour at elevated temperature ($\geq 0.4 T_m$ – melting temperature) and relatively low strain rates (10^{-4} - 10^{-3} s⁻¹), if their average grain size is lower than 10 μm. With further reduction of the grain size, region of superplasticity can be displaced to lower temperatures or higher strain rates [118, 119]. Therefore, fabrication of alloys with grain size below 1 μm is of a great interest. Main advantage of superplastic forming is the possibility to produce components with a complex shape and uniform thickness in one operation.

Grain boundary sliding of HAGB is the main deformation process during superplastic forming. Thus, to achieve superplastic behaviour, the grain growth has to be suppressed as high fraction of high angle grain boundaries have to be retained at temperatures of superplastic forming.

Málek et. al. [119] showed that after superplastic straining in Al-Mg-Sc-Zr alloy after 8 ECAP passes, the grains remain nearly equiaxed, as the grain boundary sliding is accompanied by grain rotations with no orientation relationship to the sample and with a small contribution of dislocation slip in the grain interior. The maximum displacements are close to the grain size – 1-2 μm . In AA7075-Sc-Zr alloy the superplastic characteristics are lost at higher temperatures because of grain coarsening. Moreover, the coarse particles at grain boundaries can retard boundary sliding and serve as preferential spots for cavity nucleation. Such particles inhibit superplastic behaviour in AA7075-Sc-Zr and Al-Mn-Sc-Zr alloys.

In AA7075-Sc-Zr alloy studied in [117] the strain rate sensitivity parameter decreases and its maximum shifts to lower strain rates by two orders in magnitude, when the temperature of testing is increased from 350 °C to 450 °C. This is attributed to the grain coarsening.

Dám et. al. [118] studied Al-Mg-Sc alloy where they observed during in-situ TEM straining dislocation annihilation without significant grain coarsening due to the Al_3Sc precipitates. The LAGB migrate during loading and, thus, change the shape and misorientation of the subgrains; HAGB remain fixed at positions.

Before superplastic deformation, it is usually necessary to temper the specimen at relatively high temperature before the straining starts [118]. The annealing leads to dynamic structural changes as dislocation annihilation, subgrain boundary motion, moderate grain growth or eventually recrystallization. Subgrain boundaries are observed to migrate to form stable structure of equiaxed grains. Such changes may affect the quantification of superplastic deformation.

2. Materials

2.1 Studied materials

Three materials based on aluminium alloy AA3003 were studied. Material C412 as a reference, C470 with addition of zirconium and C471 with zirconium and chromium. Detailed composition is given in Table 2.1.

Materials were prepared by twin-roll casting (see section 1.6 on page 34 for details) in industrial conditions to strips with thickness of 8 mm (normal direction – ND), width approximately 1 m (transversal direction – TD) and length of several km (rolling direction – RD). The description of the foil directions can be found in Figure 2.1. Furthermore, the thickness of the cast foils was reduced by cold-rolling in several steps to 5 and 1 mm.

All materials were cast and cold-rolled in AL INVEST Břidličná, a.s.

For further reference letters A-I were assigned to all materials according to the type of the alloy and to the foil thickness. The assignment is given in Table 2.2.

2.2 Equal channel angular pressing

In the third experimental part of the work twin-roll cast materials were subjected to severe plastic deformation by equal channel angular pressing.

The ECAP was undertaken with pressing speed 10 mm/min. The route B_C was applied, when the sample is rotated by 90° around its axis (parallel to rolling direction of the foil) after each pass. The cross-section of the ECAP channels was $10 \times 10 \text{ mm}^2$ and the intersection angle of the channels was $\Phi = 90^\circ$. Materials were subjected to 1, 2, 4 and 8 passes at room temperature. The orientation of the TRC foil before and after an ECAP pass is depicted in Figure 2.2. It varies for odd and even passes. The dimensions of the samples before ECAP were 120 mm in RD, 10 mm v TD and 8.5 mm in ND (which is the thickness of the foil after TRC). After the first pass the samples were compactized to have cross-section $10 \times 10 \text{ mm}^2$ in both TD and ND.

Table 2.1: Composition of studied materials C412, C470 and C471 in wt.% (only the main alloying elements).

	Al	Mn	Fe	Si	Cu	Zr	Cr
C412	97.5779	1.00743	0.55754	0.59806	0.14571	0.00149	0.00142
C470	97.6540	1.02449	0.22783	0.58164	0.16209	0.16305	0.00160
C471	97.6863	1.02373	0.19671	0.53209	0.15264	0.16545	0.07491

Table 2.2: Assignment of abbreviation letters to the studied materials according to the alloy and foil thickness.

	8 mm	5 mm	1 mm
C412	A	B	C
C470	D	E	F
C471	G	H	I

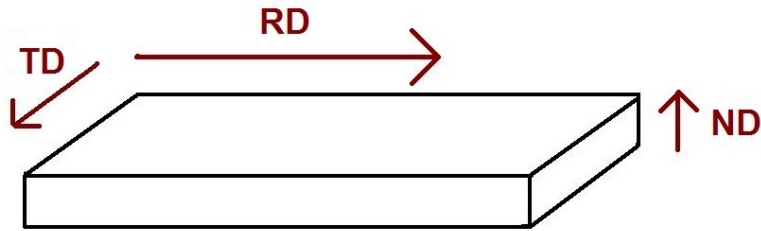


Figure 2.1: Directions used to describe twin-roll cast foils: rolling direction RD parallel with the direction of casting, transversal direction TD and normal direction ND perpendicular to the foil surface.

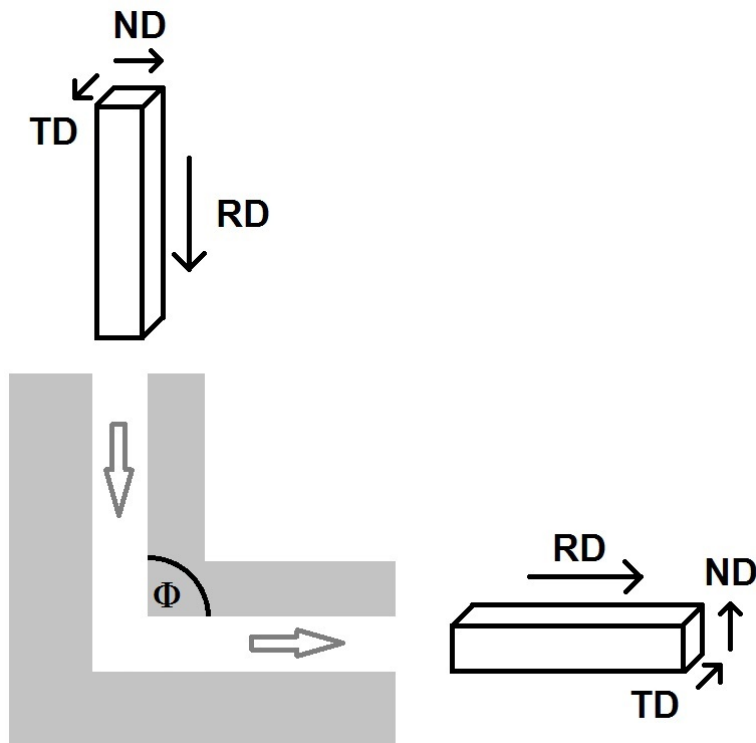


Figure 2.2: Directions of the samples before and after ECAP. The pressing direction is parallel with the rolling direction, the normal direction and transversal direction alternate for even and odd passes. The scheme is for an odd pass.

3. Experimental

Several experimental techniques were used to investigate microstructure (light optical microscopy – LOM, transmission electron microscopy – TEM and scanning electron microscopy – SEM), mechanical properties and phase transformations (electrical resistivity, differential thermal analysis – DTA, Vickers microhardness and tensile testing and).

For mechanical testing and microscopy observations samples were cut by electrical saw Accutom-50, brushed on SiC brushing papers and polished with diamond suspensions.

Usually the observations and measurements were done at the plane perpendicular to transversal direction.

3.1 Heat treatment

To monitor evolution of microstructure and properties of the materials during heat treatment, samples were annealed in air furnaces at different temperatures for miscellaneous times. Three main heating schemes were used:

- Isochronal annealing
- Isothermal annealing
- Gradual heating

The scheme of isochronal annealing is given in Figure 3.1. Sample is inserted into furnace preheated to required temperature for a defined time period. Afterwards the sample is quenched into cold water. The furnace temperature is increased by a required step and the sample is annealed again for the same time period. This procedure repeats up to the highest temperature of interest.

During isothermal annealing the furnace is preheated to a given temperature. The sample is held in the furnace for different time intervals and at the end of each interval the sample is quenched into cold water.

Gradual heating is applied when the temperature in the furnace is linearly increasing with a given rate, for example 5 K/min. The samples can be quenched just after reaching the final temperature or held at this temperature for a desired period of time. Another possibility for gradual heating is in differential scanning calorimeter (DSC), where the heating scheme is set up by a computer. In this work calorimeter DSC 404C from Netzsch was used.

3.2 Electrical resistivity

Measuring of electrical conductivity or resistivity can provide us information about solid solution decomposition via precipitation or phase transformation or enrichment of solid solution via dissolution of dispersoids during heat treatment. Resistivity annealing spectra is negative normalized differentiation of resistivity changes during annealing. Peaks then represent precipitation and valleys are connected with particles dissolution (e.g. [26]).

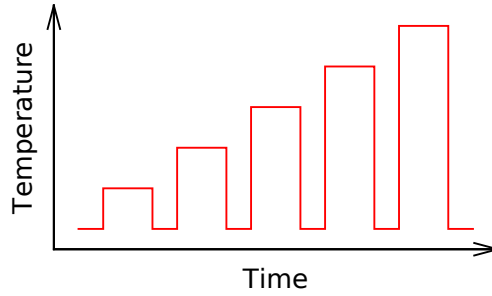


Figure 3.1: Time scheme of isochronal annealing with increasing annealing temperatures.

Table 3.1: Dimensions of the samples for resistivity measurements in the rolling direction, normal direction and transversal direction, in [mm].

Foil thickness	RD	ND	TD
8 mm	100	8.5	1.2
5 mm	100	4.6	2.5
1 mm	100	1	10
ECAP – 10 mm	100	10	1

Four point measurement [124] was used with a dummy specimen in series and applied current was 0.5 A or 0.2 A.

In order to measure the evolution of resistivity, samples were isochronally annealed with step 20 K/20 min from room temperature (RT) to 620 °C. All measurements were undertaken in a bath of liquid nitrogen to minimize the temperature dependent part of the resistivity.

For each sample and each temperature, resistance R of the material was obtained via measurement of electrical current I and voltage U . From the received values resistivity annealing spectra was calculated. It is a negative normalized derivation of resistivity ρ with respect to the temperature T :

$$-\frac{1}{\rho_0} \frac{d\rho}{dT}. \quad (3.1)$$

Normalization was done with the respect to the value before annealing ρ_0 .

The materials were cut into a shape of a strip and electrical contacts were realized at the ends (H-shape depicted in Figure 3.2a). The length of the strips was approximately 100 mm, the size in ND was given by the thickness of the foil and the size in TD was chosen in accordance with the foil thickness so as the cross section was the same for all the thicknesses. Specimens dimensions are displayed in Table 3.1.

3.3 Differential thermal analysis

During differential thermal analysis (DTA) studied material is placed into a holder equipped with thermocouple. Sample undergoes thermal cycle and temperature

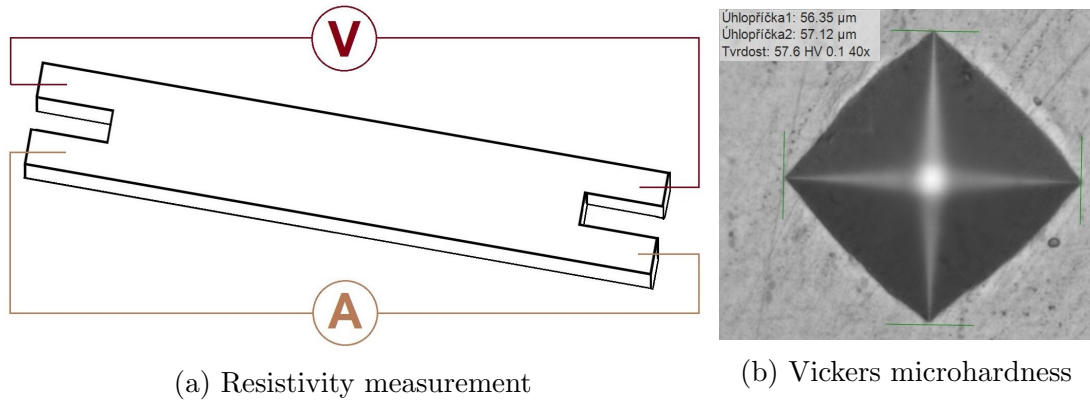


Figure 3.2: H-shape specimen for resistivity measurement with contacts for measurement of electrical current (ampermeter A) and voltage (voltmeter V) and example of microhardness indent with evaluation of the trace dimensions and final value of HV .

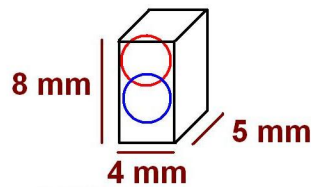


Figure 3.3: As-cast material, positions for cutting the cylinder for DTA: blue circle for center of the foil, red circle for the edge.

difference between studied sample and inert reference is recorded. Endothermic and exothermic changes related to phase transformations are detected, thus, DTA can be used to detect temperature region of precipitation.

For all measurements of DTA in SETARAM SETSYS 16/18 apparatus the specimens had a cylindrical shape with diameter 3.8 mm. Firstly, the heating rate 10 K/min was employed. To ensure similar weight of all samples (approximately 25 mg) the thickness of the cylinders was 1 mm, to match size of material cold-rolled to 1 mm. The axes of the cylinders were in ND for as-cast material, in the RD for material cold-rolled to 5 mm and, finally, in TD for 1 mm foils. From 8 and 5 mm foils the cylinders were cut from the central part of the thickness.

In order to obtain stronger signal, heating rate 5 K/min was applied at bigger samples. Cylinders with thickness 5 mm and mass approximately 130 mg were cut from 8 and 5 mm foils. Two samples came from each as-cast material: one from the center and one from the edge, see Figure 3.3. As for materials cold-rolled to 1 mm, more pieces were cumulated to obtain higher mass.

To move closer to real manufacturing conditions, specimen cold-rolled to 5 mm was subjected to heat treatment with heating rate 1 K/min.

3.4 Microhardness

To evaluate mechanical properties of the materials Vickers microhardness (HV) method was used. During the measurement an indent with pyramidal shape is applied on the material with a force F for a time t and the dimensions of the indents trace are measured. The value of the microhardness HV can be expressed as

$$HV = 0.189 \cdot \frac{F}{d^2} \quad (3.2)$$

where d represents the length of the diagonals of the indents trace (Figure 3.2b).

In this work the load of $F = 100 \text{ g}$ for $t = 10 \text{ s}$ was used on microhardness testers Leco M-400-A Hardness Tester and QNess 10A+. The second one allows automatic measurement and mapping.

For microhardness measurements the samples were brushed by SiC brushing papers and polished by diamond suspension.

3.5 Tensile tests

For tensile testing the specimens were cut to length of 40 mm in RD and thickness 1 mm in TD and then were milled to a dog-bone shape. The tensile tests were undertaken at room temperature at INSTRON 5882 with strain rate 10^{-3} s^{-1} , which corresponds to cross head speed 1 mm/min. Measurements for superplasticity were undertaken at elevated temperatures from 350 °C to 450 °C with various strain rates.

3.6 Light optical microscopy

Light optical microscopes Olympus PMG3 and Olympus GX51 were used to monitor evolution of primary particles distribution and grain sizes. For observation of particles in plain light polished samples were etched with water solution of 0.5 % HF for 10 s. Grains were observed in polarized light after electrolytical oxidation in \odot 35 % HBO_4 solution (Barker solution) for 3 minutes at 20 V. Micrographs were taken in the plane perpendicular to the transversal direction.

3.7 Scanning electron microscopy

Scanning electron microscope provides information about surface layer of studied materials. The electron beam is issued from an electron gun and interacts with the sample. By detecting the secondary electrons (SE) emitted from the sample we can obtain surface morphology. Thanks to the back-scattered electrons (BSE) chemical contrast is revealed. The higher is the atomic number of an element the more electrons are scattered by this element. Due to this phenomena phases with higher average atomic mass appear lighter.

By detection of diffracted back-scattered electrons (EBSD) the orientation of the matrix can be determined. The diffracted electrons form Kikuchi pattern on a phosphor screen, which is captured by CCD camera. By Hough transformation the orientation of each element of the sample surface is determined. The grain

boudaries are calculated from misorientation between each two points. High angle grain boundaries are considered for points with missorientation higher than 15° , low angle grain boundaries are between 5° and 15° . Another possibility of EBSD is the capability to dictinct different crystallographic phases.

Energy-dispersive X-ray spectroscopy (EDS) helps to evaluate which elements are present in the investigated area of our material by detecting energies of X-rays emitted from the material. These energies are characteristic for each element. By comparing relative intensity of signal for each energy the ratio of elements can be obtained.

In this work BSE was used to depict the structure of different phases, EDS to characterize elements contained in them and EBSD to monitor grain size and phases distribution. Microscopes LEO 435VP and FEI Quanta FEG 200 were used.

For BSE and EDS the samples were brushed and polished with diamond suspension, for EBSD they were futher polished by Masterprep (for determination of crystallographic phases) or electrolytically polished by \odot 33 % nitridic acid in methanol at -19°C with 15 V for 10 s in LectroPol 5.

3.8 Transmission electron microscopy

In this work transmission electron microscope JEOL JEM 2000FX with accelerating voltage 200 kV was utilized to monitor microstructure and its evolution in all studied materials. Observations in bright field (BF), dark field (DF) and electron diffraction (SAED) were applied.

This microscope is equipped with aparature AM-SHU2 for in-situ heating, which enables observations at different temperatures.

The foils for observation in TEM were thinned by brushing papers to 0.15 mm and electrolytically etched at Tenupol-2 or Tenupol-5 by \odot 33 % nitridic acid in methanol at -19°C with 15 V and 200 mA.

Part II

Material characterization

4. Electrical Resistivity

Firstly, electrical resistivity of all material was measured to evaluate the temperature ranges of major changes in microstructure. For the measurement all samples were isochronally annealed with step 20 K/20 min from RT to 620 °C.

The resistivity annealing spectra are shown in Figure 4.1. All materials exhibited two local maxima which corresponded to precipitation, one of them was more pronounced than the other. No substantial differences were observed between the three different alloys for thicknesses 8 and 5 mm. In the Zr-free material after cold-rolling to 1 mm the first peak in positive values in resistivity spectra started at lower temperature and reached lower maximal value. However, the area under the precipitation peaks was the same for all three 1 mm materials.

The temperature of the main precipitation shifted to lower temperatures with rolling. Higher stored deformation energy and higher dislocation density led to higher driving force for precipitation. In the cold-rolled materials, first region of precipitation was more pronounced than the second one, as opposed to the as-cast materials, where the main region of precipitation was detected at higher temperatures. Temperatures of the maxima were summarized in Figure 4.2.

All materials exhibited a global minimum at 580 °C. This was the temperature of main dissolution of precipitates back to the solid solution.

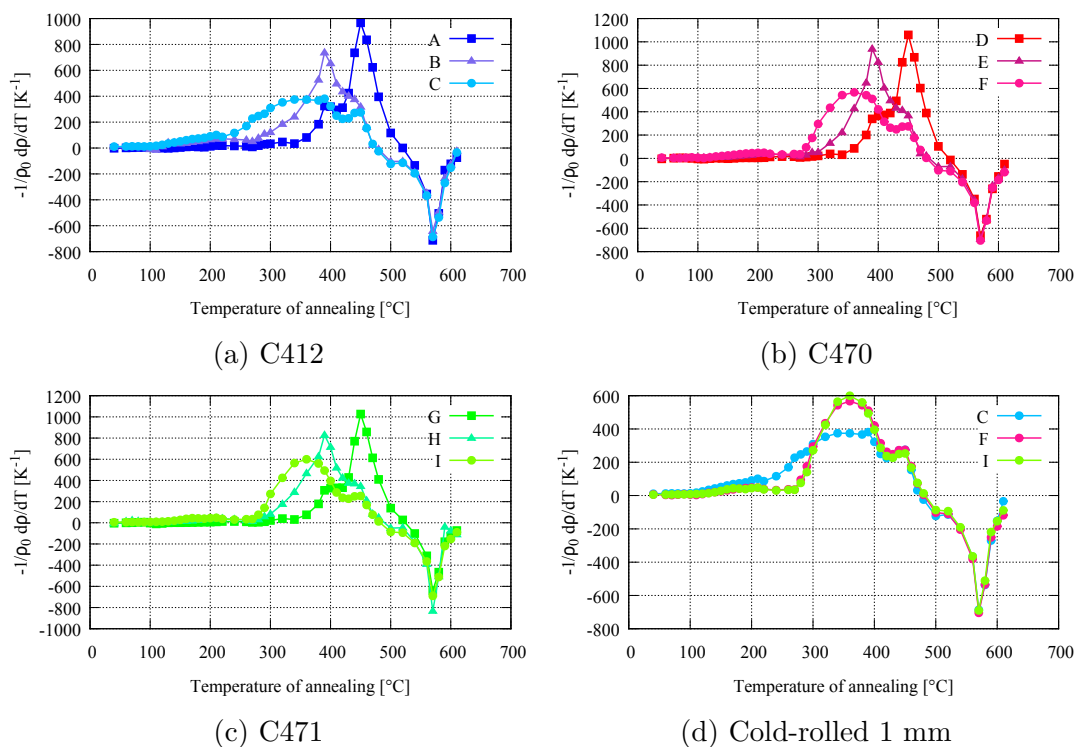


Figure 4.1: Resistivity annealing spectra of all materials for different foil thicknesses and comparison of materials after cold-rolling to 1 mm.

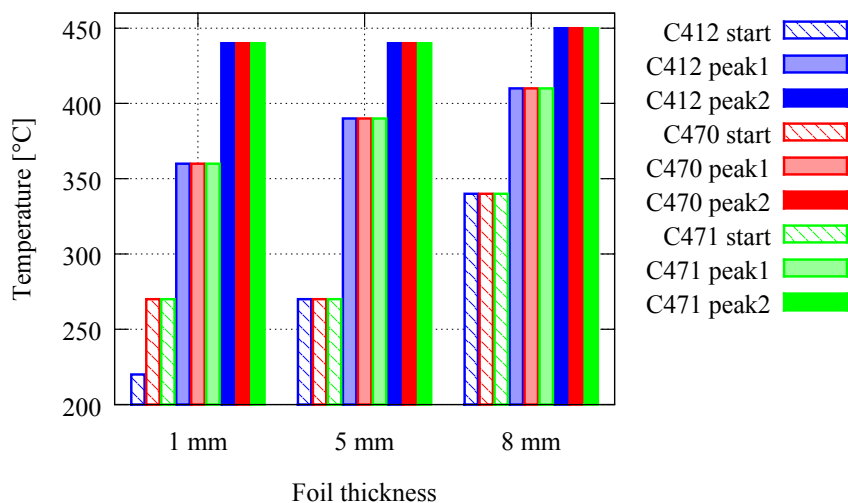


Figure 4.2: Temperatures of start and maxima of precipitation peaks in resistivity annealing spectra.

5. Differential thermal analysis

Differential thermal analysis was measured on all materials at three different heating rates in order to detect temperature intervals of phase transformations and to evaluate the role of the heating rate. These results were compared with measurement of electrical resistivity.

5.1 Heating rate 10 K/min

During heating with rate 10 K/min small peaks were detected in the course of the first cycle at high temperatures of the spectra. These did not occur during second cycle and were thus attributed to precipitation or phase transformation processes.

The temperatures of start and maximum of transformations were lower for cold-rolled materials as compared to the as-cast state. The influence of composition was hard to evaluate because of low signals, the temperatures of precipitation did not vary significantly. Obtained values were plotted in Figure 5.1a.

5.2 Heating rate 5 K/min

Thanks to higher mass of the samples the peaks in DTA spectra around 450 °C were more pronounced during heating with rate 5 K/min. In all materials the main precipitation started earlier in foils cold-rolled to 5 and 1 mm. The edge of as-cast materials followed and the precipitation started in the center of as-cast materials at even higher temperatures.

The differences between materials were not very significant. The precipitation started earlier in material C412 without Zr and Cr, but it reached its maximum at the same temperatures as materials with Zr and Cr, see Figure 5.1b.

In all materials one smaller peak occurred at lower temperatures around 350 °C. This was probably due to another precipitation reaction preceding the one detected also for samples with lower mass (during heating 10 K/min). Its presence was in agreement with resistivity measurements (see page 56). However, evolution of its position as a function of foil thickness showed a different trend as compared to the major peak. The precipitation temperature was now the same both for the edge and center of the as-cast materials. Its position shifted to lower temperatures with cold-rolling to 5 mm and reached even lower values at thickness of 1 mm. The only significant difference between materials could be recognized at 1 mm samples, where the peak temperature of material C412 without Zr and Cr was by 30 °C lower than in material C470 with Zr.

The shift of precipitation to lower temperatures after cold-rolling can be attributed to higher density of dislocations introduced to the material during deformation. Dislocations then can serve as preferable nucleation sites for precipitation and they accelerate precipitation kinetics. This phenomenon would clarify earlier onset of precipitation in 1 mm foils.

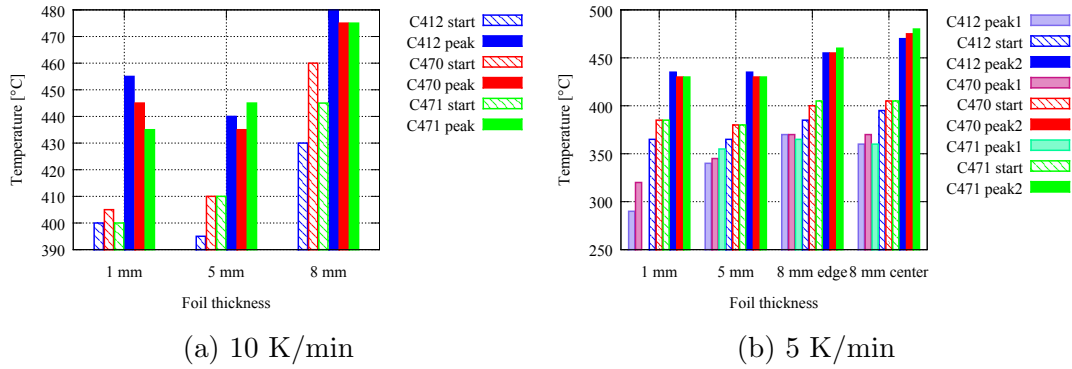


Figure 5.1: Temperatures of start and maximum of precipitation peaks during heating with rate 10 K/min and of first small maximum (peak1), local minimum (start) and major maximum (peak2) in DTA spectra during heating with rate 5 K/min in different materials.

5.3 Heating rate 1 K/min

Signal during heat treatment with heating rate 1 K/min was less pronounced than the one from heating rate 5 K/min. Only one precipitation peak was distinguishable; in materials cold-rolled to 5 mm it started at 355 °C and reaches maximum around 385 °C, which was by 50 °C lower than for heating rate 5 K/min.

5.4 Influence of heating rate

As for the influence of the heating rate on the temperature of the transformations, only a moderate shift of the precipitation to lower temperatures was recognizable in cold-rolled samples, mainly in those with thickness 1 mm. For detailed information see Figure 5.2a. This would be in correspondence with literature, transformations can start at lower temperatures when treated with lower heating rates, e.g. [26]. The inhomogeneity of the shift for different materials (e.g. in the as-cast state of material C471 the temperature of the main peak was higher for heating rate 5 K/min) was attributed to the difficulties with evaluating the peak position in the case of heating rate 10 K/min; the peaks were not enough pronounced to distinguish easily their maximum.

If we take into account the heating rate 1 K/min, the shift of precipitation to lower temperatures will be more significant.

5.5 DTA vs. electrical resistivity

Both DTA and electrical resistivity measurements gave us information about precipitation processes in the material. For measurement of electrical resistivity samples were isochronally annealed with step 20 K/20 min. In the as-cast foils minor transformation was detected at temperatures around 400 °C and major one at 450 °C. In the cold-rolled foils the magnitude of transformations was opposite: major peak occurred at lower temperatures around 390 °C and minor one around 450 °C. Peak in negative values at 570 °C was detected in all materials.

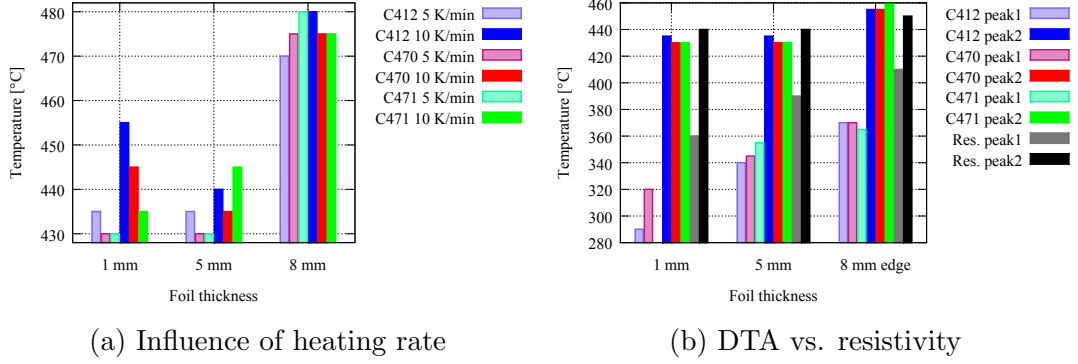


Figure 5.2: (a) Influence of heating rate on temperature of major precipitation peak. (b) Temperatures of first small maximum (peak1) and major maximum (peak2) in DTA spectra during heating with rate 5 K/min compared with peaks in resistivity annealing spectra. Peaks at higher temperatures were in accordance; first peaks show discrepancy.

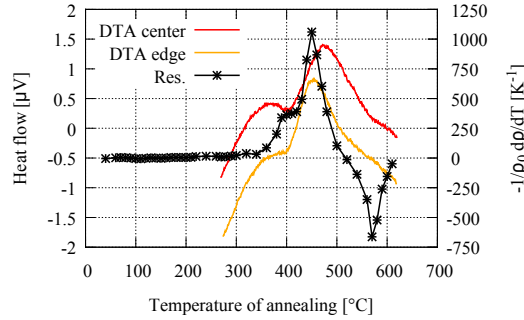


Figure 5.3: Comparison of DTA and resistivity annealing spectra for as-cast material C470, edge and central part. Only temperature of the second peak was in agreement, temperature of the first peak was lower in DTA.

As for difference between DTA and resistivity spectra, the temperatures of second precipitation were in good agreement (Figure 5.2b). For as-cast state the temperatures in resistivity annealing spectra corresponded to the edge part of the foil, temperature for central part was higher (Fig. 5.3).

Temperatures of the first precipitation peaks showed a discrepancy: the position of the peak for the as-cast materials was around 360 $^{\circ}\text{C}$ for DTA and 400 $^{\circ}\text{C}$ for resistivity. However, it exhibited the same trade concerning the decrease of the temperature with increasing cold-rolling deformation.

Furthermore, the magnitude of the peaks for cold-rolled specimens was reversed: in DTA spectra the second peak was higher whereas in resistivity spectra the first one prevailed (see Figure 5.3). This disagreement may be caused by the difference in applied heat treatment: isochronal step annealing may not reproduce what happens during industrial heat treatment which was a continuous one like in DTA.

The heating rate of the measurements was different too, 1 K/min for resistivity (20 K/20 min respectively) and 5 or 10 K/min for DTA.

6. Vickers Microhardness

6.1 Initial states

The distribution of Vickers microhardness values of the as-cast materials was measured (see Fig. 6.2). In planes perpendicular rolling and transversal direction the HV was slightly higher near the surface of the foil. In some regions, there was a high HV value in the central part of the foil. The microhardness was comparable for both planes and was slightly higher in materials with Zr – C470 and C471.

6.2 Isochronal annealing

Concerning heat treatment, specimens for microhardness measurements were treated in the same manner as for resistivity measurements – isochronal annealing 20 K/20 min from RT to 620 °C. The results are shown in Figure 6.3.

Cold-rolled materials exhibited higher values of microhardness as compared to the as-cast states, which corresponded to the deformation hardening thanks to higher dislocation density. The highest HV value at RT was observed in material C471 with addition of both Zr and Cr for all thicknesses. During annealing its value was sometimes exceeded by HV of material C470 with addition of only Zr. The HV of alloy C412 without Zr and Cr remained the lowest during all annealing steps as compared to the other materials with corresponding thickness.

The HV of the as-cast states did not change significantly during the heat treatment. As for the materials C470 and C471 with additional elements, increase in hardness by 20 % was observed at high temperatures, the maximum was located at 520 °C. The HV of cold-rolled materials slowly dropped during annealing due to recovery and a significant drop occurred at high temperatures, earlier for materials with higher stored deformation energy – cold-rolled to 1 mm. Such pronounced drop is known to be connected with recrystallization (e.g [66, 67]). The temperatures of start and end of recrystallization are plotted in Figure 6.1.

Material C412 without Zr addition and cold-rolled to 1 mm was the first one to recrystallize.

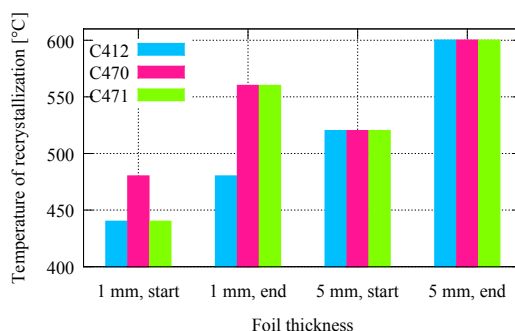


Figure 6.1: Temperatures of start and end of recrystallization of cold-rolled materials from microhardness measurement.

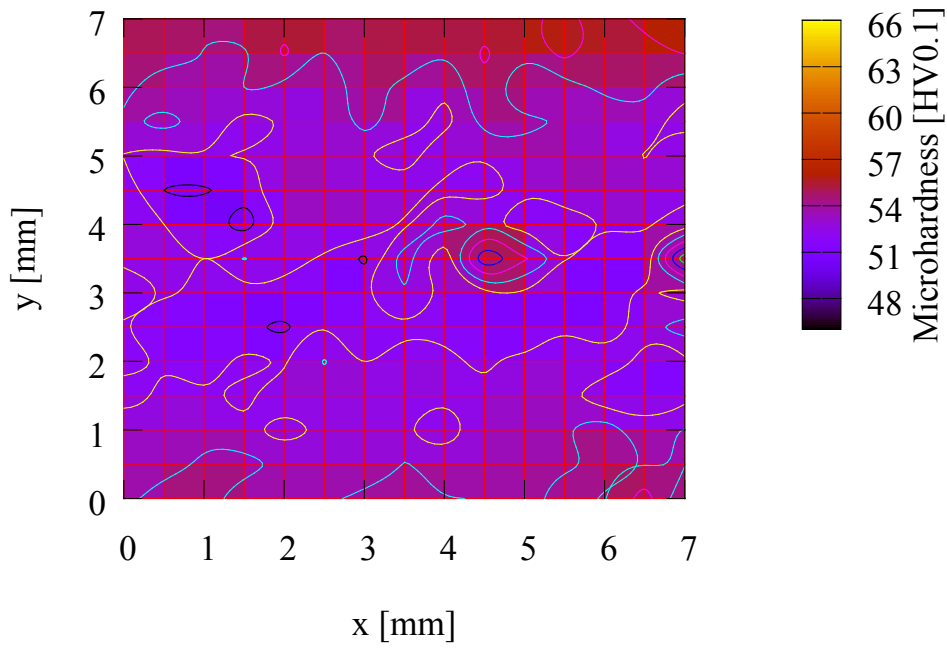
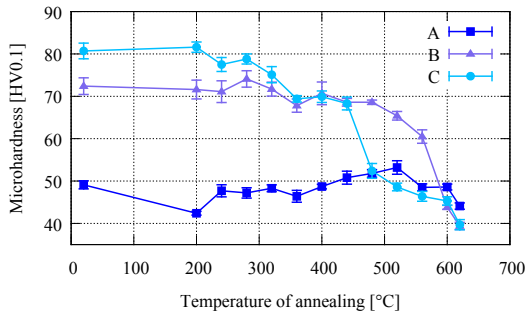
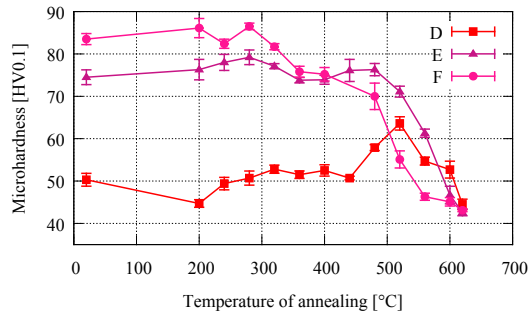


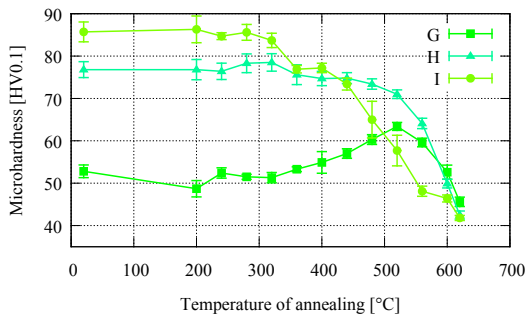
Figure 6.2: Vickers microhardness of as-cast material C470 in plane perpendicular to RD; ND was vertical.



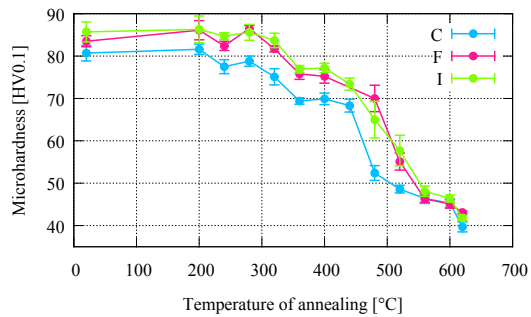
(a) C412



(b) C470



(c) C471



(d) Cold-rolled 1 mm

Figure 6.3: Microhardness evolution during isochronal annealing 20 K/20 min of all materials and comparison of foils cold-rolled to 1 mm.

7. Light optical microscopy

7.1 Phases

Samples observed by the light optical microscope were the initial states (as-cast and cold-rolled) and samples isochronally annealed to 620 °C with step 20 K/20 min. The micrographs were taken in the plane perpendicular to TD.

As-cast

Bands of macro-segregated eutectic colonies were observed in materials with Zr (and Cr) additions – C470 and C471, both in as-cast and annealed states. They were positioned mainly in the central line of the foils in the rolling direction, sometimes in more lines. Their length was in magnitude of mm, thickness 30 μm (Figure 7.1). The cold-rolling did not influence their presence. They were not detected in material C412.

In the central part of C412 primary particles (PP) were segregated into small elongated groups with size 10-20 μm (Figure 7.2a). Inbetween them dark primary particles with size in magnitude of μm were found. The small segregates were also present at the edges, however, they were ordered in linear chains. After annealing to 620 °C primary particles in the center were still segregated. New precipitates occurred during annealing between PP. More of them were in the center; higher number of PP was near the edges. In the vicinity of PP, precipitation free zones (PFZ) were found.

In the C470 material lot of PP were located near the edges, partly ordered in the rolling direction, probably at the grain boundaries. Their number density decreased near the center, where the macro-segregation was present. Several small segregates like in C412 were found near the center. The PP in the center were randomly distributed. After annealing to 620 °C, PP were ordered in the rolling direction near the edges, their number decreased but their diameter increased as compared to the initial state. Their number density was a bit smaller than in C412. Most of the small segregates disappeared. A lot of new precipitates occurred, more than in material C412 without Zr. PFZ were observed around PP.

In the alloy C471, PP near the edge were ordered in the casting direction. In the center the distribution was more random, but some of the PP even here were lined in the casting direction. Some gray particles were present near the center. The number of PP was approximately the same as in C470; their number density was higher near the edges. Some small segregations like in C412 were detected (next to the macro-segregation), but they disappeared during annealing. Like in the other two alloys, lot of precipitates and PFZ occurred, their number was comparable with C470.

Cold-rolled

After cold-rolling to 5 mm, the microstructure of C412 did not change significantly. During annealing precipitates formed, but mainly near the center and

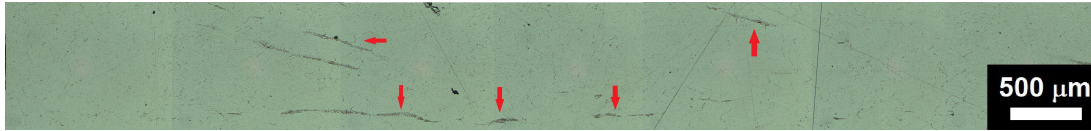
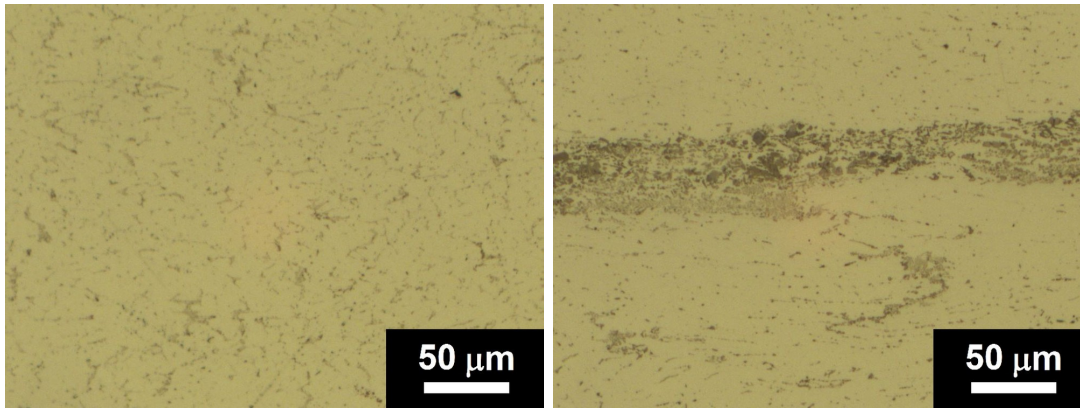


Figure 7.1: Central segregates in material C470 in the as-cast state (marked by arrows).



(a) C412, as-cast

(b) C471, cold-rolled 5 mm

Figure 7.2: Central part of the as-cast material C412 with small colonies of primary particles and material C471 after cold-rolling to 5 mm with central eutectic segregation.

their number was lower as compared to the as-cast material after annealing. After rolling to 1 mm, the central segregates were parallel to the RD, unlike in the 5 mm sample, their number was higher near the center. After annealing the number of particles increased.

In the C470 material after rolling to 5 mm, the number of PP was comparable with the as-cast state at the edges and a bit higher in the center, where no small segregates were found. The PP were partially ordered in the RD. After annealing the number of precipitates at the edge was lower than in as-cast material after annealing and comparable in the central part. The number of PP did not change in the course of annealing. The 1 mm foils exhibited low number of PP at the edges and higher in the center, where they were ordered in the RD. After annealing a lot of precipitates occurred. The number of PP was lower than in C412 material.

After cold-rolling of the C471 material (Figure 7.2b), the microstructure did not vary very much. After annealing to 620 °C, the number of PP did not change. The number of precipitates was comparable with the as-cast material after annealing at the edge, but lower at the center. The sample cold-rolled to 1 mm contained slightly more PP than material C470. The number of precipitates after annealing was comparable with the material C470.

Table 7.1: Size of the grains in the center of the samples in the rolling and normal direction, in [μm].

As cast:

C412	RD	ND	C470	RD	ND	C471	RD	ND
8 mm	100	50	8 mm	500	150	8 mm	400	100
5 mm	300	30	5 mm	800	80	5 mm	600	50
1 mm	500	10	1 mm	1000	20	1 mm	1000	10

Annealed to 620 °C:

C412	RD	ND	C470	RD	ND	C471	RD	ND
8 mm	100	50	8 mm	300	80	8 mm	300	80
5 mm	50-200	50-100	5 mm	50-200	50	5 mm	50-200	50-100
1 mm	200	30-100	1 mm	20-200	10-50	1 mm	30-100	50-200

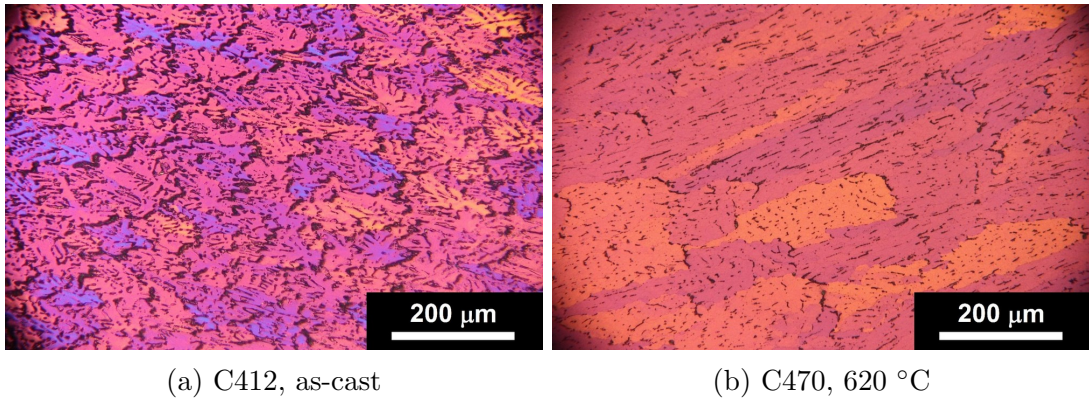


Figure 7.3: Grain structure of material C412 after twin-roll casting and material C470 annealed to 620 °C.

7.2 Grains

Material C412 without Zr and Cr had smaller grains than materials with additional elements (Figures 7.3a and 7.3b). Grain sizes of C470 and C471 were comparable.

All materials exhibited different grain structures at the edges and in the central parts. This phenomenon was caused by rolling component of twin-roll casting and further by cold-rolling. Grains near the edges were more flat and elongated in the rolling direction; however, not parallel to the surface.

After cold-rolling the grains became more flat, elongated in the rolling direction, parallel to the surface. The inhomogeneity through the foil thickness remained apparent (Figure 7.5). After annealing new recrystallized grains occurred in cold-rolled samples (see Figures 7.4 and 7.6), the ones at the edges of 1 mm samples sometimes with length in RD in magnitude of mm, in ND 100 μm .

The average grain sizes are summarized in Table 7.1.

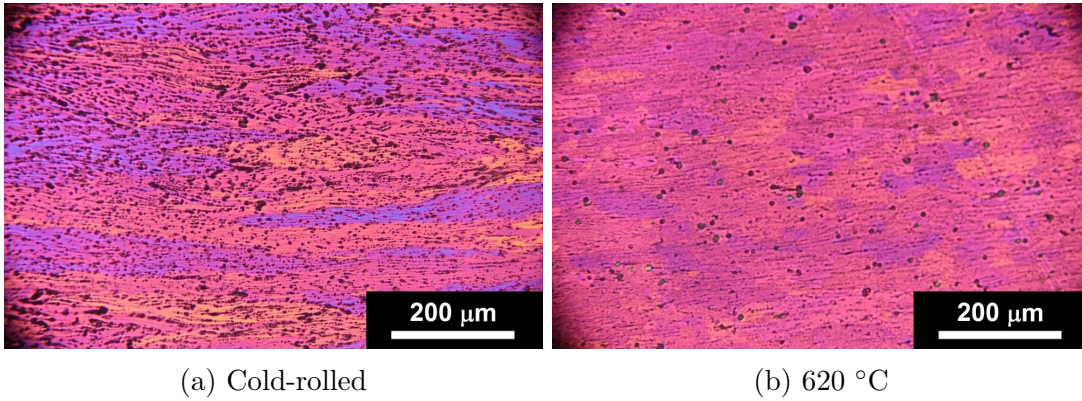


Figure 7.4: Grain structure of material C470, cold-rolled to 5 mm and subsequently annealed to 620 °C.

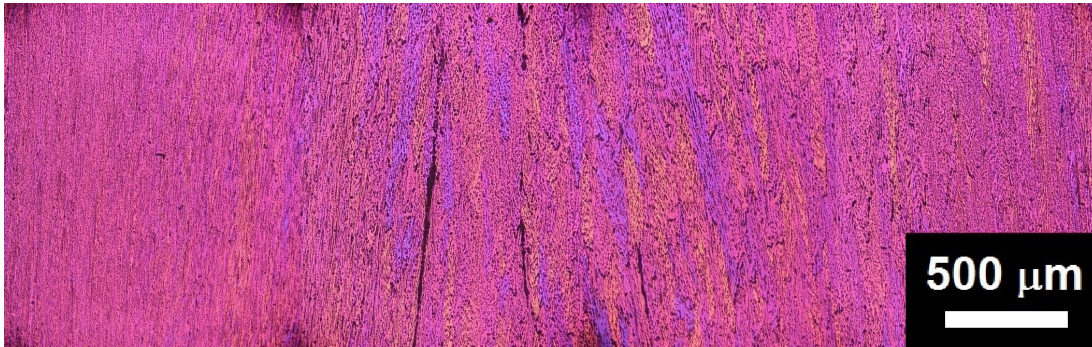


Figure 7.5: Grain structure of material C471 cold-rolled to 5 mm with larger grains and macrosegregation in the central part. RD is vertical.

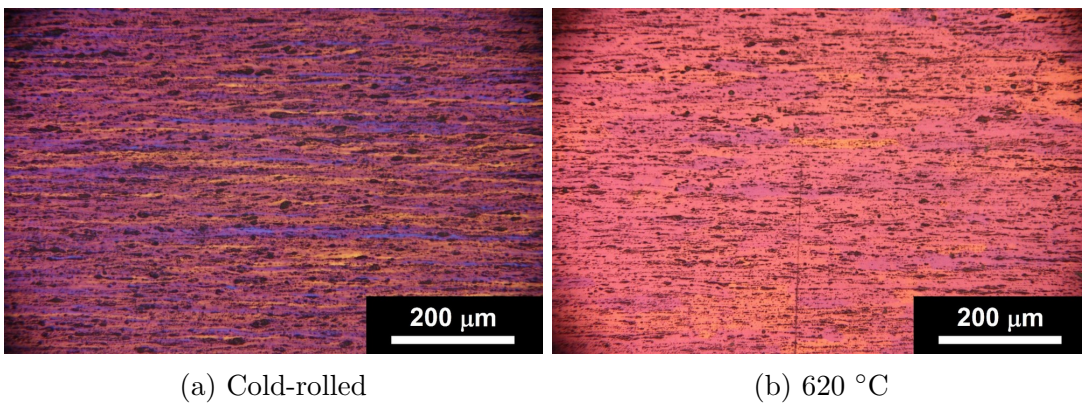


Figure 7.6: Grain structure of material C412, cold-rolled to 1 mm and subsequently annealed to 620 °C.

8. Scanning electron microscopy

8.1 Back-scattered electrons

Temperatures for SEM observations were chosen according to DTA measurements. For 8 mm foils temperature 400 °C corresponded to the beginning of major peak and 500 °C to end of this peak. As-cast state and final state after annealing to 620 °C were also examined. The SEM images were obtained in BSE and chemical analysis was performed by EDS.

Initial state

In material C412 with no Zr and Cr additions and higher content of Fe, primary particles were clustered in dendritic colonies with eutectic features (Figure 8.1a). Most of them were elongated with width smaller than 1 μm and length around 30 μm . However, some of them near the center of the foil were larger with width approximately 3 μm . Near the edges of the foil some of the eutectic colonies were oriented in the direction of solidification and they probably copied the grain boundaries. EDS analysis revealed that eutectic colonies correspond probably to α -phase $\alpha\text{-Al}_{12-15}(\text{Mn,Fe})_3\text{Si}_{1-2}$ but the presence of Cu was also detected. The amount of iron was slightly higher than of manganese and lower than the amount of silicon. As for the composition of the matrix only small peak of manganese was detected.

In material C470 with addition of Zr eutectic macrosegregation in the central part of the foil appeared (Figure 8.1b). Its size was approximately 50 μm in width and its length was in order of hundreds of μm . However, near the edges of the foil primary particles were either ordered in chains copying grain boundaries or were present as single sub-micron spherical particles (Figure 8.2a). In the central part in the vicinity of the eutectic colonies some coarse particles formed (with diameter approximately 2 μm). Detail of these particles (Figure 8.2b) revealed multiphase composition. At the edges of some α -phase particles phases with higher average atomic number were observed. EDS analysis revealed that the additional phases contained mainly Cu and small amount of Si and Ni. The lightest contained probably Zr (however, the best fit of the spectra was Pb which was not contained in our materials). The α -phase particles contained more Mn than Fe (opposite trend than in material C412) and even more Si. Next to aluminium, only small amount of manganese was detected in the matrix, both near the center and the edge of the foil.

Material C471 with additional Zr and Cr did not show many differences from material C470 without Cr when it comes to the distribution of primary particles and central segregation. However, EDS showed minor contribution of Cr to the spectra. According to literature, Cr can substitute for Fe and Mn in the α -phase to create $\alpha\text{-Al}_{12-15}(\text{Mn,Fe,Cr})_3\text{Si}_{1-2}$. In the analyzed particle the amount of Mn and Fe was nearly the same, but the level of Si was higher than in the material C470.

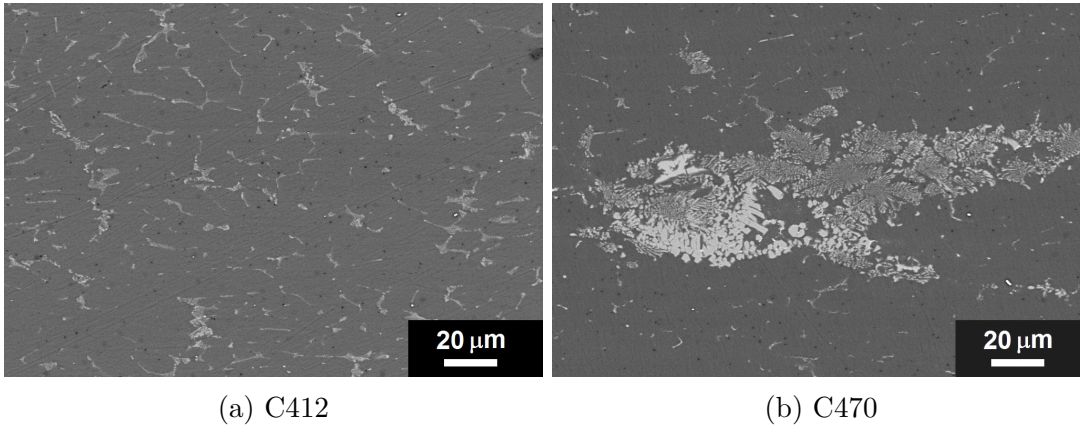


Figure 8.1: Dendritic colonies with eutectic features in the center of the as-cast foil in C412 alloy and macrosegregation in C470.

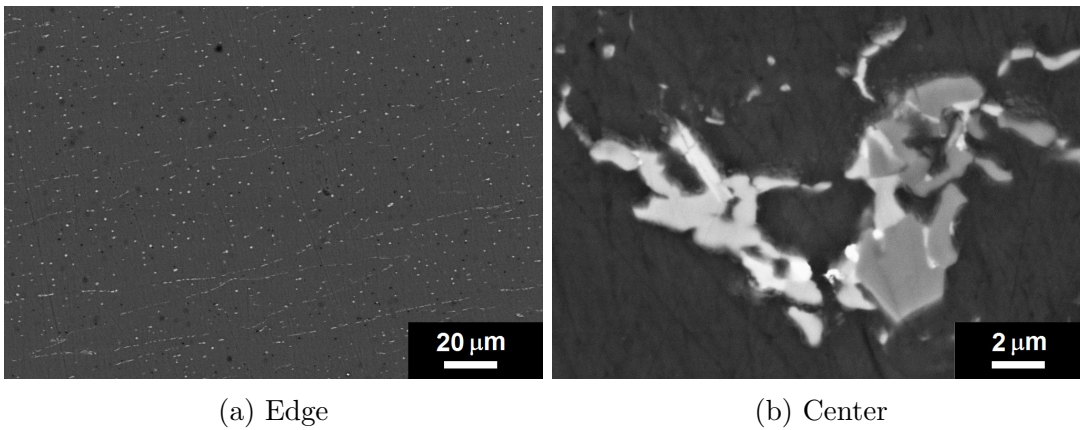


Figure 8.2: Primary particles near the edge of the foil aligned with the grain boundaries and detail of a multi-phase macrosegregation in the center, both in alloy C470 with Zr.

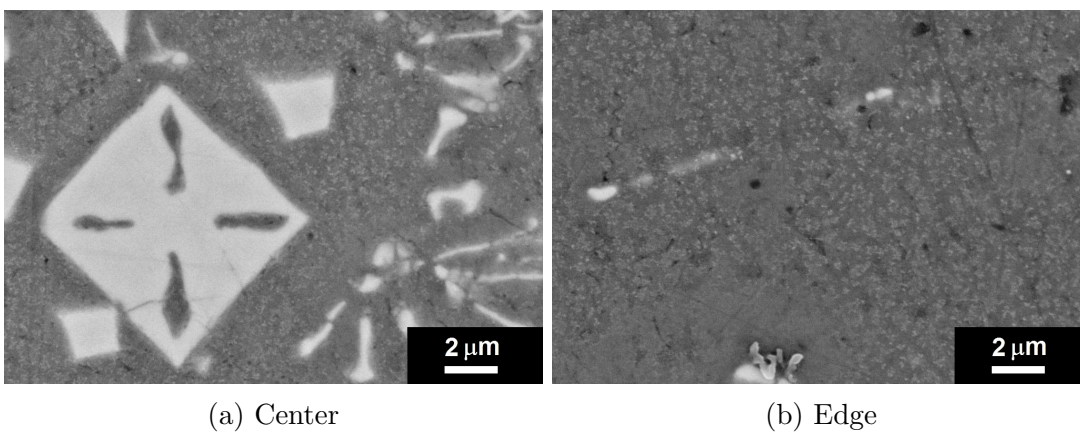


Figure 8.3: High density of new fine particles between the central segregation and near the edge of the foil in C470 alloy annealed to 500 °C.

Annealing to 400 °C

After annealing to 400 °C, material C412 seemed to have lower density of particles. However, this fact may be caused by different position from the edge of the observed foil - according to observations in light optical microscope, the number density of primary particles decreased from the edge to the center of the foil. α -phase still contained more Fe than Mn.

Multiphase particles in C470 material were still present: α -phase with smaller particles containing Cu, Zr and Ni attached to it. As for the α -phase composition, Mn slightly prevailed over Fe, but Si prevailed over both. Outside the central eutectical colonies primary particles were in a form of small clusters or solitary circular particles.

In C471 α -phases contained more Mn than Fe like in C470 alloy. Moreover, the Mn content differed in individual particles. At boundaries of the coarse α -particles (diameter around 4 μm) in the center of the foil small particles with Cu and Ni were occasionally attached.

Annealing to 500 °C

After further annealing to 500 °C high density of new small particles appeared. They were present both inside and outside of the central segregation (Figure 8.3). EDS analysis revealed presence of silicon and manganese in vicinity of these particles.

Annealing to 620 °C

If we compare the microstructure of material C412 after casting and after annealing to 620 °C, the distribution of phases did not evolve significantly – particles were clustered in the central part of the foil and copied grain boundaries near the edge.

Materials C470 and C471 with additional Zr and Cr still contained central segregates after annealing to 620 °C. Quantitative EDS analysis was performed in the material C471. The results given in Table 8.1 showed, that particles in the central segregation (numbers 1 and 2 in Figure 8.4) contained high ratio of Mn and Si atoms, the atomic percentage of Fe was twice lower than the one of Mn. Particle outside the central segregation (number 5) contained approximately the same atomic percentage of Si, Mn and Fe. All of these particles evinced also small amounts of Cr. In aluminium matrix (numbers 3 and 4) only small amounts of Mn and Si were detected.

8.2 Chemical analysis

Mapping of chemical elements (aluminium, manganese, iron, silicon and copper) in central segregation is depicted in Figures 8.5 and 8.6. After twin-roll casting, most of the Mn and Fe were detected within the segregation, Si was detected in clusters outside the segregations and Cu was found mainly in lighter parts of the segregation.

After annealing at 450 °C for 8 hours the majority of Mn and Fe were still in the segregation; however, no traces of silicon or copper clusters were detected, the distribution of Si was more homogeneous, most of it was detected in the

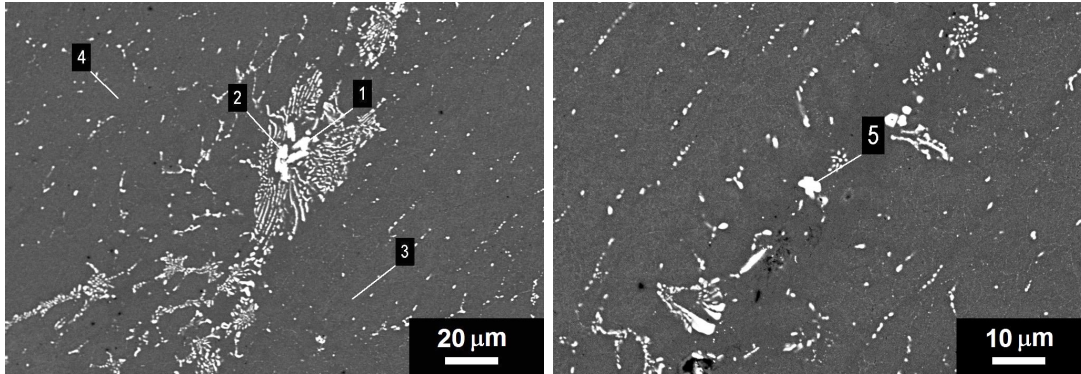





Figure 8.4: C471 8 mm after annealing to 620 °C: Central part of the material with eutectic segregations. Numbers indicate spots, where the quantitative EDS analysis was taken.

Table 8.1: Quantitative results from EDS analysis of C471 alloy after annealing to 620 °C. Numbering of analysis spots was in accordance with Figure 8.4.

Spot	Al		Mn		Fe		Si		Cr	
	wt.%	at.%	wt.%	at.%	wt.%	at.%	wt.%	at.%	wt.%	at.%
1	62.93	74.03	18.47	10.67	9.56	5.43	8.4	9.49	0.64	0.39
2	63.18	74.3	18.18	10.5	9.86	5.6	8.18	9.24	0.6	0.37
3	98.72	99.12	0.73	0.36	0	0	0.53	0.51	0.02	0.01
4	98.29	98.89	1.01	0.5	0	0	0.55	0.54	0.15	0.08
5	62.96	74.28	14.48	8.39	14.21	8.1	7.91	8.96	0.44	0.27

Table 8.2: Phases identified by EBSD in C470 material and their color in figures.

Phase	Structure	Point group	Lattice constant	Color
Al	Cubic	$O_h \bar{m}\bar{3}m$	a = 0.404 nm	
α -Al(Mn,Fe)Si	Cubic	$T_h \bar{m}\bar{3}$	a = 1.2643 nm	
α -Al(Mn,Fe)Si	Hexagonal	$D_{6h} 6/mmm$	a = 1.2406 nm c = 2.6236 nm	

segregation. Point analysis showed ~ 10 at.% Mn, ~ 10 at.% Si and ~ 6 at.% Fe in the segregation.

8.3 Electron back-scatter diffraction

8.3.1 Phases

For identification of crystallographic phases in material C470 electron back-scatter diffraction was applied. Three phases were identified – Al, hexagonal α -Al(Mn,Fe)Si and cubic α -Al(Mn,Fe)Si. More details were given in Table 8.2. All primary phases were identified as cubic α -Al(Mn,Fe)Si, both in the central segregation and near the edges of the foil. After annealing for 8 hours at 450 °C the crystallographic structure of the phases did not change (see Figure 8.7). Precipitates that nucleated in the volume of the grains also may have been of cubic α -phase. However, those situated at subgrain boundaries may have been hexagonal phase (Figure 8.8).

8.3.2 Grains

The grain size and orientation of as-cast and cold-rolled materials were also studied by the means of electron back-scatter diffraction. Only the cubic phase Al of the matrix was evaluated. In the Zr-free material C412 the grains were elongated in the casting direction, with length in order of 100 μm and thickness 30 μm . The grains of the C470 alloy were larger as compared to C412, also aligned in the casting direction – Figure 8.9. Outside the central part of the foil their length was several hundreds of μm and thickness around 50 μm . The orientation inside a grain was not homogeneous; this was connected with the grain substructure and subdivision of individual grains to subgrains.

Cold rolling to 5 mm resulted in further elongation of the grains in casting/rolling direction and reduction of their thickness in normal direction. The inhomogeneous orientation in the grain interior was apparent. The average grain size was still lower in C412 material.

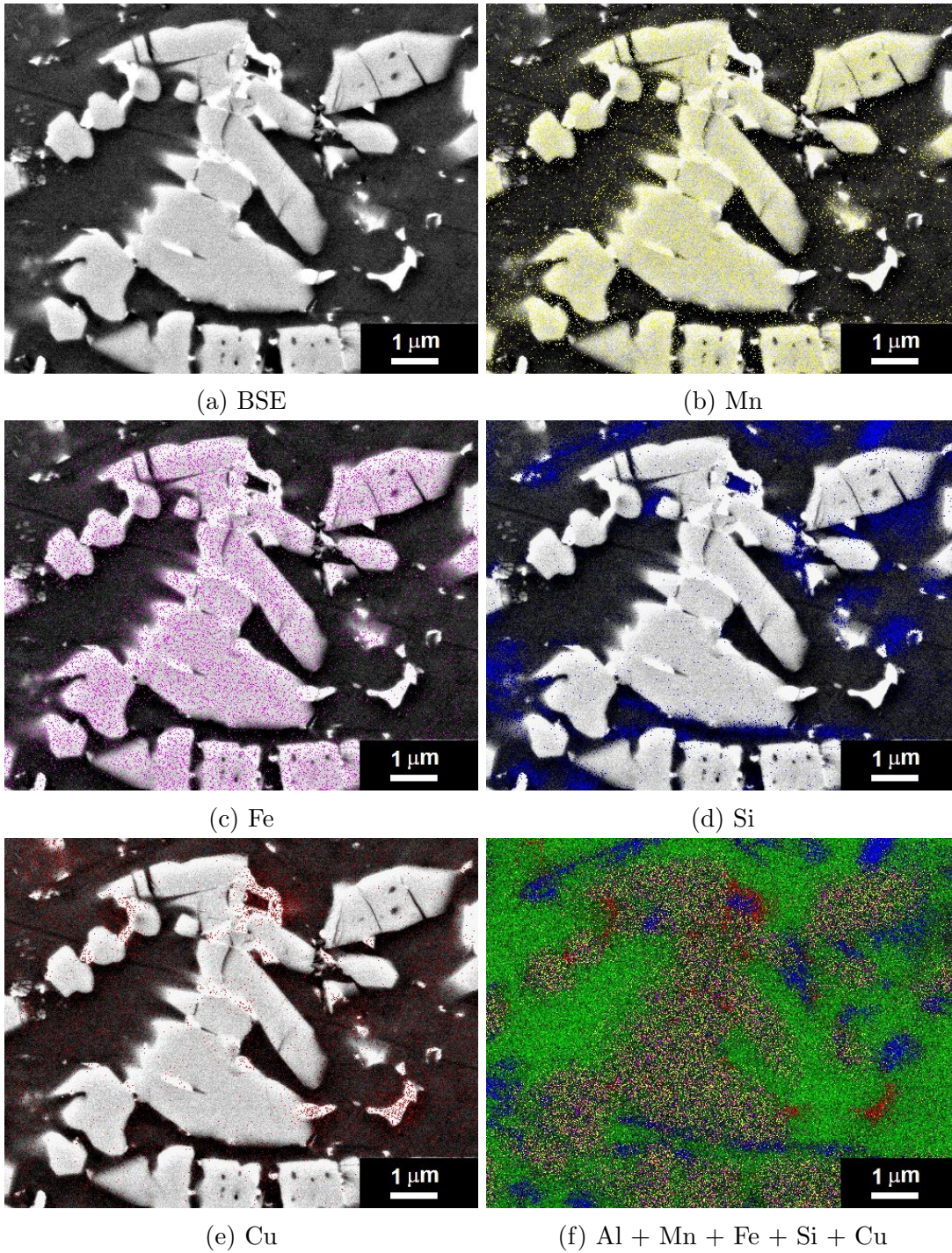


Figure 8.5: EDS maps of chemical elements in material C470 after twin-roll casting (Al – green, Mn – Blue, Fe – magenta, Si – blue, Cu – red).

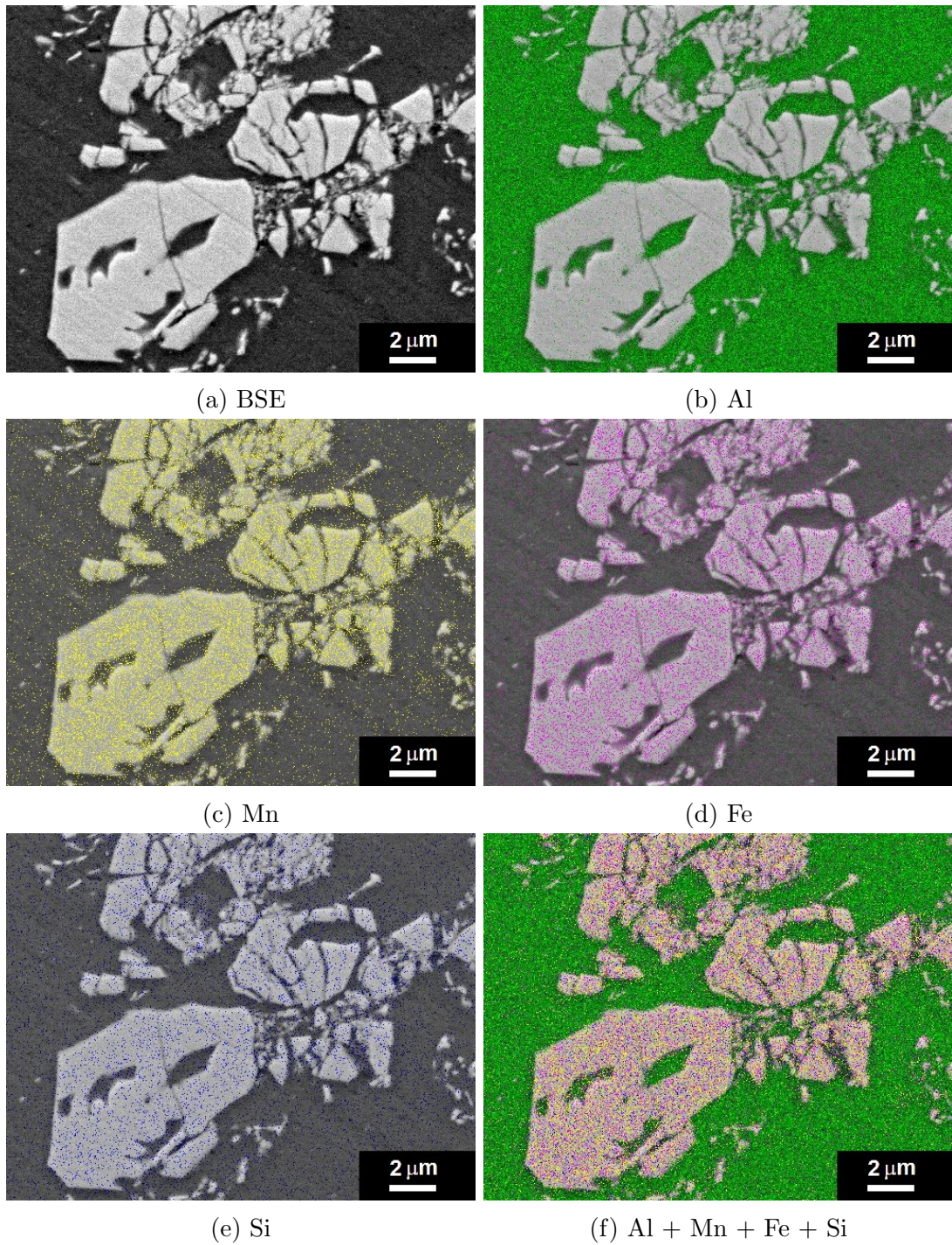


Figure 8.6: EDS maps of chemical elements in material C470 after annealing at 450 °C for 8 hours (Al – green, Mn – Blue, Fe – magenta, Si – blue).

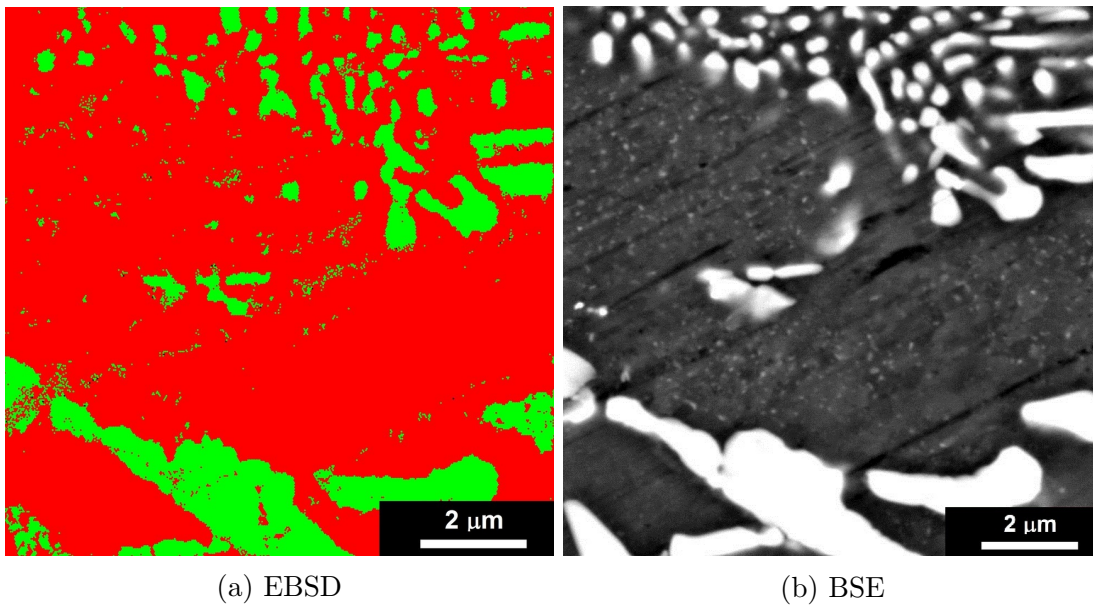


Figure 8.7: EBSD image of phases in C470 alloy annealed to 450 °C - Al (green) and cubic α -Al(Mn,Fe)Si (red) in the central segregation and corresponding BSE image.

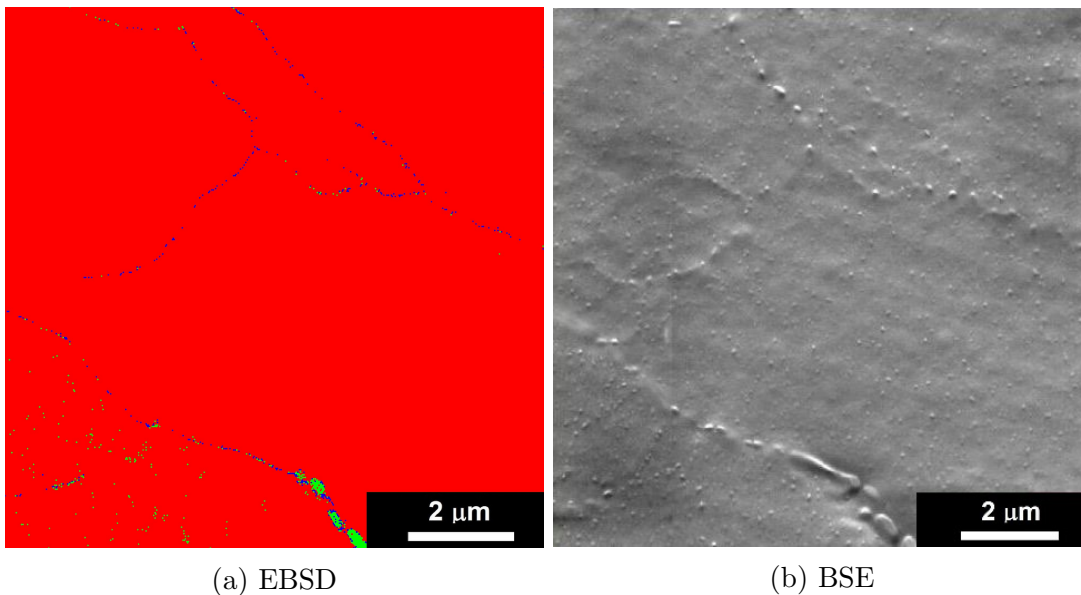


Figure 8.8: EBSD image of precipitates in C470 alloy annealed to 450 °C - Al (red), cubic α -Al(Mn,Fe)Si (green) in primary particles and in grain interior and hexagonal α -Al(Mn,Fe)Si (blue) on subgrain boundaries.

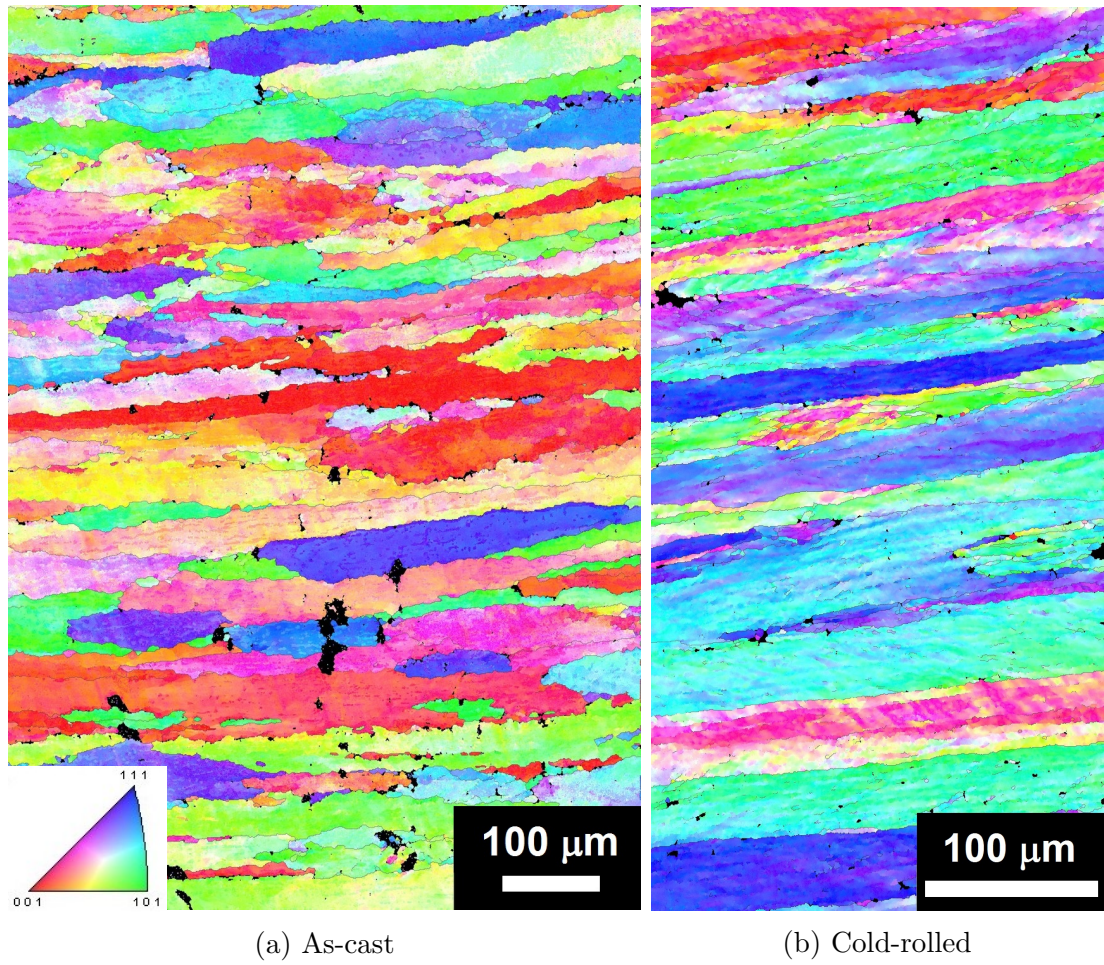


Figure 8.9: EBSD map of the grains in C470 alloy after twin-roll casting and cold rolling to 5 mm; with the color coding of orientation of Al matrix.

9. Transmission electron microscopy

9.1 Initial states

Observations in TEM revealed that twin-roll cast materials consisted of aluminium matrix with primary particles in eutectic colonies, surrounded by dislocations. The grains were subdivided into subgrains with average size of several μm . In the cold-rolled sheets, subgrains were elongated in the rolling direction due to the deformation and a high density of dislocations was observed (Figure 9.1).

9.2 Annealing

According to DTA measurements, temperatures for further investigation were chosen as 300 °C, 400 °C, 500 °C and 620 °C for as-cast sheets and 280 °C, 380 °C, 500 °C and 620 °C for the cold-rolled ones. Specimens were annealed in an air furnace to selected temperatures with heating rate 5 K/min and quenched into cold water.

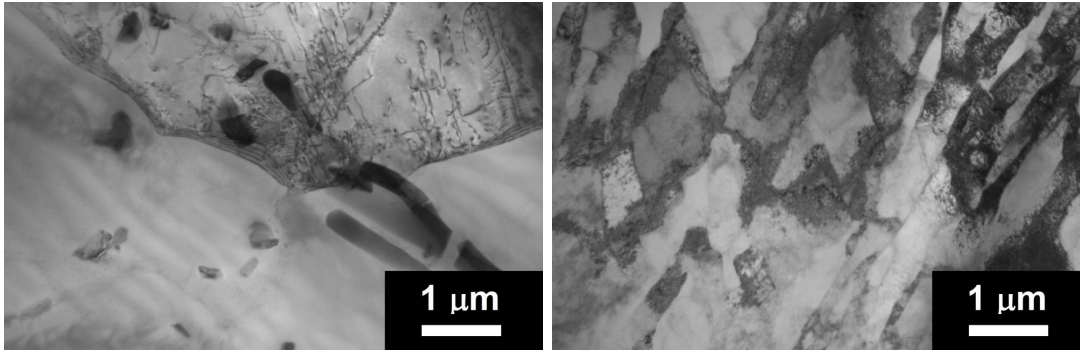
After annealing to 300 °C slight spheroidization of primary particles occurred and during further heating to 400 °C first precipitates of α -phase formed. In the Zr-free alloy C412 they were found mainly at subgrain boundaries (Figure 9.2a) while in the Zr-bearing alloy C470 precipitates formed not only on subgrain boundaries but also within the subgrains in random clusters.

Concerning the sheets cold-rolled to 1 mm, first α -phase precipitates were observed in both alloys after heating to 380 °C. However, they were rather smaller and their number density was higher in Zr alloy as opposed to the cold-rolled material without Zr (Figure 9.3).

In all alloys annealed to 500 °C high density of precipitates was present. In non-deformed sheets the precipitates not only decorated subgrain boundaries but their dense population was observed also inside the subgrains (Figure 9.2b). In cold-rolled materials new small particles with average diameter of around 30 nm precipitated next to those that nucleated at lower temperatures and coarsened during further annealing to approximately 80 nm. The size of precipitates was comparable in both alloys C412 and C470. Recrystallization already started in cold-rolled material without Zr at this temperature and in some parts of the foil small subgrains were replaced by grains with larger diameter (Figure 9.4).

Due to the annealing to 620 °C the average size of α -phase precipitates increased in all materials to ~ 150 nm, though this augmentation was more apparent in non-deformed states. The shape of the particles, which nucleated during heat treatment, depended on the deformation: in cold-rolled sheets the precipitates were mainly spherical while their shape was more complex in non-deformed materials – they often appeared as polygonal plates. Both cold-rolled alloys were fully recrystallized after annealing to this temperature.

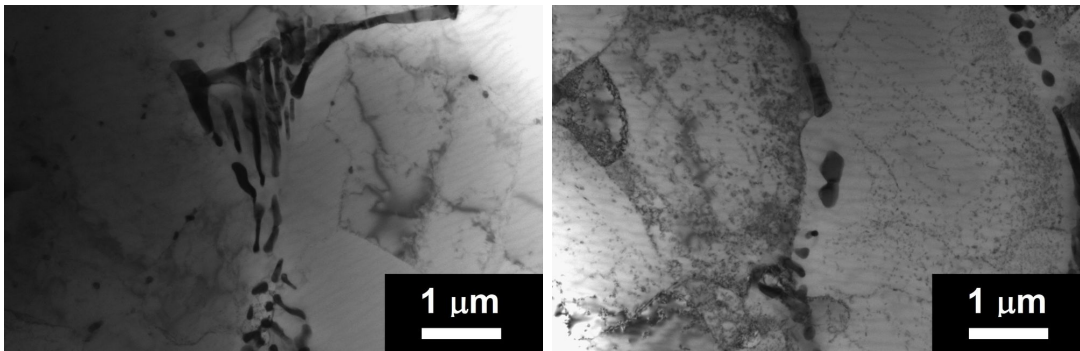
According to EDS analysis the content of manganese and silicon in all precipitates was comparable to each other and was much higher than iron content.



(a) C471, as-cast

(b) C470, cold-rolled 5 mm

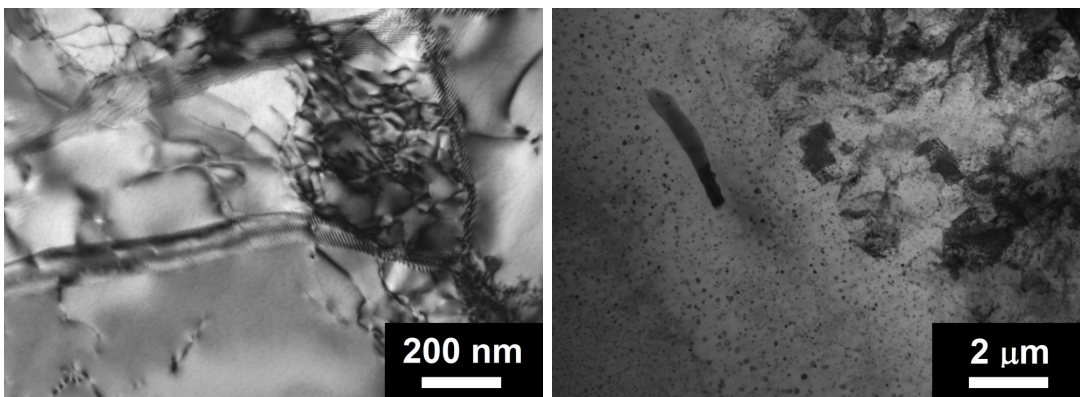
Figure 9.1: Initial microstructure of as-cast and cold-rolled alloys observed in TEM. Material C471 with primary particles and dislocation substructure (a) and C470 after cold-rolling with elongated subgrains and high dislocation density (b).



(a) 400 °C

(b) 500 °C

Figure 9.2: Microstructure of as-cast alloy C412 after annealing to 400 °C with clustered primary particles and first precipitates on subgrain boundaries (a) and high number of precipitates and PFZ near spheroidized primary particles after annealing to 500 °C (b).



(a) 280 °C

(b) 500 °C

Figure 9.3: Microstructure of alloy C412 cold-rolled to 1 mm after annealing to 280 °C with dislocation substructure and annealing to 500 °C with partially recrystallized structure (left = recrystallized, right = still deformed).

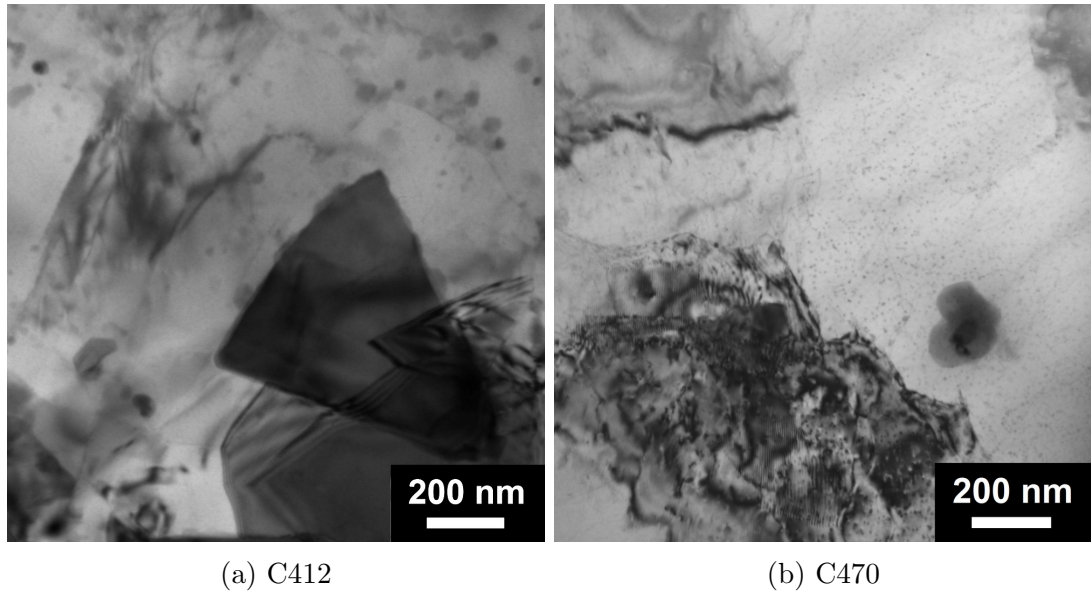


Figure 9.4: Microstructure of cold-rolled materials C412 and C470 after annealing to 380 °C with newly formed precipitates.

9.3 In-situ heating

As-cast alloy C470 with Zr was subjected to in-situ annealing in transmission electron microscope. This allowed observation of substructure recovery, precipitation, particles coarsening and dissolution on one spot in the material during the whole heating cycle. The heating scheme 50 K/50 min was applied – the sample was heated to required temperature, held 50 minutes at this temperature and afterwards the temperature was raised again by 50 K, and so on up to 550 °C. The images from in-situ heating can be found in Figure 9.5 and the video in appendix.

First precipitates of α -Al(Mn,Fe)Si phase started to form at subgrain boundaries at 300 °C, followed by particles which emerged in the interior of the grains. Their number and diameter rose up to 350 °C, where their number density started to decrease. The smaller particles dissolved back to solid solution, the others grew further. At 550 °C almost no particles were present in the matrix. No grain motion was observed.

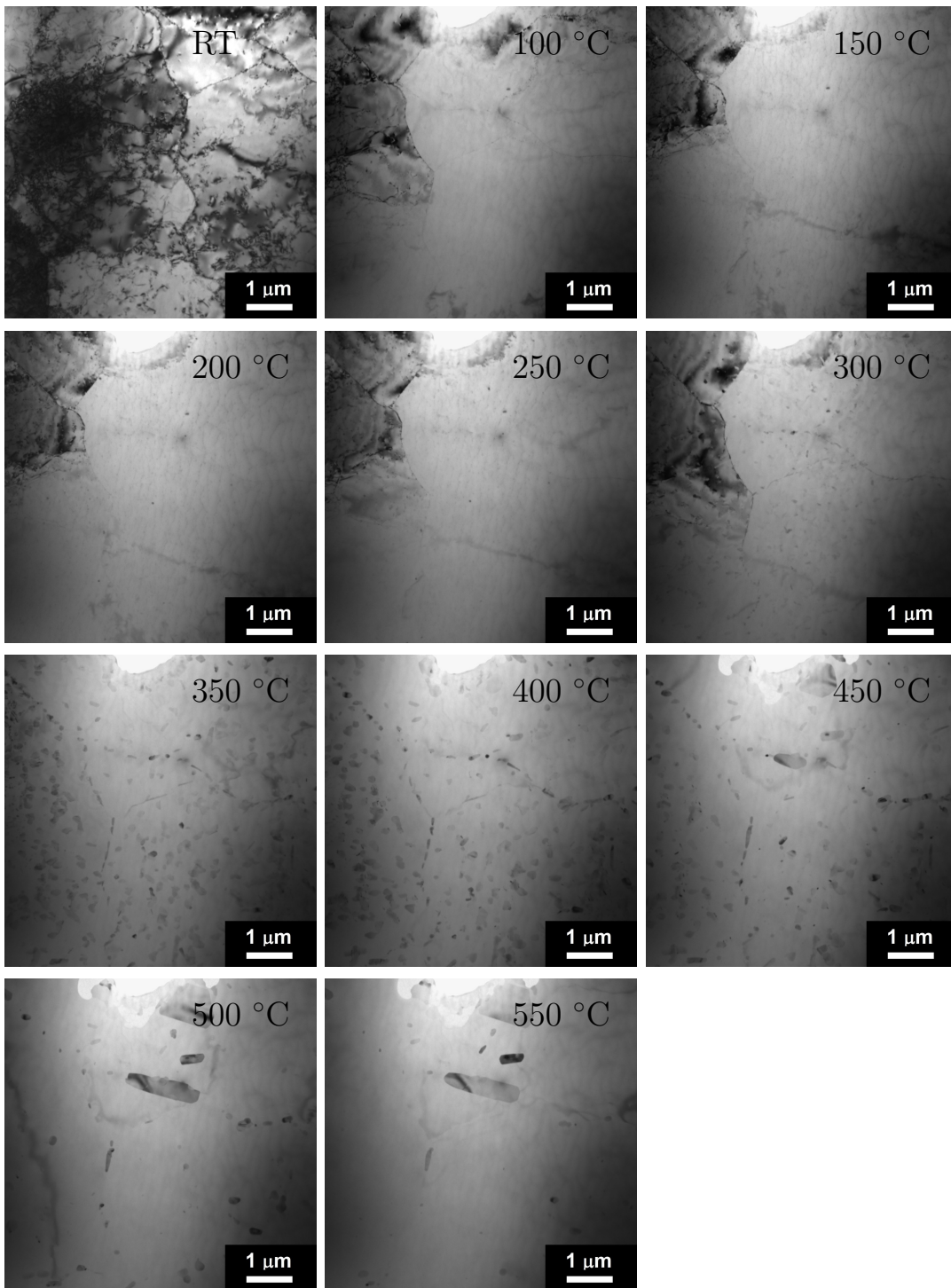


Figure 9.5: In-situ annealing in TEM of as-cast alloy C470 from room temperature to 550 °C.

10. Discussion

After casting the microstructure of all studied alloys was inhomogeneous with primary particles clustered in eutectic colonies and high contents of Mn and Si supersaturated in the (Al) solid solution. Composition of primary particles corresponded to α -Al(Mn,Fe)Si phase with silicon content higher than iron and manganese. According to EBSD mapping these phase had cubic structure with lattice parameter 1.26 nm. In material C471 Cr was also built into the α -phase to form α -Al(Mn,Fe,Cr)Si. During heat treatment further manganese incorporated into these particles which resulted in their spheroidization. As Si content was relatively high in all alloys (~ 0.6 wt.%), no $\text{Al}_6(\text{Mn,Fe})$ particles formed.

Macro-segregation of eutectic colonies was present in the center of materials with Zr (and Cr) additions – C470 and C471 and caused a slight increase of microhardness. Presence of the segregation was influenced neither by cold-rolling nor by isochronal annealing.

Some of the primary particles near the edges of the foils were ordered in the rolling direction, on the grain boundaries. This corresponded to the grain shape, which was elongated near the edges due to the rolling component of twin-roll casting. The unhomogeneity of grain structure resulted in unhomogeneous mechanical properties – the microhardness exhibited higher values at the edges of the foils where the average grain width was smaller.

Micrographs in polarized light and EBSD mapping revealed smaller grains in material without Zr and Cr additions – C412. This was caused by different casting conditions – materials with zirconium were cast at higher temperature to suppress formation of coarse Zr-containing particles. In the as-cast materials the grains near the surface were elongated in the rolling direction. Cold-rolled materials contained grains elongated in the RD in the whole volume; those near the edges were more flat than those in the center. During annealing up to 620 °C new grains formed via recrystallization. According to microhardness measurements, materials cold-rolled to 1 mm recrystallized earlier than those cold-rolled to 5 mm due to higher stored deformation energy induced into the matrix by higher extent of deformation.

Thanks to DTA and resistivity measurements phase transformations were detected at temperatures between 300 °C and 500 °C. The onset of these transformations was earlier in the cold-rolled materials. The temperature also differed for the edge and the center of the as-cast materials, where microstructure was different in regard to the macro-segregation. In the center, where most of the atoms of alloying elements were consumed in macro-segregation, the precipitation was postponed to higher temperatures, as lower amount of alloying elements was available for precipitates formation.

In the as-cast sheets the first exothermic peak in DTA occurred between 300 °C and 400 °C and was more pronounced in alloy without Zr, where the precipitates nucleated preferentially at subgrain boundaries. In the Zr-bearing alloys, some of the new particles formed also inhomogeneously in clusters within the grains.

The second stage of precipitation took place in the temperature range 400-500 °C and new precipitates nucleated in the whole volume of the material, not only at the subgrain boundaries.

Further annealing at temperatures above 550 °C led to partial dissolution of smaller precipitates and coarsening of the remaining ones.

In the as-cast material the bulk precipitation prevailed; however, cold-rolling introduced new grain boundaries into the material which caused the majority of the precipitates to nucleate at lower temperature on the grain boundaries. The most intense precipitation according to DTA occurred between 360 °C and 500 °C in the Zr-free alloy and between 390 °C and 500 °C in the Zr containing alloy, respectively. At 620 °C the remaining precipitates could be divided into two groups – coarsened particles with average diameter of around 120 nm, and smaller ones about 40 nm which precipitated at higher temperatures.

Both in resistivity and DTA spectra the detected phase transformation in alloy C412 cold-rolled to 1 mm started at lower temperatures than in materials with addition of zirconium. Observations in TEM revealed in the C412 material, that as the precipitation started earlier, lower number of precipitates nucleated and during annealing to 380 °C their diameter reached higher values than in material C470, where high density of precipitates nucleated at higher temperature. However, the area under the first peak in resistivity spectra was equivalent for all alloys cold-rolled to 1 mm and after annealing to 500 °C, both the size and number density of the precipitates were comparable in all materials.

After annealing to 500 °C, TEM revealed partially recrystallized microstructure in alloy C412 cold-rolled to 1 mm. According to microhardness measurements, the main drop of HV in this material was finished before 500 °C. However, the heating rate and also the heating scheme were different during microhardness measurement and for TEM observations. As the heating rate was higher for TEM, the time at lower temperatures was not sufficient for the microstructure to undergo recrystallization in the whole volume. Moreover, for TEM observations samples were just heated to the required temperature, although for microhardness all samples were heated for 20 minutes at the given temperature.

Due to the low solubility of iron in aluminium [1], most of Fe atoms were incorporated in the primary particles after casting. Solubilities of silicon and manganese are much higher and relatively significant amounts of Si and Mn atoms were dissolved in the aluminium matrix. Thus during decomposition of solid solution at elevated temperatures, precipitates were composed mainly of Mn and Si and contain nearly no Fe.

According to EBSD analysis, the precipitates in the grain volume were cubic α -phase and on the subgrain boundaries hexagonal α -phase. However, the size of the precipitates was in the same magnitude with the available step of EBSD measurement and the precipitates were hard to detect.

The addition of zirconium did not influence the position of the precipitation peaks as the resistivity and DTA measurements reflect only precipitation of major phases with Mn, Fe and Si. However, it affected the evolution of microhardness during annealing. The alloy with Zr exhibited higher values of microhardness and recrystallized at higher temperature. This demonstrates the positive influence of zirconium on recrystallization resistance of aluminium alloys.

In the as-cast foils the microhardness started to increase from ~400 °C when also the precipitates started to form and grow. The peak HV was reached after 500 °C, when the precipitates density was the highest. Further with the particles dissolution microhardness dropped again.

Part III
Zirconium addition

11. Two-step annealing

The following part of the work was devoted to the search of ideal conditions for Al_3Zr particles formation.

Several authors reported, that the best results for precipitation of coherent Al_3Zr precipitates were achieved after two-step annealing at 250 °C and 450 °C with slow heating rate (e.g. [89]). Thus two-step annealing was chosen for the first part of investigation.

For examination in TEM two-step annealing in DSC was chosen. 3 mm discs were heated with heating rate 0.5 K/min to 250 °C, held at this temperature for 0 or 12 hours, subsequently heated to 450 °C with the same heating rate, where they remained for 0, 1, 2, 4 or 8 hours. Afterwards they were cooled with rate 0.5 K/min (Figure 11.1).

After casting materials contained primary particles of $\alpha\text{-Al}(\text{Mn,Fe})\text{Si}$ in eutectic colonies and some dislocations within the grains. Huge number of α -phase precipitates formed during two step annealing, some of them decorated grain boundaries, others were observed in the bulk (Figure 11.2). They were much smaller in size than primary particles. In more detailed view, tiny precipitates of Al_3Zr phase were found after all annealing steps in as-cast materials C470 and C471 with zirconium addition. However, their distribution was not uniform, places without these precipitates were found within the material (Figure 11.3).

After cold-rolling to 5 mm and two-step annealing at 250 °C and 450 °C with heating rate 0.5 K/min, the density of observed Al_3Zr particles was lower than in the non-deformed sheets.

High density of Al_3Zr precipitates was also observed in the step, where the holding at 250 °C was 0 hours. The distribution of Al_3Zr particles was comparable regardless time at 250 °C (see Figure 11.4) and so one-step annealing at only 450 °C was applied for further study of microstructure and mechanical properties.

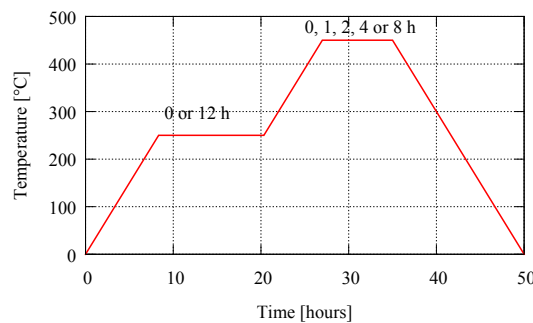
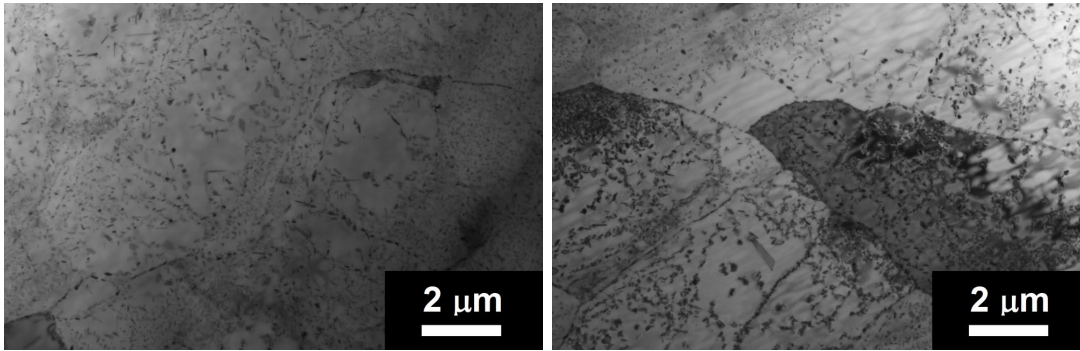


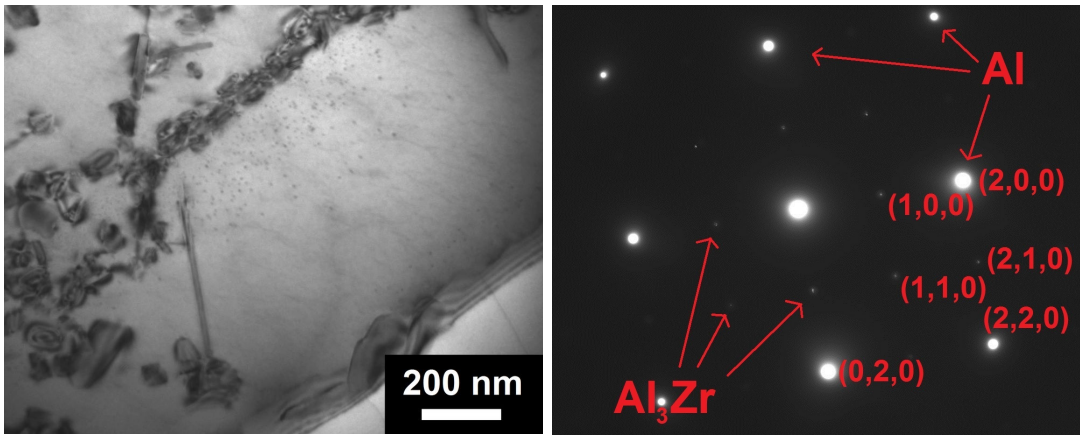
Figure 11.1: Heating scheme for two-step annealing at 250 °C and 450 °C in DSC.



(a) 12 h/250 °C and 2 h/450 °C

(b) 12 h/250 °C and 8 h/450 °C

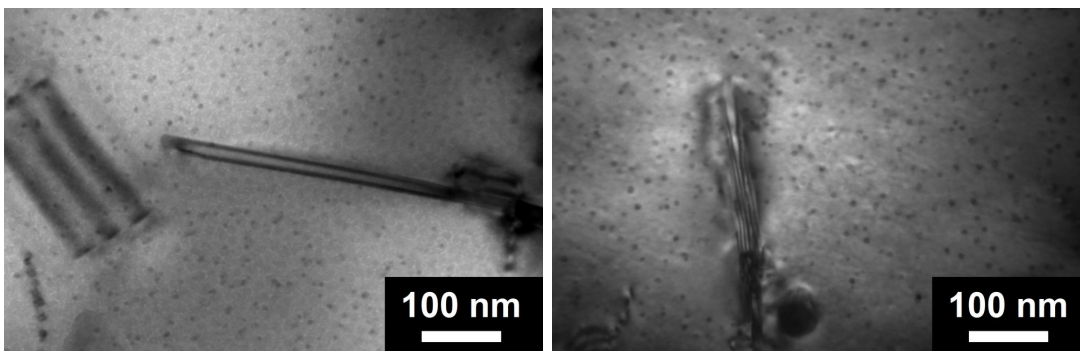
Figure 11.2: Microstructure of C471 material after two-step annealing at 250 °C and 450 °C with heating rate 0.5 K/min: high number of precipitates, some of them copy subgrain boundaries.



(a) BF

(b) SAED

Figure 11.3: Microstructure of C471 material after two-step annealing 12 h/250 °C and 0 h/450 °C with heating rate 0.5 K/min, unhomogeneous distribution of Al_3Zr and selected area electron diffraction with additional diffraction spots from Al_3Zr with structure L1_2 , which are forbidden for Al.



(a) 12 h/250 °C and 8 h/450 °C

(b) 8 h/450 °C

Figure 11.4: Microstructure of C471 material after annealing at 8 h/450 °C with and without annealing step at 250 °C.

12. One-step annealing

In further step materials were subjected to annealing to 450 °C in an air furnace with heating rate 0.5 K/min and holding at 450 °C, followed by water quenching. The mechanical properties and microstructure were studied with regard to the time of holding at 450 °C – from 0 to 16 hours.

12.1 Mechanical properties

The evolution of Vickers microhardness during annealing at 450 °C is displayed in Figure 12.1a. Moreover, the values of microhardness of the as-cast state and cold-rolled state before annealing are plotted. As for the initial states, the values of HV were similar for the material with and without Zr around 50 HV0.1. Thanks to cold-rolling to 1 mm the HV reached 80 HV0.1. After heating to 450 °C, microhardness of the as-cast materials increased; this rise was more pronounced in the materials containing zirconium – approximately 30 %. During holding at 450 °C the microhardness decreased moderately, maintaining higher values for the Zr containing materials.

The microhardness drop in sheets cold-rolled to 5 mm was fluent in all materials, maintaining the same slope of the decrease up to 16 hours of annealing. The HV values were by ~10 % lower in C412 alloy.

Concerning sheets cold-rolled to 1 mm, microhardness values decreased during annealing to 450 °C and this trend continued also during holding at 450 °C. Most of this drop was completed after 2 hours of holding at 450 °C in material C412 and after 8 hours for C470 and C471. Final values of microhardness of all alloys were comparable with the HV of the as-cast Zr-free alloy after 16 hours at 450 °C.

Concerning the tensile tests at room temperature (Figure 12.1b), annealing for 8 hours at 450 °C caused reduction in ductility by ~30 % and slight increase in yield strength in Zr-containing alloys. In C412 the changes were less pronounced.

12.2 Microstructure

The evolution of grain structure was monitored by light optical microscopy. Holding at 450 °C for 16 hours did not impact the grain size of the as-cast sheets substantially.

Owing to cold-rolling, 1 mm thick sheets contained narrow grains elongated in rolling direction. Thickness of the grains was higher in the center of the sheets. After heating to 450 °C, first recrystallized grains were observed in the Zr-free material C412. After 2 hours of holding at the temperature this material was fully recrystallized. Though, the rolling direction was still apparent. The structure was very inhomogeneous, ranging from several tiny equiaxed grains with the size of 10 μm in the bulk to the grains at the surface with length of several mm.

The situation was different in alloys with zirconium addition (Figure 12.2). If just heated up to 450 °C, the structure remained deformed; partial recrystallization was apparent after holding for 2 hours at 450 °C. Recrystallization started probably near the surface, as the deformed structure was observed only in the

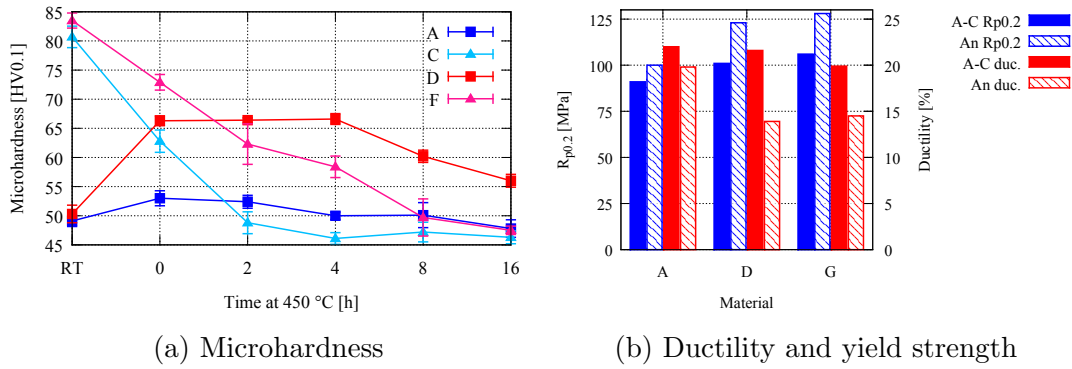


Figure 12.1: (a) The evolution of Vickers microhardness during annealing at 450 °C for materials C412 and C470, as-cast and cold-rolled states. (b) Ductility (duc.) and yield strength (Rp0.2) of as-cast alloys before (A-C) and after (An) annealing for 8 hours at 450 °C.

central part of the sheet. The recrystallization was completed after 8 hours of annealing. The grain-shape distribution was similar to the Zr-free alloy; however, the average grain size was lower in Zr containing materials.

High number of α -Al(Mn,Fe)Si particles formed in the course of annealing. During holding at 450 °C their average diameter slightly increased, volume fraction decreased and primary particles spheroidized. Secondary particles, which formed during annealing to 450 °C, were also apparent on micrographs from LOM and SEM, see Figure 12.3.

In cold-rolled materials the α -Al(Mn,Fe)Si precipitates were homogeneously distributed inside the material.

Regarding precipitation of Al_3Zr particles in the Zr containing alloy, first precipitates were observed in the alloy just after heating up to 450 °C. However, their number density was very low. It increased significantly during holding for 2 hours at 450 °C (Figure 12.4). They were identified as metastable coherent phase with cubic $L1_2$ structure with diameter around of 5 nm. Their distribution was not uniform within the material and their size only slightly rised during further annealing.

No Al_3Zr precipitates were detected by TEM in the material which was cold-rolled to 1 mm and subsequently annealed to 450 °C.

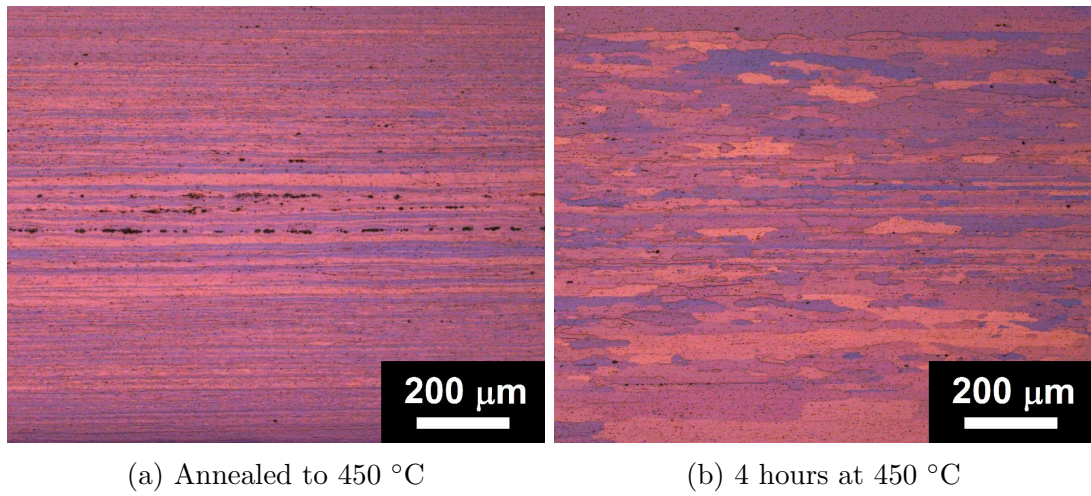


Figure 12.2: Grain structure of material C470 cold-rolled to 1 mm after annealing to 450 °C with heating rate 0.5 K/min and holding for 4 hours at this temperature.

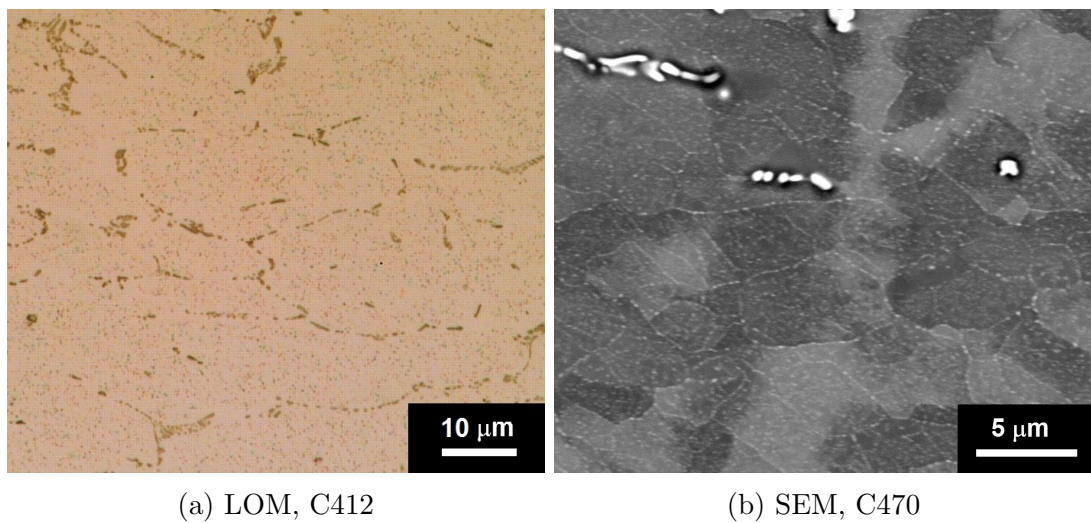
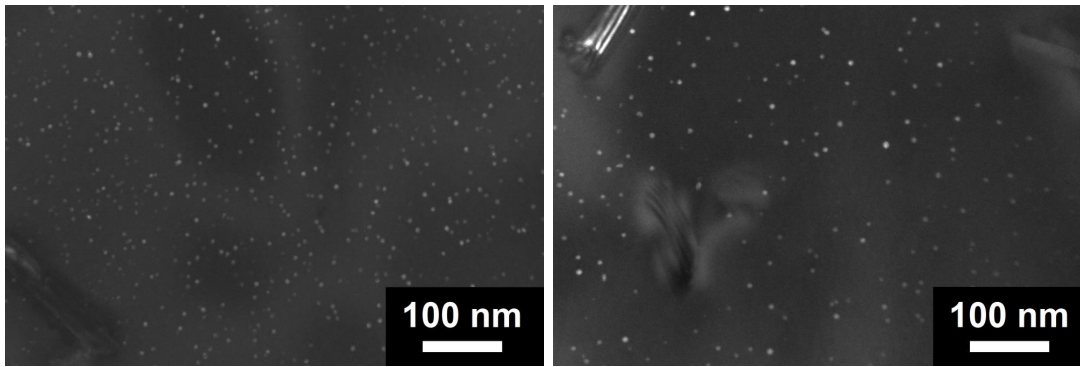


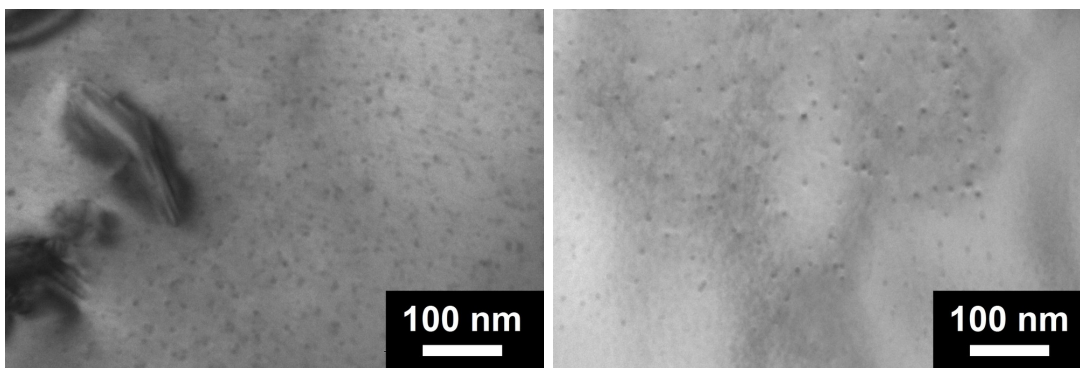
Figure 12.3: (a) Light optical micrograph of particles of α -Al(Mn,Fe)Si phase, which nucleated during annealing to 450 °C in material C412, inbetween clusters of larger primary particles. (b) SEM micrograph in BSE of particles of α -Al(Mn,Fe)Si phase in material C470, copying subgrain boundaries and in the grain interior, and several primary particles in chains.



(a) 2 hours

(b) 8 hours

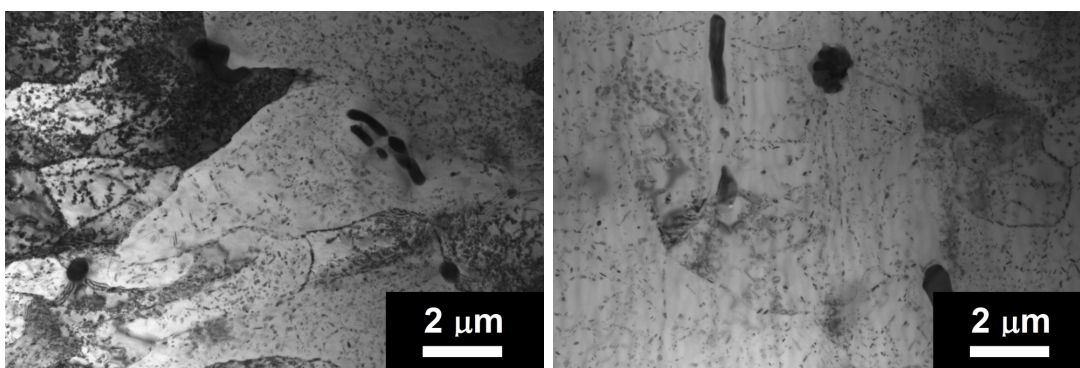
Figure 12.4: Dark field TEM image of Al_3Zr precipitates in C470 alloy after annealing to $450\text{ }^\circ\text{C}$ with heating rate 0.5 K/min and holding for 2 and 8 hours at this temperature.



(a) DSC

(b) Furnace

Figure 12.5: As-cast alloy C470 annealed with heating rate 0.5 K/min to $450\text{ }^\circ\text{C}$, held at this temperature for 8 hours (a) in DSC with cooling 0.5 K/min and (b) in an air furnace followed by water quenching – distribution of Al_3Zr precipitates.



(a) DSC

(b) Furnace

Figure 12.6: As-cast alloy C470 annealed with heating rate 0.5 K/min to $450\text{ }^\circ\text{C}$, held at this temperature for 8 hours (a) in DSC with cooling 0.5 K/min and (b) in an air furnace followed by water quenching – distribution of $\alpha\text{-Al(Mn,Fe)Si}$ phase particles.

13. Discussion

All alloys were subjected to annealing at 250 °C and 450 °C in order to find out suitable conditions for precipitation of Al₃Zr particles in the Zr-containing ones. It was shown that coherent precipitates of Al₃Zr phase were present in as-cast materials with zirconium even after 12 h/250 °C + 0 h/450 °C or 0 h/250 °C + 8 h/450 °C annealing steps. Annealing at 250 °C was thus shown unnecessary for their formation and only annealing at 450 °C was studied further. Volume fraction of Al₃Zr precipitates increased with the annealing time. However, their distribution remained unhomogeneous.

Distribution of both Al₃Zr and α -Al(Mn,Fe)Si precipitates was comparable regardless the way of annealing – either in DSC with slow cooling rate or in an air furnace with water quenching from 450 °C (Figures 12.5 and 12.6).

The addition of zirconium positively influenced mechanical properties of the studied alloys. This was monitored by the evolution of Vickers microhardness, which was higher for materials with Zr addition.

In the as-cast state zirconium atoms were dissolved in the solid solution of aluminium and HV values were nearly the same for all alloys. After heat treatment HV moderately rised due to the precipitation hardening from α -phase precipitates. However, thanks to the nucleation of Al₃Z particles, which strengthen the matrix, the increase was much higher in the Zr-containing alloys. During holding at 450 °C the slight decrease of HV was caused by depletion of the solid solution from Mn and Si atoms. For alloys with Zr this decrease was compensated by further formation of Al₃Z precipitates at short annealing times - up to 4 hours at 450 °C. Owing to the high number of Al₃Z, the final value of HV after long-time exposure to 450 °C remained higher than in the Zr-free alloy.

Cold-rolling resulted in formation of elongated grains in all materials and to deformation hardening with significant increase of HV. The deformed substructure recovered and new grains formed during recrystallization; this process was considerably affected by the presence of Zr. While the first recrystallization nuclei appeared in the Zr-free alloy even during heating up to 450 °C and nearly full recrystallization occurred after 2 hours at 450 °C, materials with Zr fully recrystallized after longer holding at 450 °C – 8 hours.

Such shift in recrystallization resistance could be attributed to Zener pinning of Al₃Z precipitates. However, no such particles were detected by TEM in the sheets cold-rolled to 1 mm. In foils of thickness of 5 mm their number density was lower than in the 8 mm sheets. This is in contradiction with Nes and Slevolden [86] who claim that deformation should facilitate nucleation of Al₃Z as dislocations can serve as nucleation sites and, in addition, accelerate diffusion. It is therefore probable that the Al₃Z precipitates in the cold-rolled material were too small to be detected by transmission electron microscopy.

The impact of other phases on microhardness in the cold-rolled materials was compensated by recrystallization.

Part IV

Equal channel angular pressing

14. Equal channel angular pressing

The last part of the work was devoted to study of severe plastic deformation by ECAP and thermal stability of the deformed alloys during subsequent annealing.

14.1 Processing

All three studied materials were subjected to severe plastic deformation by equal channel angular pressing at room temperature. Details of this procedure are given in section 2.2 on page 45. Prior to ECAP materials were annealed to 450 °C with heating rate 0.5 K/min and held at 450 °C for 8 hours in order to precipitate high dispersion of Al₃Zr particles. Two types of materials were studied: ECAPed just after twin-roll casting (further referred as A, D and G) and heat treated at 450 °C before ECAP (AZ, DZ and GZ, respectively).

Pre-annealed materials AZ, DZ and GZ were processed by 1, 2, 4 and 8 passes. The non-annealed A, D and G were capable of maximum 4 passes; with further processing cracks occurred.

14.2 Mechanical properties

After ECAP processing Vickers microhardness and tensile properties were performed on all materials. Dependences of the mechanical properties on number of ECAP passes are depicted in Figure 14.1.

Concerning tensile tests, increasing number of ECAP passes shifted the stress vs. strain curves to higher stresses. Simultaneously, a drop in formability occurred. The main change in deformation behaviour occurred already during the first ECAP pass. Further ECAP passes caused only moderate strength increase and did not influence significantly the ductility.

Differences in behaviour of non-annealed and annealed materials were also observed. Higher strength of pre-annealed Zr-containing materials (DZ and GZ) resulted from precipitation hardening especially by Al₃Zr particles. However, an opposite effect was observed already after the first ECAP pass. Strength increase caused by ECAP was significantly higher in non-annealed materials so that the non-annealed materials became stronger.

ECAP resulted also in significant increase of Vickers microhardness, which was most pronounced after the first ECAP pass. In non-annealed materials microhardness values shifted from initial 55 HV0.1 to ~85 HV0.1 after the first pass and further rose to ~100 HV0.1 up to the fourth pass. In the pre-annealed materials the increase was milder, the first pass caused shift of microhardness by 15-20 HV0.1. The evolution of microhardness exhibited similar trend for all materials. However, the absolute values were slightly lower for material without Zr (A and AZ). Moreover, microhardness of pre-annealed materials reached lower values after ECAP than microhardness of the non-annealed ones.

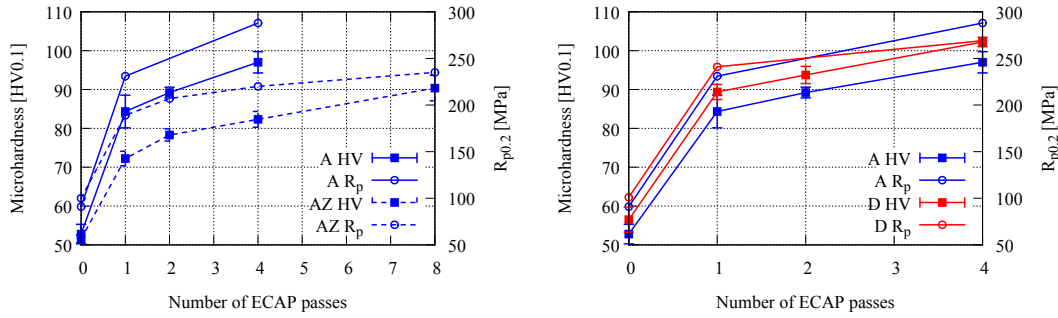


Figure 14.1: Values of Vickers microhardness and yield strength as a function of number of ECAP passes for the "A" material without zirconium, both non-annealed (A) and pre-annealed (AZ) prior to ECAP; and "D" material with zirconium addition.

Both microhardness and yield strength dependences on number of ECAP passes were qualitatively very similar and documented tight interconnection between both mechanical characteristics.

14.3 Microstructure

The initial structure with grain size in order of $100 \mu\text{m}$ was gradually destroyed during ECAP. After the first pass elongation of grains in pressing direction was apparent (Figure 14.2). Near the edges of the foil the grain length reached mm, in the central part hundreds of μm in materials with Zr; grains were shorter in Zr-free alloy. EBSD measurements revealed presence of numerous low angle grain boundaries within the elongated grains (Figure 14.4). Moreover, bands of recrystallized grains with size in order of μm occurred within the deformed matrix in the pre-annealed material with Zr. Second ECAP pass led to decrease of average subgrain size; nevertheless, the grain elongation remained apparent.

Orientation map of sample after four ECAP passes was completely different (see Figure 14.4). The mean grain size dropped to approximately $0.4 \mu\text{m}$ and the shape of the sub-micrometric grains was quite equiaxed. However, the microstructure was not fully uniform; numerous regions of the size $\sim 5 \mu\text{m}$ consisting of subgrains were still present. Structures of non-annealed and annealed materials were similar, only the grain size was slightly lower in the non-annealed ones (Figure 14.5). It was also lower for material without Zr. Further processing caused decrease of the grain size.

Finally, maps of samples after eight passes showed a mixture of regions with very small equiaxed grains and regions with elongated grains of the size over $1 \mu\text{m}$. Low angle grain boundaries were detected especially in the elongated grains, subdividing them into subgrains.

The fraction of high angle grain boundaries increased with the imposed strain by deformation. After one ECAP pass the HAGB fraction was ~ 0.3 , ~ 0.4 after two passes and ~ 0.7 after four and eight passes.

TEM micrographs for material with Zr after different number of ECAP passes are shown in Figure 14.3. Figures document severely deformed microstructure

with high density of dislocations after first ECAP pass. Only a very limited number of newly formed grains of the sub-micrometer size were observed. No significant differences were observed between particular alloys.

After two ECAP passes, both regions with high dislocation density and some newly formed grains, especially in the pre-annealed materials, were present. The replacement of severely deformed regions by ultrafine-grained structure proceeded during further ECAP passes. After four passes the grains and subgrains were well defined and dislocation density was much lower. The microstructure development seemed to be faster in the pre-annealed materials. Finally, the microstructure after eight ECAP passes consisted mostly of ultrafine grains with the grain size deeply below $1\ \mu\text{m}$. However, it was not fully recrystallized. The main difference between materials annealed and non-annealed prior to ECAP was the presence of second-phase particles in the aluminium matrix after ECAP in pre-annealed alloys and much higher dislocation density in the non-annealed materials.

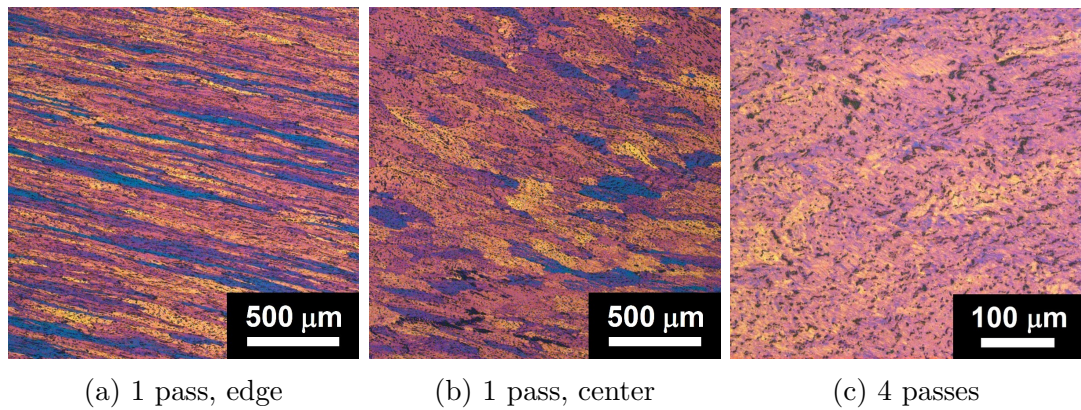


Figure 14.2: LOM micrograph of material DZ after one ECAP pass with elongated grains – near the edge of the foil and in the central part and after four passes.

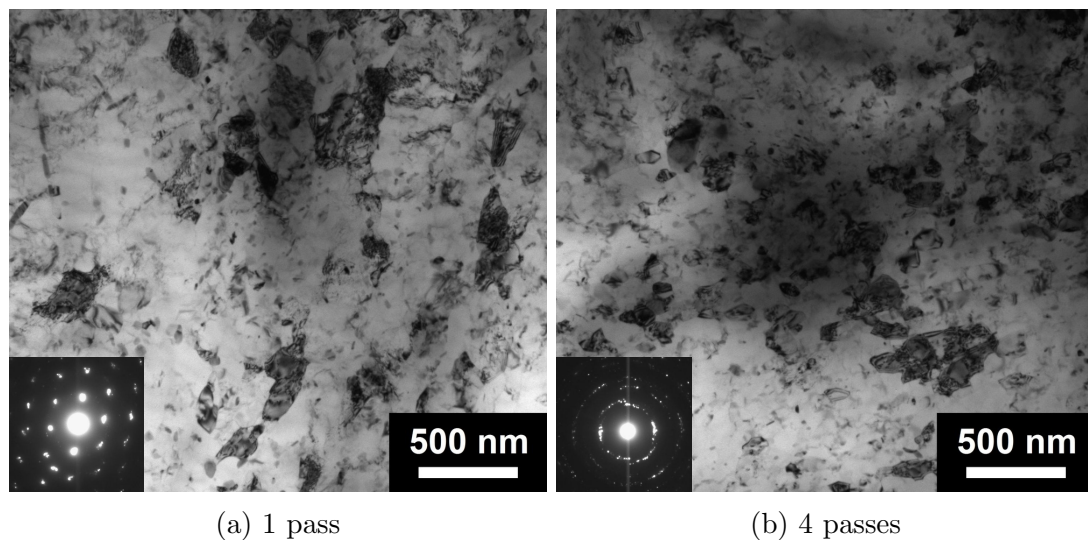


Figure 14.3: TEM micrograph of pre-annealed material DZ after one and four ECAP passes.

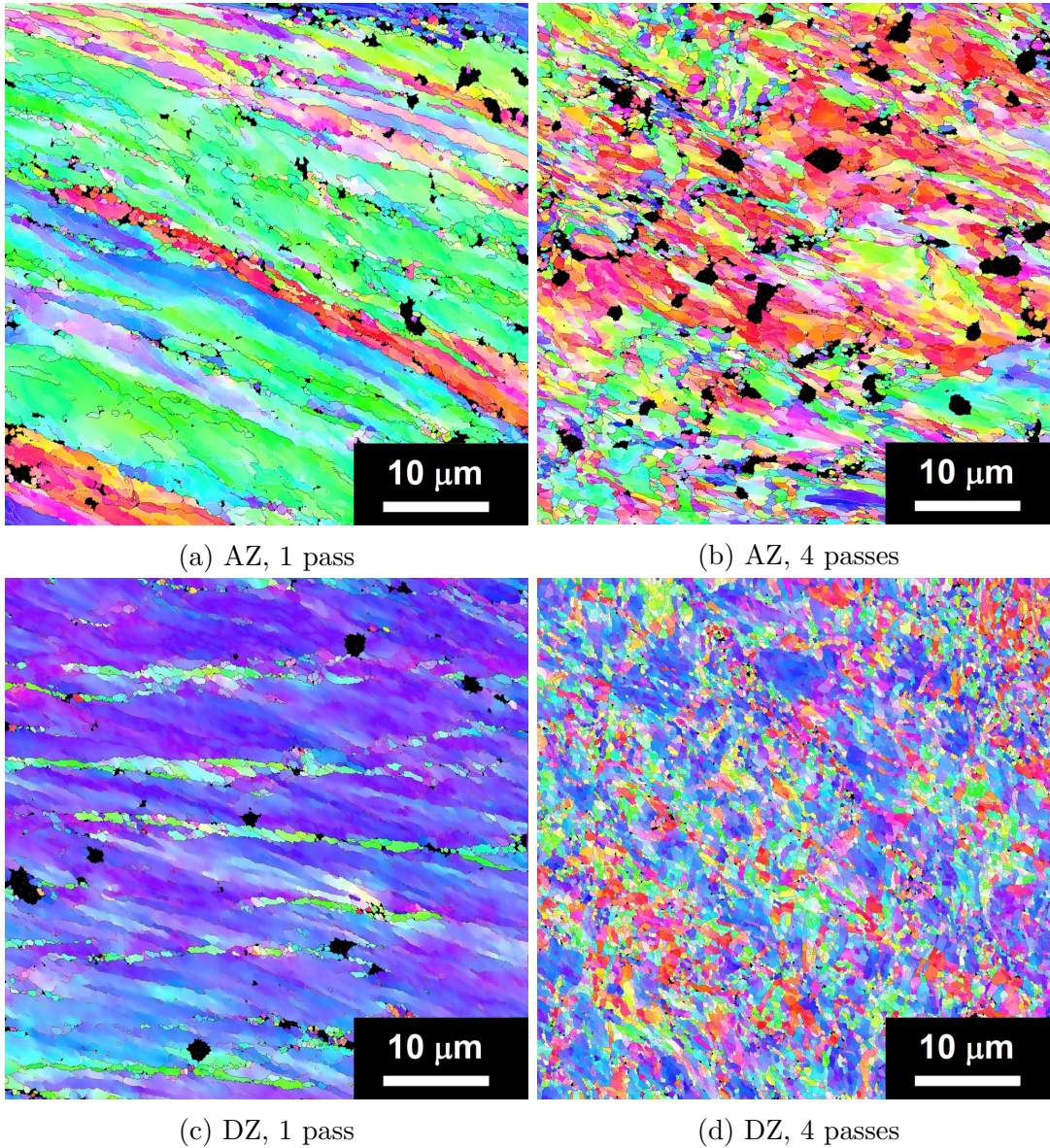


Figure 14.4: EBSD maps of materials AZ and DZ after one ECAP pass with deformed matrix and new recrystallized grains and four ECAP passes with un-homogeneously deformed matrix and grains with sub-micrometric size.

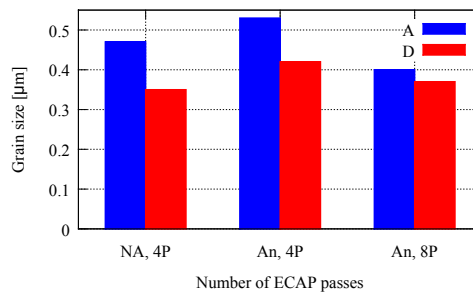


Figure 14.5: The average grain size measured by EBSD software [125] of alloys C412 and C470 after four and eight ECAP passes; for materials non-annealed (NA) and pre-annealed (An) prior to ECAP.

15. Isochronal annealing

After processing by ECAP, materials were subjected to heat treatment at elevated temperatures to study thermal stability of the microstructure and the course of second-phase particles precipitation. Firstly, isochronal annealing with step 50 K/50 min was applied and the induced changes were monitored by Vickers microhardness, electrical resistivity, light optical microscopy and transmission electron microscopy - conventional and in-situ heating.

15.1 Vickers microhardness

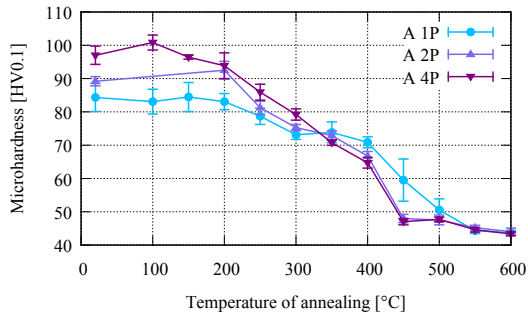
Values of Vickers microhardness after ECAP and during subsequent isochronal annealing 50 K/50 min are depicted in Figure 15.1. Deformation induced by ECAP caused significant increase of HV. Initial microhardness after ECAP was higher by approximately 10 % in the non-annealed materials as compared to the pre-annealed ones. Addition of Zr into the alloys increased HV values not only in the initial states after ECAP but during the whole annealing cycle.

Indistinctive increase of microhardness below 150 °C was observed in alloys A, D and G, which was followed by a two-stage drop of HV. Only the two-stage decrease of HV was recognized in the pre-annealed materials. At lower annealing temperatures, the HV values decreased only moderately with increasing annealing temperature; nevertheless, a significant reduction of microhardness was achieved during this stage. This stage of the microhardness drop was more distinctive in the non-annealed materials and the magnitude of the drop increased with the number of ECAP passes.

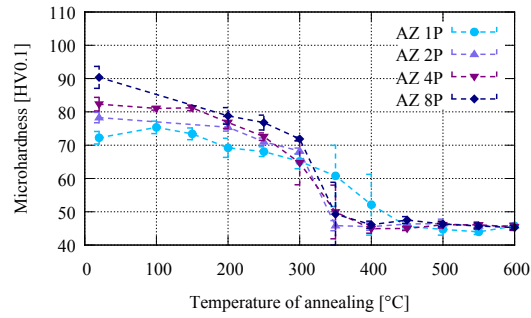
During the second stage, a steep drop of microhardness associated with full recrystallization was observed in all materials. The onset of this stage depended on number of ECAP passes and on presence of Zr. While the increasing number of ECAP passes displaced the onset of the recrystallization stage to lower temperatures, addition of Zr shifted it to considerably higher temperatures. The lowest temperature of the onset of recrystallization stage (~ 300 °C) was found in the material AZ after two, four and eight ECAP passes, materials DZ and GZ after eight passes followed at 350 °C. Concerning the main HV drop in materials after one ECAP pass, the start was similar to the materials ECAPed by more passes (~ 400 °C), however the decrease was more fluent. Figure 15.2b describes the temperature between the onset of the main HV drop and the end this decrease. At 600 °C the microhardness of all studied alloys was comparable and reached values 45-50 HV0.1.

15.2 Grain structure

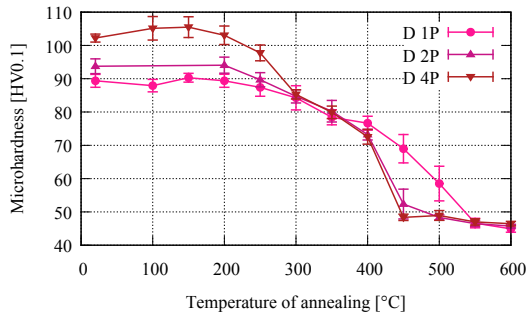
Light optical microscopy confirmed that after annealing to the temperature above the main HV drop (mainly 450 °C) the microstructure was fully recrystallized with large grains. In the materials subjected to one ECAP pass the initial elongation of the grains in rolling direction (direction of ECAP pressing) was still apparent. However the grains were more equiaxed as compared to the state just



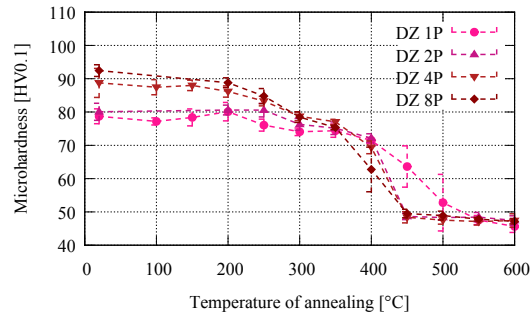
(a) C412, non-annealed



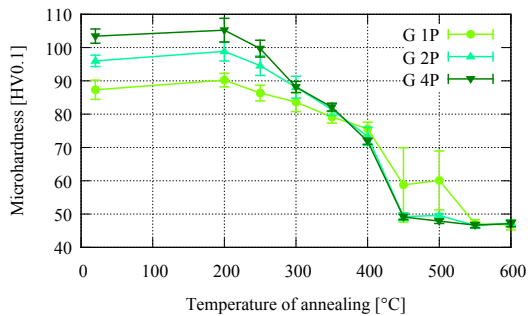
(b) C412, pre-annealed



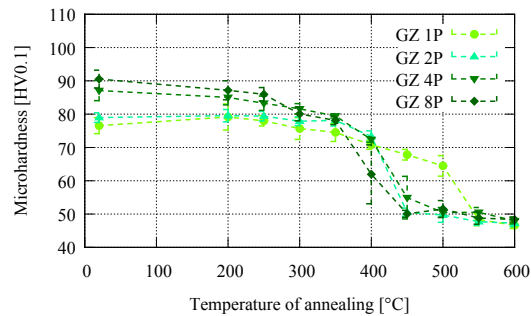
(c) C470, non-annealed



(d) C470, pre-annealed



(e) C471, non-annealed



(f) C471, pre-annealed

Figure 15.1: The evolution of Vickers microhardness during isochronal annealing 50 K/50 min for all three materials after 4 ECAP passes. Materials non-annealed prior to ECAP (A, D and G) and pre-annealed ones (AZ, DZ and GZ).

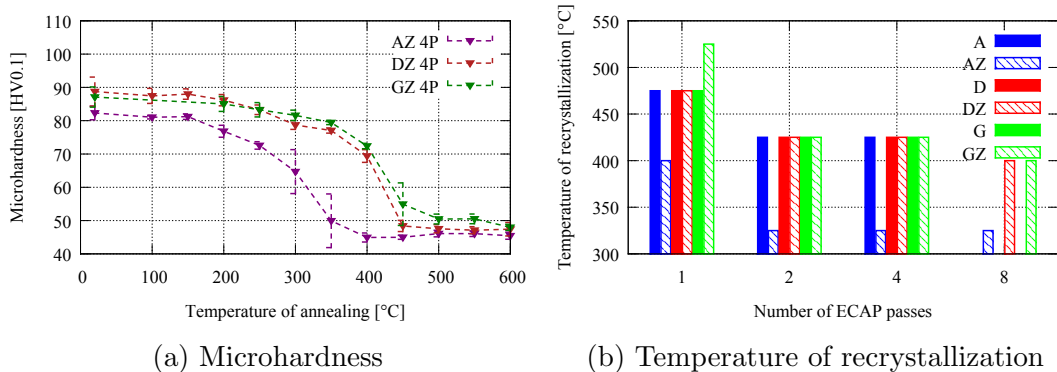


Figure 15.2: (a) The evolution of Vickers microhardness during isochronal annealing 50 K/50 min for pre-annealed materials after four ECAP passes. (b) The temperature of recrystallization during isochronal annealing 50 K/50 min after ECAP – temperature between the start and end point of the main microhardness drop.

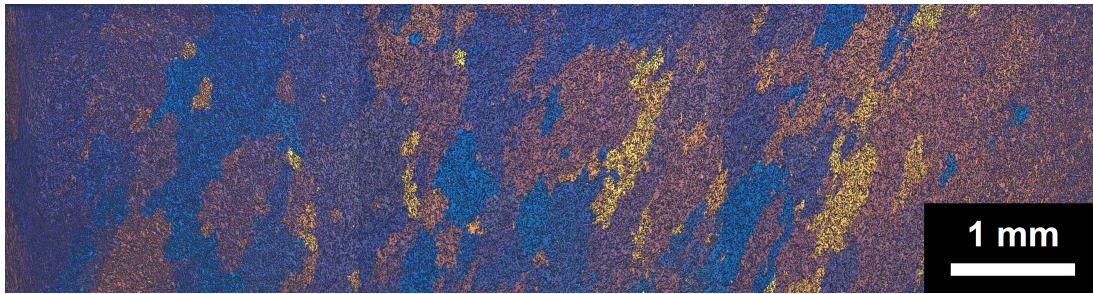
after ECAP. While the grain size was lower in the Zr-free material after casting, the recrystallized grain size after annealing up to 450 °C was much higher in the pre-annealed material without zirconium.

Concerning the materials after four ECAP passes, the main decrease of HV occurred between the temperatures of 400 °C and 450 °C for materials A, D, G and DZ, DZ. At 400 °C first recrystallized grains were observed in the central part of the billet in the vicinity of large primary particles. After further annealing to 450 °C the materials were fully recrystallized with grain size in order of 100 μm (Figure 15.3b). Further annealing to 600 °C led only to subtle grain coarsening. However, in the material AZ the drop of microhardness was observed at annealing temperatures by 100 °C lower. After annealing up to 300 °C the material was only partially recrystallized, while annealing to 350 °C resulted in almost full recrystallization. The average size of the recrystallized grains was much larger than in other materials, the diameter of the largest grains approached 1 mm (Figure 15.3a).

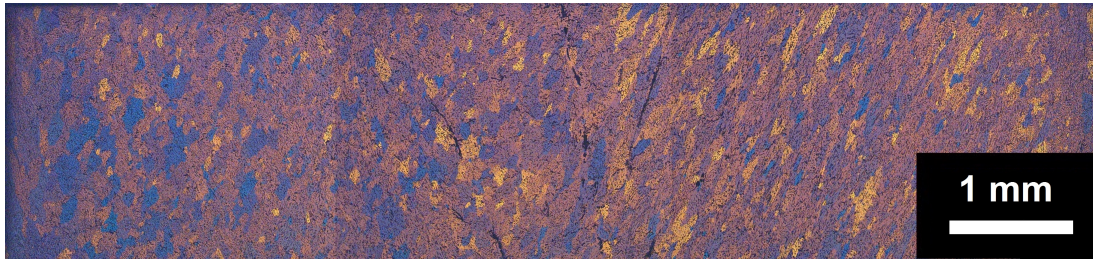
Observations by EBSD revealed that material AZ was after annealing at 300 °C composed of bimodal structure with smaller grains of average 2 μm and larger ones reaching 100 μm , which grew further during annealing. Zr-containing material DZ at 400 °C still preserved the sub-micrometric grain size. After further annealing to 450 °C the microstructure of DZ became bimodal with recrystallized grains reaching 100 μm and smaller ones, which retained size around 5 μm (see Figure 15.4). In both alloys before recrystallization the fraction of HAGB was ~ 0.8 , after recrystallization it reached ~ 0.9 .

15.3 Electrical resistivity

Evolution of electrical resistivity during isochronal annealing 20 K/20 min was measured on material C470 with addition of zirconium after ECAP (Figure 15.5a). Resistivity evolution exhibited significant difference between materials which were and which were not annealed prior to ECAP. In the non-annealed materials re-

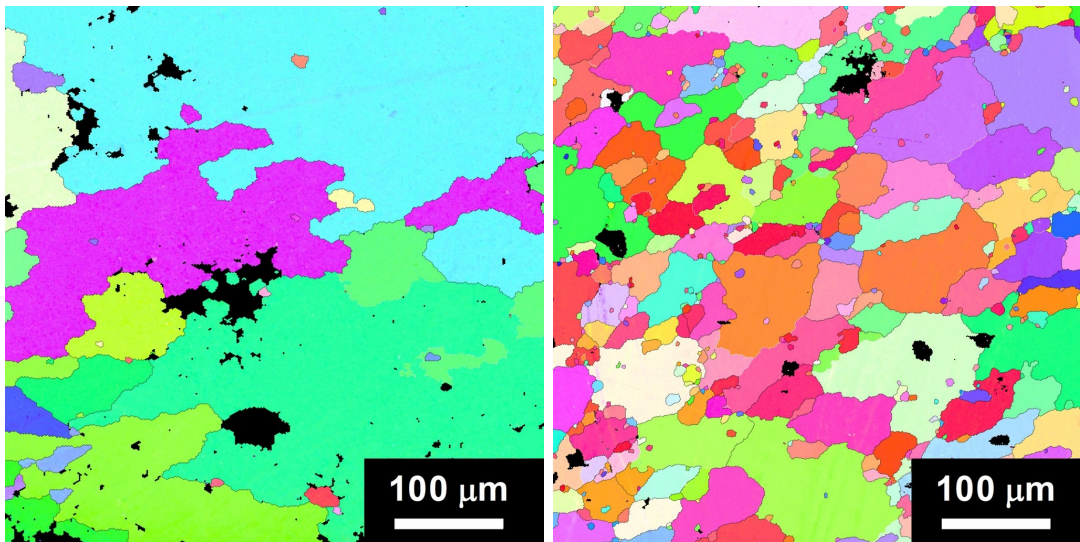


(a) AZ, 4 passes, 350 °C



(b) DZ, 4 passes, 450 °C

Figure 15.3: Through thickness grain structures of materials AZ and DZ after four ECAP passes and isochronal annealing to 350 °C and 450 °C, respectively. RD is vertical.



(a) AZ

(b) DZ

Figure 15.4: EBSD grain maps of materials AZ and DZ after four ECAP passes and isochronal annealing to 450 °C.

sistivity started to decrease moderately, the main drop occurred between 250 °C and 480 °C. This drop was connected with peaks in positive values in resistivity annealing spectra. With increasing number of ECAP passes magnitude of the peaks was shifted to lower temperatures. The onset of the peaks was shifted by nearly 100 °C to lower temperatures as compared to the as-cast material. Above 480 °C the resistivity started to increase.

The absolute values of electrical resistance were much lower in the pre-annealed materials. The drop of electrical resistivity was very shallow and increased with the deformation applied by ECAP. At 450 °C the distinct rise of resistivity took place. After annealing to 620 °C the absolute values of electrical resistance were comparable for both D and DZ materials.

15.4 Transmission electron microscopy

15.4.1 In-situ annealing

Several materials (D, DZ and AZ) were subjected to in-situ annealing in transmission electron microscope. This allowed observation of substructure recovery, grain growth, precipitation and particles dissolution on one spot in the material during the whole heating cycle. Heating scheme 50 K/50 min was applied: sample was heated to required temperature, held 50 minutes at this temperature and afterwards the temperature was raised again by 50 °C, and so on up to 550 °C. The micrographs of the microstructure evolution during annealing are depicted in Figure 15.7.

After four ECAP passes all studied materials contained high number of subgrains with an average size lower than 1 μm . Dislocation density was much higher in material D than in DZ and AZ. However, the main difference between the materials was the presence of secondary particles of $\alpha\text{-Al}(\text{Mn,Fe})\text{Si}$ phase in materials DZ and AZ, which were heat-treated before ECAP.

In-situ heating experiments revealed substantial microstructural changes in the course of annealing. During annealing at lower temperatures below 200 °C the dislocation substructure within the grains of the material D was nearly fully recovered. Subgrains after annealing at 150 °C contained only residual density of dislocations. In this material new particles of $\alpha\text{-Al}(\text{Mn,Fe})\text{Si}$ phase started to nucleate above 250 °C, preferentially on the subgrain boundaries. Their volume fraction and density grew up and reached maximum at 350 °C. At higher annealing temperatures their ripening and partial reversion to the solid solution was observed. At 500 °C only low number of coarser particles remained undissolved in the matrix. At annealing temperature around 450 °C significant subgrain growth occurred, creating a bimodal structure – a small amount of grains retained its sub-micron size while most of the matrix was composed of large grains with average size of several micrometers.

In the pre-annealed material DZ the $\alpha\text{-Al}(\text{Mn,Fe})\text{Si}$ particles were present in the matrix already before (and after) ECAP and no new precipitates formed during in-situ heating. Nevertheless, also these particles increased their average diameter at annealing temperatures below 350 °C and then, similarly as in the specimen D, their ripening and dissolution was observed. At 500 °C only a small number of coarse particles was present in the matrix. At 450 °C coalescence of

subgrains and rapid grain growth began and at 500 °C most of the grains reached the size of about 10 μm , only small fraction of them retained the micrometric size. The dislocation substructure recovered at temperatures below 200 °C

Concerning material AZ without Al_3Zr particles, no substantial differences from DZ were observed during the course of in-situ annealing. Some grains started to expand at 300 °C; however, the most pronounced grain growth took place between 450 °C and 500 °C as in the material DZ.

The grain size evolution during in-situ heating in TEM of materials after four ECAP passes is depicted in plot in Figure 15.5b. The values represent the average diameter of the grains on the spot, which was observed during the whole in-situ experiment (Figure 15.7). The increase of the grain size was fluent, indicating continuous recrystallization. No difference was detected between materials D and DZ. In AZ material without Zr the rise of grain size was steeper from temperature 450 °C. The smallest grains in the observed area had diameter approximately half of the average, the largest were around 5 μm .

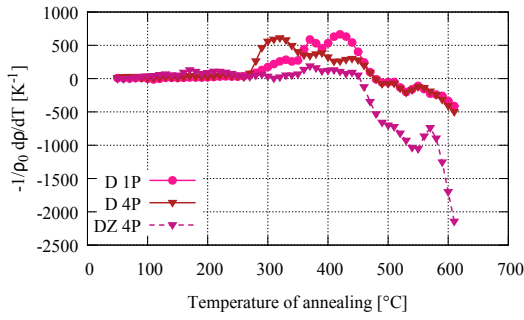
In the material after one ECAP pass the recovery of dislocation substructure took place during annealing to 300 °C and high angle grain boundaries formed. These boundaries started to migrate at 450 °C. $\alpha\text{-Al}(\text{Mn,Fe})\text{Si}$ particles nucleated from 300 °C, their partial dissolution began at 400 °C. They emerged both at the grain boundaries and inside the grains.

15.4.2 Post-mortem observations

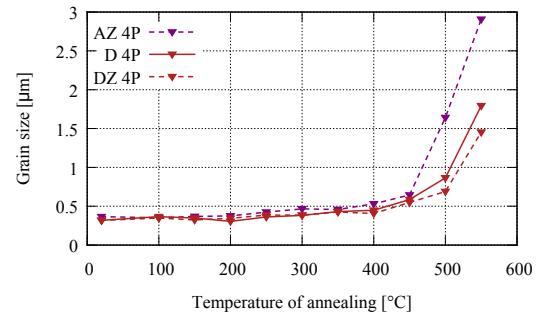
To evaluate the role of in-situ heating on the microstructure evolution, some of the materials were isochronally annealed in an air furnace with the same step as during in-situ experiments and were observed in TEM afterwards.

The main difference seemed to be in temperatures of precipitation and particles dissolution (see Figure 15.6 for example). During in-situ observations the particles formed at lower temperatures and their average diameter during annealing was higher and number density lower. At 500 °C most of the particles were already dissolved during in-situ processing; on the other hand, in materials annealed in an air furnace the precipitates density at 500 °C was still high.

Moreover, during in-situ TEM observation the recovery seemed to proceed more rapidly and the grain growth was limited and postponed to higher temperatures. In materials processed by ECAP the grain size after in-situ annealing was several μm , in conventionally annealed materials the grain size was much larger than 10 μm after annealing at 500 °C. Nevertheless, some regions in the material after one ECAP pass retained the grain size in order of 1 μm .

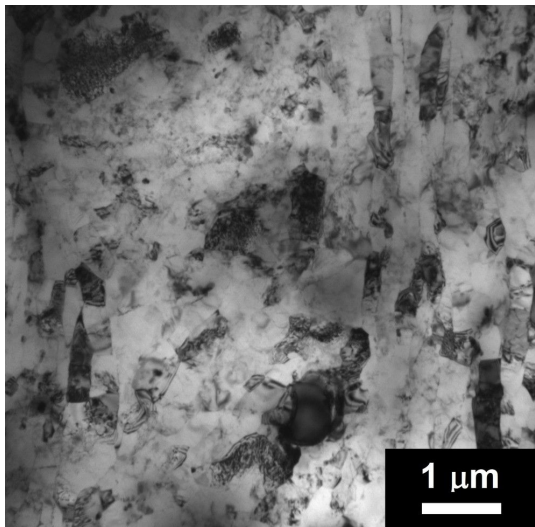


(a) Electrical resistivity

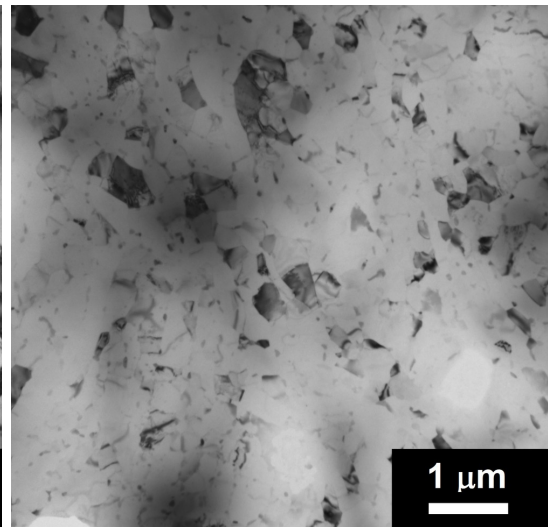


(b) Grain size

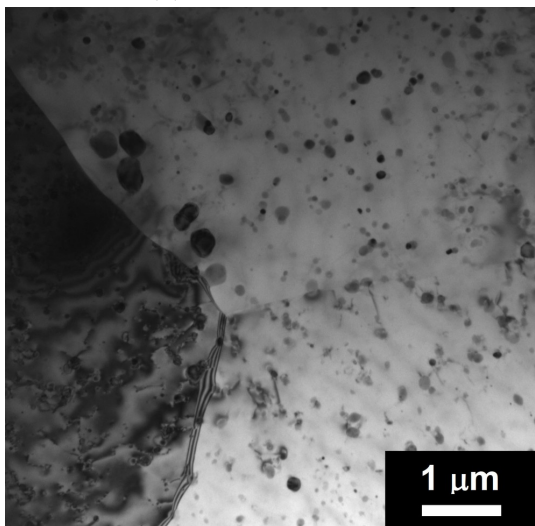
Figure 15.5: (a) The evolution of electrical resistivity during isochronal annealing 20 K/20 min for alloys with zirconium after one and four ECAP passes. (b) The evolution of average grain size measured during in-situ heating in TEM.



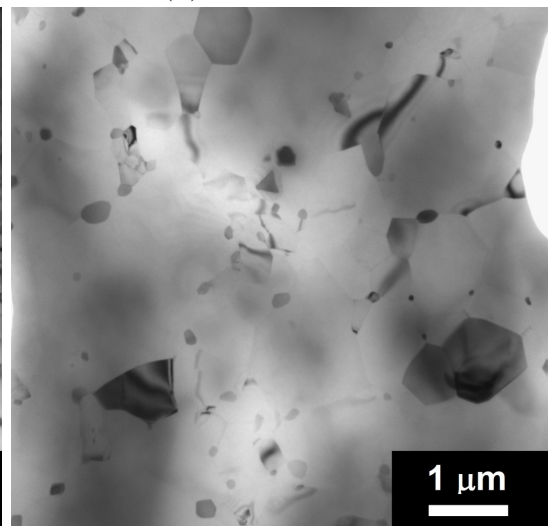
(a) Furnace, 300 °C



(b) In-situ, 300 °C



(c) Furnace, 500 °C



(d) In-situ, 500 °C

Figure 15.6: TEM micrograph from alloy D after four ECAP passes and annealing to 300 °C and 500 °C in an air furnace and by in-situ heating in TEM.

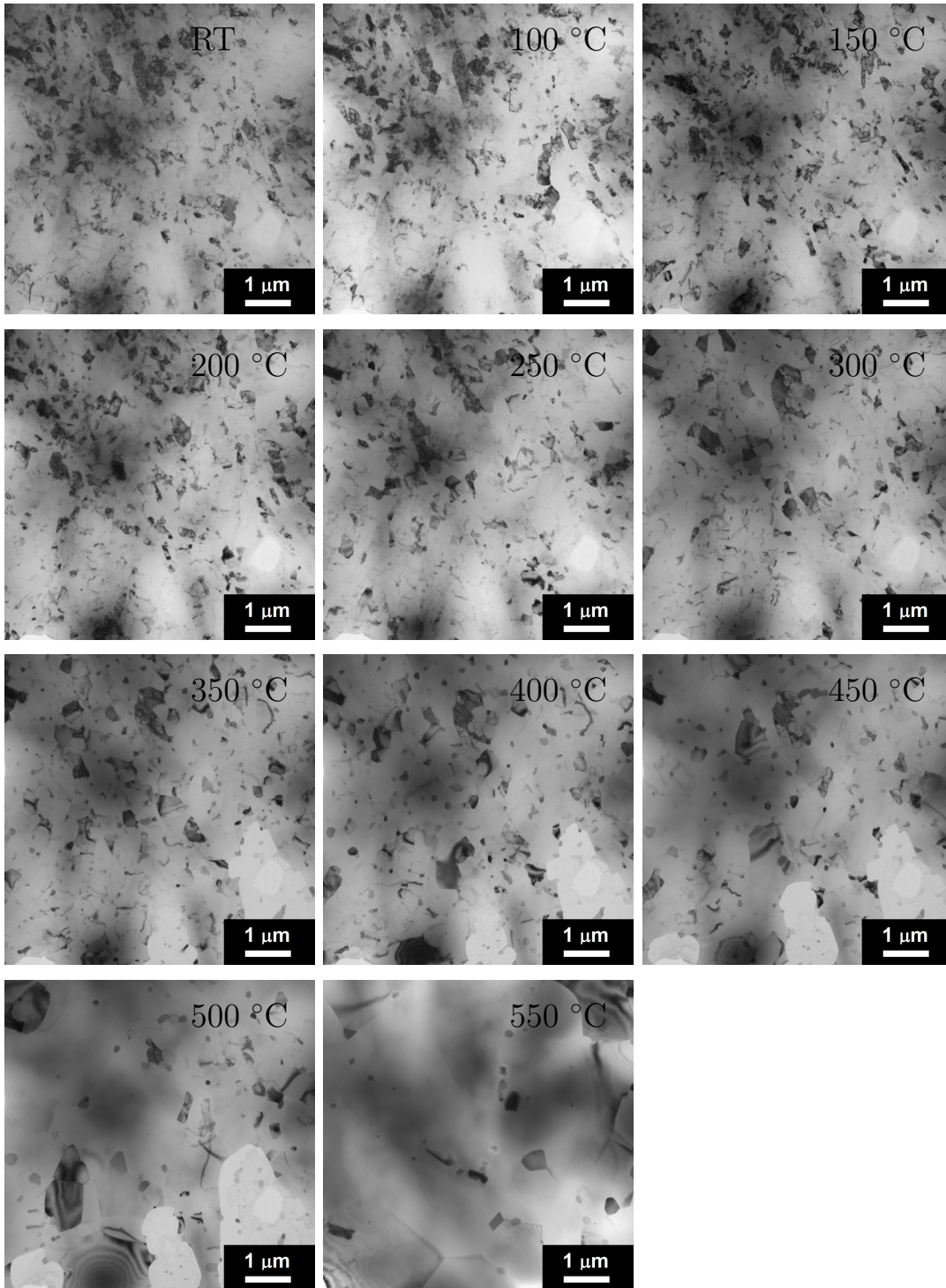


Figure 15.7: In-situ annealing in TEM of alloy C470 after four ECAP passes from room temperature to 550 °C.

16. Isothermal annealing

As isochronal annealing 50 K/50 min did not prove any significant differences in material with Zr between states which were or were not annealed prior to ECAP (materials D and DZ) – both recrystallized between 400 °C and 450 °C, isothermal annealing at 400 °C, 425 °C and 450 °C was applied in order to describe the kinetics of recrystallization. All three materials were subjected to isothermal annealing, only the pre-annealed alloy without Zr (AZ) was omitted, as it recrystallized at lower temperatures than other materials.

16.1 Vickers Microhardness

The evolution of Vickers microhardness during isothermal annealing at 400 °C, 425 °C and 450 °C from 0.5 to 16 hours is shown in Figure 16.1. Concerning materials after four ECAP passes, after a short annealing time at elevated temperature the microhardness dropped significantly from initial values of 100 HV0.1 for the non-annealed and 90 HV0.1 for the pre-annealed materials, respectively. At the highest investigated temperature 450 °C the microhardness drop was very steep in all investigated materials. After 30 minutes of annealing the average microhardness reached 50 HV0.1 and all alloys preserved this value during further exposure to 450 °C.

Fast decrease of the macrohardness values in specimens annealed at 400 °C and 425 °C for 0.5 hour to values between 70 and 75 HV0.1 was followed by a plateau. Nevertheless, after longer annealing times also at these temperatures the microhardness dropped to final value of about 50 HV0.1. Significantly shorter time between 2 and 4 hours was necessary at 425 °C, while at 400 °C the main HV drop from around 70 to 50 HV0.1 took place between 12 and 16 hours of annealing in materials with zirconium. In the material without Zr the HV drop was quicker at all temperatures (Figure 16.2a).

Annealing at 450 °C of materials ECAPed by only one pass led to HV decrease from approximately 85 HV0.1 to 75 HV0.1 after annealing up to 1 hour. Due further annealing the microhardness dropped slowly, reaching 50 HV0.1 after 8 hours. The values of HV were again lower for A material.

16.2 Microstructure

Light optical microscopy and scanning electron microscopy were used to study the evolution of the grain structure during annealing. After a short period at 450 °C part of the matrix contained new, recrystallized grains with an average size of 50 μm . The recrystallized fraction was higher in the pre-annealed materials. After 1 hour at 450 °C the microstructure was fully recrystallized in both materials pre-annealed and non-annealed prior to ECAP.

At 425 °C first recrystallization nuclei were observed after 1 hour in the pre-annealed materials and after 2 hours in the materials, which were not heat treated before ECAP. The full recrystallization occurred after 4 hours of annealing in both types of materials.

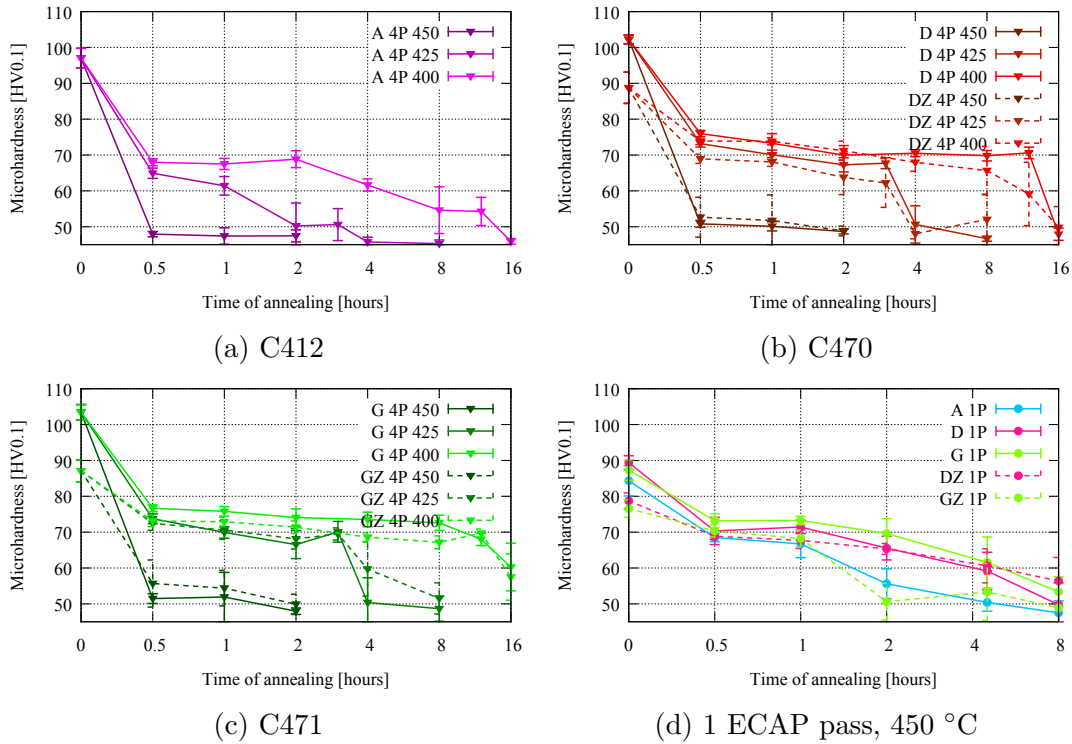


Figure 16.1: (a, b, c) The evolution of Vickers microhardness during isothermal annealing at 400 °C, 425 °C and 450 °C for all material after four ECAP passes and (d) at 450 °C for materials after one ECAP pass.

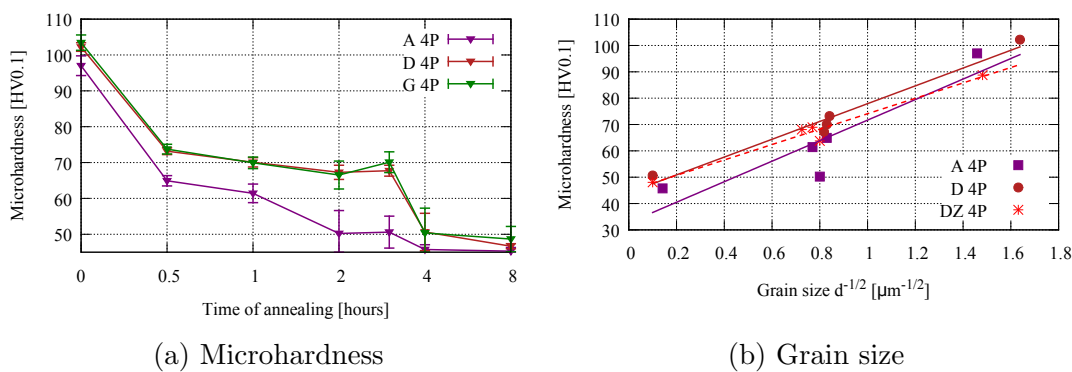


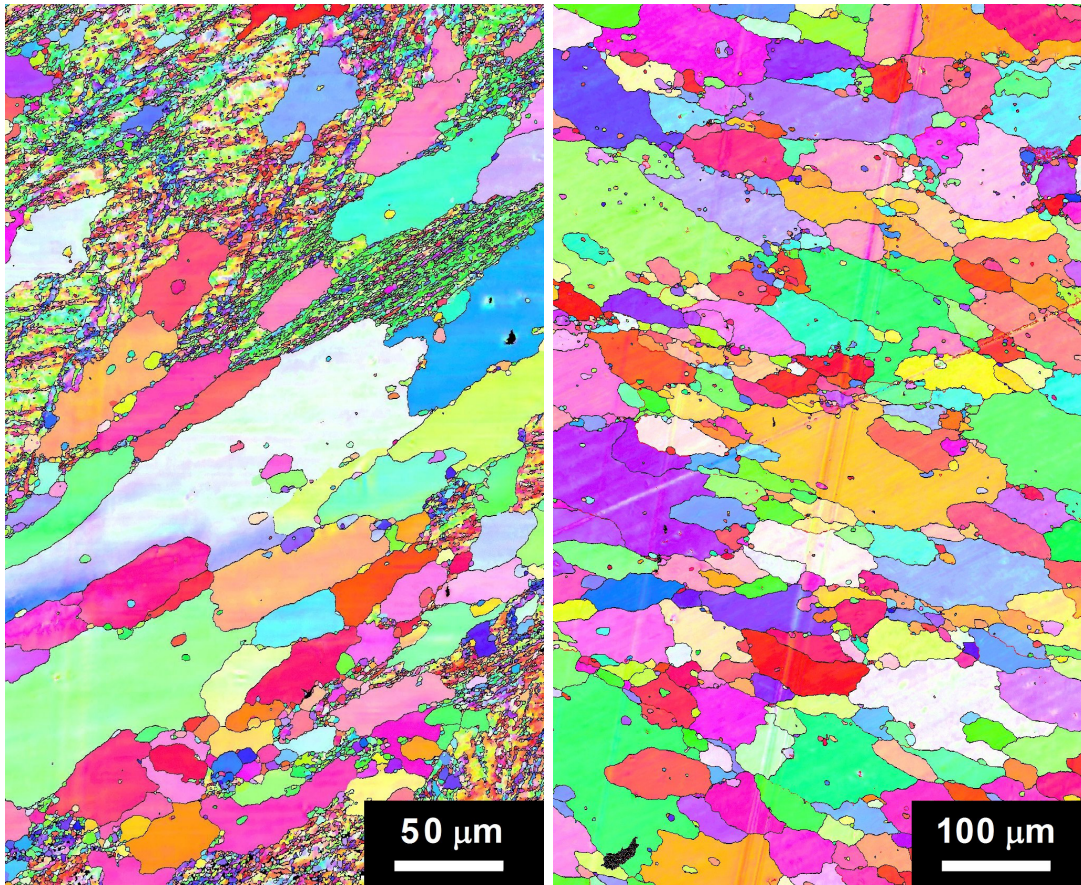
Figure 16.2: (a) The evolution of Vickers microhardness during isothermal annealing at 425 °C for materials after four ECAP passes. (b) The dependence of Vickers microhardness on the average grain size of materials during isothermal annealing at 425 °C, fit of Hall-Petch relation 1.18.

During heat treatment of materials with Zr at 400 °C, limited number of recrystallization nuclei was observed in the pre-annealed material after 4 hours. Full recrystallization took place after 16 hours in both types of materials; however, the first traces of recrystallization in the non-annealed materials were not observed until 8 hours of annealing. After recrystallization at all temperatures the microstructure was bimodal with large grains of the size in order of hundreds of μm . Also considerable number of smaller grains with average diameter in the order of 10 μm was present in the material. The HAGB fraction reached ~ 0.9 .

Observations in SEM by EBSD enabled examination of the grain structure. After four ECAP passes materials were comprised of sub-micrometric grains which were separated by high angle boundaries. During initial stages of annealing at elevated temperature the average grain size increased slightly from 0.4 μm to approximately 1 μm . Due further annealing these grains were stable to the point, where grains of size 20-100 μm started to appear. This new grains were separated by high angle grain boundaries. After 3 hours at 425 °C half of the microstructure of material D was comprised of micrometric grains or subgrains, the second half was built up of new grains with no subgrain substructure (Figure 16.3a). Further annealing to 4 hours resulted in full transformation to coarse-grained structure. However, small grains with diameter around 10 μm inside the large ones were observed (Figure 16.3b), which confirmed the observation in LOM.

Precipitation of $\alpha\text{-Al(MnFe)Si}$ phase was another effect of isothermal annealing at all temperatures. Examinations in TEM and SEM (Figure 16.4) showed that high density of these particles was present in all materials after heat treatment. In the material, which was not annealed prior to ECAP, all precipitates were newly formed. They were located mainly on the grain boundaries. In the pre-annealed material, the precipitates, which were present in the matrix before ECAP, coarsened and new ones formed.

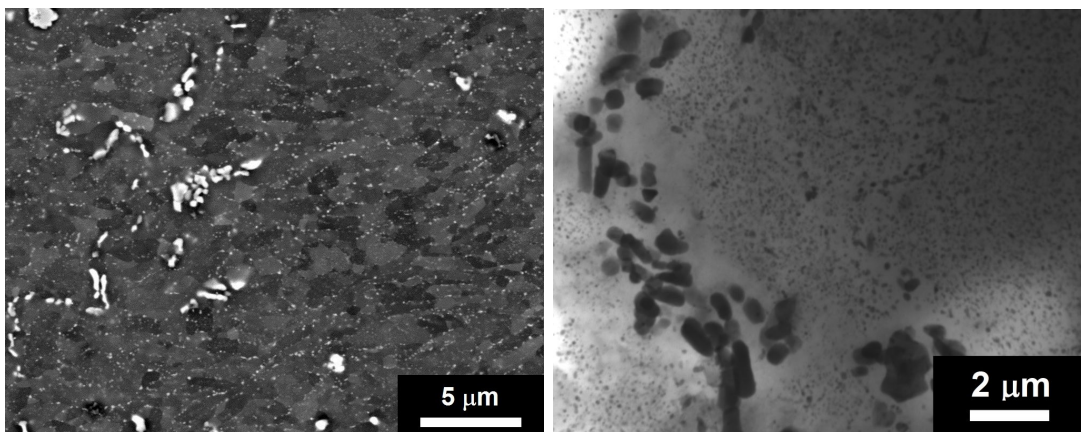
Application of Hall-Petch relationship (Eq. 1.18) on microhardness and grain size evolution during isothermal annealing at 425 °C revealed linear dependance of microhardness on inverse square root of average grain size (Figure 16.2b). Fitted parameters from Equation 1.18 are $H_0 = 32 \pm 4 \text{ HV}0.1$ and $K_H = 42 \pm 4 \text{ HV}0.1 \cdot \mu\text{m}^{1/2}$, which are comparable with values obtained by other researchers (e.g. [58, 115]).



(a) 3 hours at 425 °C

(b) 4 hours at 425 °C

Figure 16.3: EBSD orientation map of material with Zr after four ECAP passes and annealing at 425 °C. After 3 hours at 425 °C part of the microstructure retained ultrafine grains, in other parts grains grew to size around 100 μm. After 4 hours the microstructure is bimodal with large grains around 100 μm and smaller grains with size around 10 μm inside them.



(a) D, 2 hours at 425 °C

(b) DZ, 1 hour at 450 °C

Figure 16.4: (a) BSE image of material D after four ECAP passes and annealing for 2 hours at 425 °C. (b) TEM micrograph of material DZ after four ECAP passes and annealing for 1 hour at 450 °C.

17. High temperature deformation

17.1 Mechanical properties

Materials after ECAP were tested by high temperature deformation to find out, whether they exhibit superplastic behaviour. The tests were undertaken at temperatures between 350 °C and 450 °C.

The results from tensile tests are shown in Figure 17.1. Processing by four ECAP passes significantly increased both ductility and the value of strain rate sensitivity parameter m (Eq. 1.19). Materials, which were not annealed prior to ECAP, exhibited higher values of ductility and m – 4-5 times higher than materials before ECAP. However, mechanical properties of the pre-annealed material C412 without Zr, which recrystallized during isochronal annealing at lower temperature than other materials after four ECAP passes, were close to properties of the material before ECAP.

With increasing temperature of tensile test both ductility and m rose. Nevertheless, above the temperature of recrystallization (~ 450 °C for most of the materials), both ductility and m dropped significantly (see Figure 17.1b).

The maximal parameter m was measured in non-annealed materials after four ECAP passes; however, its value barely reached the lower limit for superplastic behaviour, which is $m = 0.3$.

The Vickers microhardness measurements showed the distribution of microhardness after the tensile tests (see Figure 17.2). In non-deformed part of the sample microhardness dropped by ~ 20 %, in the deformed section the drop was more pronounced. The closer to the point of fracture, the lower was the HV.

17.2 Microstructure

Observations in TEM and analysis by EBSD showed that the average grain size of materials after ECAP (~ 0.4 μm) increased during tensile testing at 400 °C. This growth was more apparent in the deformed area of the sample, near the fracture point. Also significant elongation of grains in the direction of tensile loading was observed – Figure 17.3. In the undeformed section of the sample the average grain size reached ~ 2 μm , in the deformed part it was $\sim 2 \times 5$ μm . The increase of the grain size was closely connected to the microhardness drop in the deformed part of the samples.

The average grain size of material AZ after testing at 400 °C was several hundreds of μm in length and ~ 100 μm perpendicular to the direction of tensile loading.

Due to exposure to 400 °C during tensile testing, massive precipitation of $\alpha\text{-Al}(\text{Mn,Fe})\text{Si}$ phase was observed in all materials. This phenomenon was more pronounced in the materials which were not heat treated before ECAP, as no precipitates were present in aluminium matrix before and after deformation and all formed during heating and tensile tests.

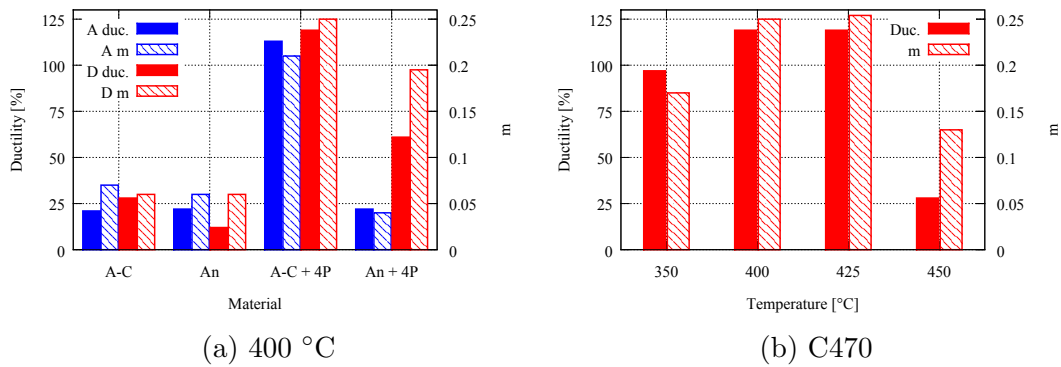


Figure 17.1: (a) Ductility and strain rate sensitivity parameter m for alloys C412 and C470 in as-cast state (A-C), annealed for 8 hours at 450 °C (An) and processed by four ECAP passes (4P). The tensile test were performed at 400 °C. (b) Ductility and m parameter for alloy C470 processed by four ECAP passes for different temperatures of tensile tests.

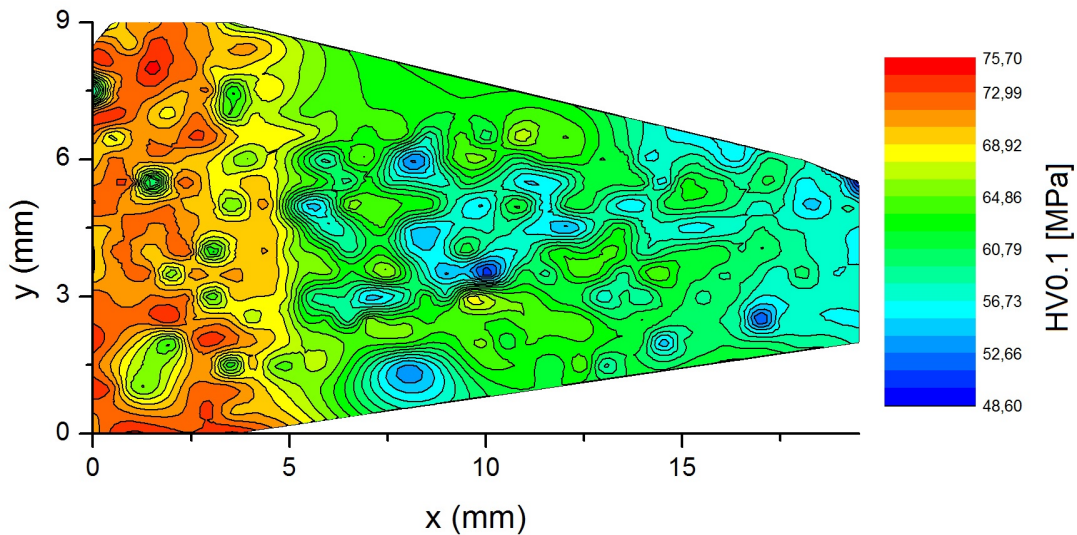


Figure 17.2: Map of Vickers microhardness on a specimen after high temperature tensile testing at 400 °C – undeformed part at left, point of fracture at right. Material C470, annealed at 450 °C, after four ECAP passes.

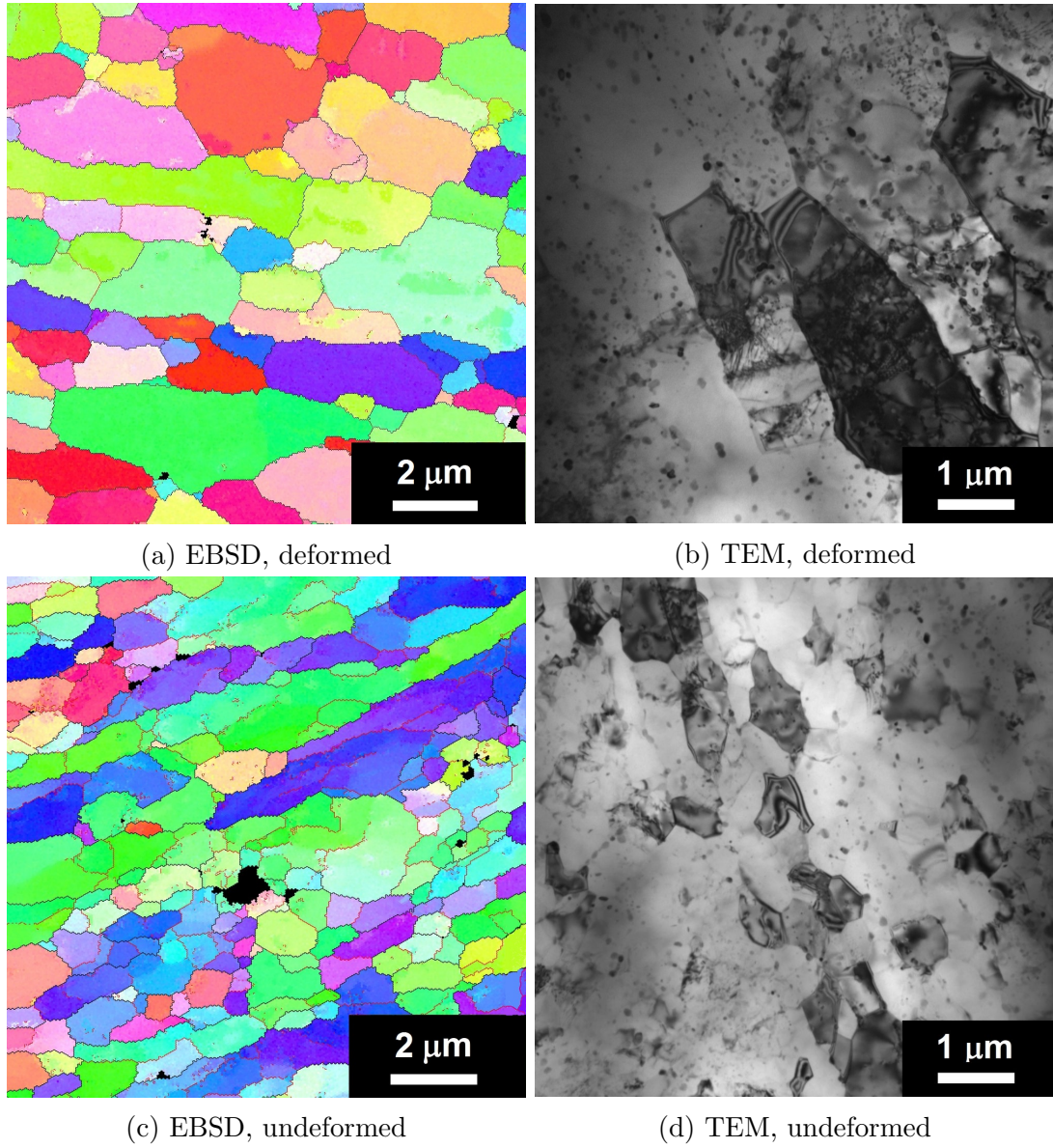


Figure 17.3: EBSD orientation map and TEM micrograph of material C470 after four ECAP passes and tensile testing at 400 °C, deformed area near the fraction point and undeformed part.

18. Discussion

Similarly to other Al-based alloys, the equal channel angular pressing is an effective tool for microstructure refinement also in the TRC Al-Mn-based alloys. The grain size after four ECAP passes was $\sim 0.5 \mu\text{m}$, i.e. it was lower in comparison with Al-Zn-based [126] or Al-Mg-based alloys [117] after ECAP. Explanation could be found in a lower ECAP temperature in the Al-Mn-based alloys which did not allow grain coarsening at higher number of ECAP passes.

Development of an ultrafine-grained structure was completed after four ECAP passes. Further increase in ECAP deformation led to elongation of newly formed grains. A similar microstructure development during ECAP was observed in a chill cast Al-Mn-Sc-Zr alloy with a reduced Fe+Si content [127]. Such process did not significantly influence the deformation characteristics and both the strength and ductility were very close in samples after four and eight ECAP passes, respectively.

The main increase in strength characteristics occurred already during the first ECAP pass. The microstructure analysis documented clearly that not the ultrafine grain size but very high dislocation density was responsible for this effect.

The Al_3Zr particles were introduced into the alloys in order to retard recrystallization and grain growth. Annealing at $450 \text{ }^\circ\text{C}$ prior to ECAP resulted additionally in precipitation of the $\alpha\text{-Al}(\text{Mn,Fe})\text{Si}$ particles and thus in the reduction of Mn atoms dissolved in the aluminium matrix. The higher strengthening effect of ECAP in the non-annealed materials can be thus explained by the higher content of Mn remaining in the solid solution. Mn atoms are very effective in hindering dislocation motion and suppression of recovery processes. Therefore, deformation energy stored in the non-annealed materials was higher than in the annealed ones. The manganese atoms remaining in aluminium solid solution in non-annealed materials seemed to have a greater stabilizing effect than the Al_3Zr particles present simultaneously with the $\alpha\text{-Al}(\text{Mn,Fe})\text{Si}$ particles in annealed materials.

However, the increased dislocation density in materials non-annealed prior to ECAP, which led to higher microhardness values, made further processing more difficult and materials cracked.

Isochronal annealing

Comparing the microstructure of the pre-annealed alloys, the presence of Al_3Zr particles was found to have a major influence on the thermal stability of the deformed materials. During isochronal annealing with heating rate $50 \text{ K}/50 \text{ min}$ softening of materials, indicated by a decrease of the microhardness, was caused by substructure recovery and recrystallization. In-situ transmission electron microscopy showed that recrystallization occurred in a continuous manner. During the continuous recrystallization highly deformed alloy may transform during annealing by relatively localized boundary migration to a microstructure of approximately equiaxed defect-free grains, which are predominantly bounded by high angle grain boundaries. It has been shown [73, 113] that the continuous recrystallization is promoted by large strains induced into the material and by second-phase particles, which is the case of the studied materials, as a dense dis-

persion of secondary particles of α -Al(Mn,Fe)Si phase was achieved by annealing at 450 °C prior to ECAP processing.

Al₃Zr precipitates beneficially contributed to the shift of recrystallization and the main microhardness decrease to temperature range of 400-450 °C in the Zr-containing materials C470 and C471, unlike the C412 material which recrystallized between 300 °C and 350 °C. The average grain size after isochronal annealing was much lower in the Zr-containing materials, which was another positive effect of the Al₃Zr particles — they pin moving grain boundaries and inhibit grain growth.

The situation was different in the case of materials which were not heat treated before deformation – recrystallization in both materials with and without Zr addition took place between 400 °C and 450 °C.

From another point of view, materials D and DZ were compared to evaluate the role of pre-annealing at 450 °C. In the course of isochronal annealing of material D, dislocation density dropped via recovery of the substructure and microhardness gradually decreased. As new precipitates of α -Al(Mn,Fe)Si phase nucleated at temperatures above 250 °C, aluminium matrix was depleted from manganese; this process also contributed to microhardness drop.

In the case of material DZ, dislocation density within subgrains was low and no new particles nucleated, thus, depletion of solid solution was modest; the microhardness decrease was much less pronounced.

The initial deformed microstructure after ECAP processing also influenced the subsequent mechanisms of hardening and softening at elevated temperatures. The initial faint increase of microhardness below 150 °C observed in the D specimen might be associated with the mechanism observed in heavily deformed aluminium by Huang et al. [128]. Decrease of dislocation density and formation of well developed small subgrains can result in surprising rise of the strength of the material. As dislocations are annealed out, higher tensile stress is required to activate new dislocation sources to enable deformation [129]. As material DZ already contained small subgrains with well developed subgrain boundaries and very low dislocation density in their interior, no such increase of HV was observed in this material.

The presence of Al₃Zr precipitates in pre-annealed material DZ was responsible for the shift of the recrystallization temperature by 100 °C to higher values when compared to the alloy without Zr addition pre-annealed in the same manner as the material DZ. On the other hand, no Al₃Zr precipitates were present in the material D after ECAP. Because the recrystallization temperature during isochronal annealing was the same for both materials, different mechanism has to be attributed for recrystallization resistance of material D.

During the in-situ heating in TEM new α -Al(Mn,Fe)Si precipitates formed preferentially on the subgrain boundaries and the boundaries were pinned by these particles up to temperatures around 450 °C when particle dissolution occurred. This phenomenon is in accordance with previous work (e.g. [66]) where it was shown that in cold-rolled aluminium alloys second-phase particles, which nucleated from the solid solution during subsequent heat treatment, interact with moving dislocations and pin grain boundaries more effectively; they could thus postpone recrystallization to higher temperatures (by approximately 100 °C) as compared to materials, where the secondary particles were present before defor-

mation.

Although no Al_3Zr precipitates were observed in the D specimen at 450 °C by TEM, their presence in the form of very small particles (diameter less than 1-2 nm) could not be excluded. Their eventual presence is very probable because the annealing temperature and time correspond with the initial phases of the Al_3Zr particle formation in the DZ specimen. Therefore their role as recrystallization inhibitors could not be omitted. Moreover, they may be responsible for the slight microhardness increase above HV of material C412.

The pronounced drop of HV between 400 °C and 450 °C was connected with the nucleation of new grains and recrystallization. Recrystallization began in the center of the billets. During twin-roll casting central segregates of eutectic phase $\alpha\text{-Al}(\text{Mn,Fe})\text{Si}$ were formed in the center of the foil. The aluminium matrix in the vicinity of these segregates was depleted from atoms of alloying elements and only limited number of precipitates formed in this area. As there were almost no particles to pin moving grain boundaries, recrystallization began preferentially from the central segregates. These segregates also can serve as preferential sites for nucleation of new grains through particle simulated nucleation.

According to in-situ TEM observation, recrystallization was also connected with dissolution of secondary particles. As the precipitates were formed mainly on the subgrain boundaries, motion of the boundaries was hindered by the particles. At 450 °C most of the precipitates were dissolved or too coarse to effectively pin the grain boundaries and grain boundaries started to migrate.

The stored deformation energy is connected with the driving force for recovery and recrystallization. Thus, the continuous drop of microhardness at the first stage of annealing resulting from recovery was steeper and recrystallization, which is responsible for the HV reduction in the second stage, started at lower temperatures for the materials subjected to higher number of ECAP passes. The shallowest was the microhardness decrease in materials subjected to only one ECAP pass.

Resistivity measurements and observations by TEM of samples annealed in an air furnace revealed discrepancies between in-situ and post-mortem observations in TEM. According to resistivity measurements precipitation in material D started at temperatures above 260 °C, number of precipitates observed by conventional TEM was still quite low at 300 °C. However, first precipitates were observed during in-situ heating at 250 °C. The highest number of precipitates was present in the material at ~ 350 °C during in-situ and at ~ 500 °C during post-mortem observations. Moreover, the number density and average size of precipitates were different – during in-situ heating the precipitates were coarser and their number density was lower. Recovery processes were quicker during in-situ annealing. On the contrary, grain growth was suppressed and the grain size at 550 °C was much lower after in-situ annealing. Both resistivity and microhardness measurements were undertaken on samples annealed in furnace and their results corresponded to post-mortem microscopic observations.

The main difference is in two-dimensional nature of in-situ observations in TEM. During in-situ annealing recovery is sped up as free surface, where dislocations can annihilate, form high fraction of the TEM foil. As the precipitates nucleated at lower temperature, their number density was lower and during further annealing atoms of solute elements were consumed on coarsening of the

existing precipitates rather than on nucleation of new ones. HAGB were more stable as they were fixed by the free surface and higher temperature was necessary for their motion. Moreover, as dislocation density was reduced more quickly during in-situ annealing, driving force for recrystallization and grain growth was lower as compared to conventionally annealed materials. Thus, recrystallization was postponed to higher temperatures.

Isothermal annealing

During isothermal annealing at elevated temperatures the sub-micrometric grains were replaced by new grains with size comparable to the ones observed before plastic deformation by ECAP. However, the grain distribution was inhomogeneous and some of the grains retained smaller size around 10 μm . The time necessary for full recrystallization highly depended on annealing temperature. Concerning material C470 after four ECAP passes, at 400 °C it took 16 hours for full recrystallization, at 425 °C only 4 hours. At the highest applied temperature 450 °C the recrystallization was very fast, high fraction of the matrix recrystallized already during 10 minutes of exposure to the elevated temperature. The time required for recrystallization at all selected temperatures did not depend on the alloy pre-treatment. This means that the initial annealing at 450 °C, which was conducted in order to enhance thermal stability of the alloy at high temperatures, did not meet the requirement. Moreover, first recrystallized grains emerged at a given temperature in the pre-annealed material after shorter annealing time than in the non-annealed one. This may be caused by the depletion of the matrix from Mn and also by a higher density of $\alpha\text{-Al(Mn,Fe)Si}$ phase particles, which were present in the matrix prior to isothermal annealing. Such particles can promote recrystallization by serving as preferential nucleation sites for recrystallization through the particle stimulated nucleation. Both effects thus can override the beneficial influence of Al_3Zr precipitates.

The recrystallization was slightly faster in material C412 without Zr. The distribution of $\alpha\text{-Al(Mn,Fe)Si}$ particles was similar in both materials with and without Zr, so their contribution to recrystallization resistance should be comparable. This fact confirms the positive influence of zirconium even in the material D, where Al_3Zr precipitates were not detected.

Due to lower stored deformation energy in materials after one ECAP pass, their recrystallization at 450 °C took much longer time than for materials after four passes – between 2 and 8 hours depending on the alloy and heat pre-treatment.

The increase of average grain size during annealing was interconnected with microhardness via Hall-Petch relation – the values of microhardness dropped with increasing square root of average grain size.

Superplasticity

Finally, deformed materials were subjected to dynamic testing by high temperature tensile tests to examine, whether they manifest superplastic behaviour. The ultrafine-grained structure was introduced into the material by ECAP and it was shown by static testing, that thanks to zirconium addition the UFG structure remained stable up to several hours of annealing at 425 °C.

However, none of the materials exhibited properties corresponding to superplasticity. This can be attributed to dense population of secondary particles. These are known to retard sliding of HAGB, which is the main deformation mechanism during superplastic deformation [119]. These particles were already present in the pre-annealed material and obstructed superplastic behaviour more efficiently than those in material non-annealed prior to ECAP. There the secondary particles formed during high temperature deformation. Moreover, the initial grain structure was not homogeneous and still reasonable fraction (~ 0.3) of the grain boundaries were LAGB. Only HAGB can contribute to superplasticity.

The degradation of mechanical properties during testing at 450 °C was in accordance with microstructure observations which showed rapid recrystallization at this temperature.

Part V
Conclusion

19. Discussion

19.1 Precipitation

After twin-roll casting most of the solute elements were dissolved in solid solution of aluminium. Heat treatment at elevated temperatures led to decomposition of the solid solution via precipitation of second-phase particles. The predominant phase occurring in AA3003 aluminium alloys is α -Al(Mn,Fe)Si phase. Cubic morphology of this phase was observed in all studied materials.

Precipitation kinetics was studied by the means of electrical resistivity measurements. Deformation implied into the material had a significant influence on the course of precipitation (Figure 19.1a). In the as-cast materials precipitation started around 370 °C; however, deformation shifted start of precipitation to lower temperatures by ~ 100 °C. Both deformation by cold-rolling and ECAP influenced the precipitation in the same manner.

Precipitation was divided into several stages. The higher was the imposed strain, the more pronounced was the first stage, where precipitates nucleated at subgrain boundaries. Comparing cold-rolled and ECAPed materials, four ECAP passes induced into the material strain ~ 4 , cold-rolling to 1 mm induced strain ~ 2 . The first stage reached maximum earlier in material after four ECAP passes (see Figure 19.1a) than in the cold-rolled one. Processing by only one ECAP pass induced strain ~ 1 and resulted in prevailing of precipitation at higher temperatures.

19.2 Recrystallization

After deformation by cold-rolling and ECAP, high dislocation density was introduced into the materials and aluminium matrix was in non-equilibrium state. In the course of heat treatment the stored deformation energy was released by recovery and recrystallization and new grain structure formed.

All deformed materials were subjected to high temperature annealing in order to evaluate their thermal stability. Influence of the strain imposed into the material by deformation played the main role on the temperature of recrystallization (Figure 19.1b). The higher was the imposed strain, the lower was the recrystallization resistance of the material; moreover, more pronounced was the softening of the material prior to recrystallization. The microhardness decreased to ~ 70 HV0.1 before the main drop connected with recrystallization regardless the type of deformation. After recrystallization the grain size reached values similar to as-cast states – 100 μm and microhardness of all materials was the same.

In materials pre-annealed prior to deformation, recrystallization was substantially influenced by presence of zirconium in the alloys. In non-annealed materials deformed by both cold-rolling and ECAP, the difference was milder.

In Zr-containing alloys heat pre-treatment did not influence the recrystallization temperature. However, the recrystallization resistance was achieved by different mechanisms – in pre-annealed alloys it was presence of Al_3Zr , in non-annealed ones it was mainly precipitation of α -Al(Mn,Fe)Si phase.

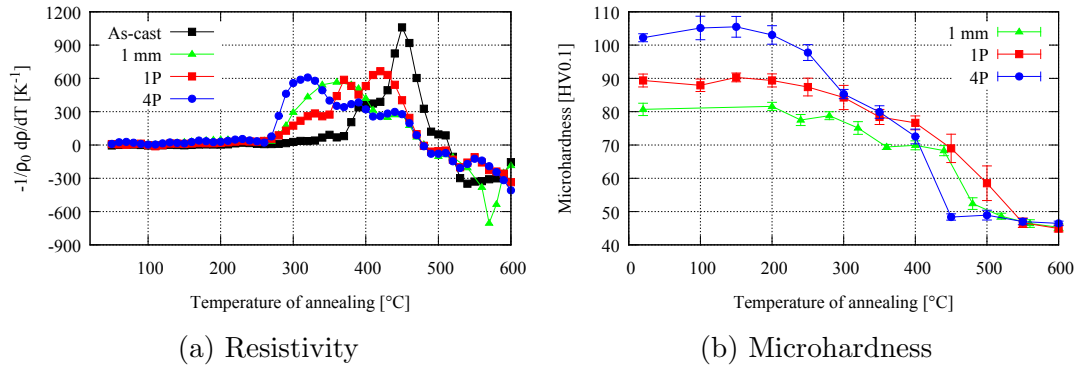


Figure 19.1: Resistivity annealing spectra and evolution of Vickers microhardness during isochronal annealing of material C470 in as-cast state, cold-rolled to 1 mm and processed by one and four ECAP passes.

19.3 Zirconium and chromium

Zirconium and chromium were added into the alloys in order to enhance recrystallization resistance and refine the grain structure. Zirconium formed Al_3Zr precipitates which postponed recrystallization in annealed alloys after ECAP by 100 °C. However, they did not influence temperature of recrystallization concerning the same material with and without Al_3Zr particles.

Comparing alloys with and without Zr which were not annealed for Al_3Zr precipitates formation, recrystallization resistance was also slightly higher in alloys with Zr, both after cold-rolling and ECAP. Thus, clusters of Zr atoms, which formed during recrystallization annealing, can be also attributed for enhanced recrystallization resistance.

However, no significant differences were observed between material with Zr and with both Zr and Cr. Chromium was found to incorporate into α -phase particles to form $\alpha\text{-Al}(\text{Mn},\text{Fe},\text{Cr})\text{Si}$.

20. Conclusion

Three twin-roll cast alloys from AA3003 series were studied. After casting the microstructure was unhomogeneous with eutectic macrosegregations in center of the foils and elongated grains near the foil surface.

Firstly, precipitation of second-phase particles was monitored. The precipitation took place in temperature range 300-500 °C and was divided into two main stages. At lower temperatures precipitates formed at subgrain boundaries, later also in grain interior. Both precipitates and primary particles, which were present in the material after casting, were cubic α -Al(Mn,Fe)Si phase with lattice parameter 1.26 nm. With applied deformation the precipitation shifted to lower temperatures and the first stage became more pronounced.

In the next step conditions for precipitation of coherent Al₃Zr precipitates were found. High density of these particles formed in alloys with zirconium addition during annealing to 450 °C with heating rate 0.5 K/min. During holding at 450 °C their number density further increased.

Finally, alloys were subjected to severe plastic deformation by equal channel angular pressing. Materials with and without zirconium and annealed and non-annealed prior to ECAP were compared. Four ECAP passes led in all materials to substantial grain size reduction and strength increase. During exposure to elevated temperatures ultrafine grains were replaced by larger ones via recrystallization. In annealed materials recrystallization resistance was enhanced by presence of Al₃Zr particles. In non-annealed alloys recrystallization was postponed by precipitation of α -Al(Mn,Fe)Si particles and probably also by clusters zirconium. The higher was the applied temperature, the more rapid was recrystallization. Also the strain induced into the material by deformation accelerated recrystallization.

Both precipitation and recrystallization were observed by in-situ heating in transmission electron microscope. However, mechanical properties evolution corresponded to microstructures, which were achieved by conventional ways of annealing.

Bibliography

- [1] J. E. Hatch, *Aluminum: Properties and Physical Metallurgy*, 1st ed. Metals Park: ASM, 1984.
- [2] Š. Michna, I. Lukáč, V. Očenášek, R. Kořeněný, J. Drápala, H. Schneider, and A. Miškuřová, *Encyklopedie Hliníku*, 1st ed. Prešov: Adin, s r. o., 2005.
- [3] P. Stadelman, “JEMS Electron Microscopy Software,” [software], cited 12/10/2009, version 3.4711U2009, Switzerland.
- [4] D. T. L. Alexander and A. L. Greer, “Solid-state intermetallic phase transformation in 3XXX aluminium alloys,” *Acta Materialia*, vol. 50, pp. 2571–2583, 2002.
- [5] M. Dehmas, P. Weisbecker, G. Geandier, P. Archambault, and E. Aeby-Gautier, “Experimental study of phase transformation in 3003 aluminium alloys during heating by in situ high energy X-ray synchrotron radiation,” *Journal of Alloys and Compounds*, vol. 400, pp. 116–124, 2005.
- [6] A. Mamala and W. Sciezor, “Evaluation of the effect of selected alloying elements on the mechanical and electrical aluminium properties,” *Archives of Metallurgy and Materials*, vol. 59, pp. 413–416, 2014.
- [7] T. Pettersen, Y. Li, T. Furu, and K. Marthinsen, “Effect of Changing Homogenization Treatment on the Particle Structure in Mn-containing Aluminium Alloys,” *Materials Science Forum*, vol. 558-559, pp. 301–306, 2007.
- [8] M. Karlík, T. Mánik, M. Slámová, and H. Lauchmann, “Effect of Si and Fe on the Recrystallization Response of Al-Mn Alloys with Zr addition,” *Acta Physica Polonica A*, vol. 122, pp. 469–474, 2012.
- [9] N. A. Belov, D. G. Eskin, and A. A. Askenov, *Multicomponent Phase Diagrams: Applications for Commercial Aluminum Alloys*, 1st ed. Elsevier, 2005.
- [10] L. F. Mondolfo, *Aluminium Alloys: Structure and Properties*, 1st ed. London: Butterworths, 1976.
- [11] G. Davignon, A. Serneels, B. Verlinden, and L. Delaey, “An Isothermal Section at 550 °C in the Al-Rich Corner of the Al-Fe-Mn-Si System,” *Metallurgical and Materials Transactions A*, vol. 27A, pp. 3357–3361, 1996.
- [12] T. Carlberg, M. Jaradech, and H. K. Kamga, “Solidification Studies of Automotive Heat Exchanger Materials,” *Journal of the Minerals, Metals and Materials Society*, vol. 58, pp. 56–61, 2006.
- [13] M. Warmuzek, G. Mrówka, and J. Sieniawski, “Influence of the heat treatment on the precipitation of the intermetallic phases in commercial AlMn1FeSi alloy,” *Journal of Materials Processing Technology*, vol. 157-158, pp. 624–632, 2004.

- [14] M. Warmuzek, K. Rabczak, and J. Sieniawski, "The course of the peritectic transformation in the Al-rich Al-Fe-Mn-Si alloys," *Journal of Materials Processing Technology*, vol. 162-163, pp. 422–428, 2005.
- [15] Y. Birol, "Homogenization of a twin-roll cast thin Al-Mn strip," *Journal of Alloys and Compounds*, vol. 471, pp. 122–127, 2009.
- [16] M. Warmuzek, J. Sieniawski, K. Wicher, and G. Mrówka, "The study of the distribution of the transition metals and Si during primary precipitation of the intermetallic phases in Al-Mn-Si alloys," *Journal of Materials Processing and Technology*, vol. 175, pp. 421–426, 2006.
- [17] Y. J. Li and L. Arnberg, "Evolution of eutectic intermetallic particles in DC-cast AA3003 alloy during heating and homogenization," *Materials Science and Engineering A*, vol. 347, pp. 130–135, 2003.
- [18] M. Dehmas, R. Valdés, M.-C. Lafont, J. Lacaze, and B. Viguier, "Identification of intermetallic precipitates formed during re-solidification of brazed aluminium alloys," *Scripta Materialia*, vol. 55, pp. 191–194, 2006.
- [19] Y. J. Li and L. Arnberg, "Quantitative study on the precipitation behaviour of dispersoids in DC-cast AA3003 alloy during heating and homogenization," *Acta Materialia*, vol. 51, pp. 3415–3428, 2003.
- [20] M. Dehmas, P. Archambault, M. Serriere, E. Gautier, and C.-A. Gandin, "Evolution of primary precipitates in a AA 3003 alloy during isothermal holdings," *Aluminium*, vol. 80, pp. 619–623, 2004.
- [21] M. Cieslar, M. Slámová, J. Uhlř, C. Coupeau, and J. Bonneville, "Effect of composition and work hardening on solid solution decomposition in twin-roll cast Al-Mn sheets," *Kovové Materiály*, vol. 45, pp. 91–98, 2007.
- [22] M. Cieslar, M. Slámová, M. Hájek, and J. Veselý, "Effect of Thermomechanical Pretreatment on Mechanical Properties of Modified Al-Mn-Fe-Si Based Alloys," *Materials Science Forum*, vol. 567-568, pp. 325–328, 2008.
- [23] Y. J. Li, A. M. F. Muggerund, A. Olsen, and T. Furu, "Precipitation of partially coherent α -Al(Mn,Fe)Si dispersoids and their strengthening effect in AA 3003 alloy," *Acta Materialia*, vol. 60, pp. 1004–1014, 2012.
- [24] S. G. Shabestari, "The effect of iron and manganese on the formation of intermetallic compounds in aluminium-silicon alloys," *Materials Science and Engineering A*, vol. 383, pp. 289–298, 2004.
- [25] M. Karlík, T. Mánik, and H. Lauschman, "Influence of Si and Fe on the distribution of intermetallic compounds in twin-roll cast Al-Mn-Zr alloys," *Journal of Alloys and Compounds*, vol. 515, pp. 108–113, 2012.
- [26] M. Dehmas, P. Archambault, M. Serriere, E. Gautier, and C. A. Gandin, "In situ precipitation in the Al-Mn-Fe-Si alloy during homogenization treatment," *Aluminium*, vol. 78, pp. 864–869, 2002.

- [27] V. Hansen, J. Gjonnes, and B. Andersson, “Quasicrystals as part of the precipitation sequence in an industrially cast aluminium alloy,” *Materials Science Letters*, vol. 8, pp. 823–826, 1989.
- [28] D. L. Sun, S. B. Kang, and H. S. Koo, “Characterization of morphology and crystal structure of α -phase in two Al-Mn-Mg alloys,” *Materials Chemistry and Physics*, vol. 63, pp. 37–43, 2000.
- [29] W. Liu and B. Radhakrishnan, “Recrystallization behavior of a supersaturated Al-Mn alloy,” *Materials Letters*, vol. 64, pp. 1829–1832, 2010.
- [30] Y. Birol, “Response to annealing treatment of a twin-roll cast thin AlFeMn-Si strip,” *Journal of Materials Processing Technology*, vol. 209, pp. 506–510, 2009.
- [31] Y. Birol and S. Kasman, “Friction stir welding of twin-roll cast EN AW 3003 plates,” *Metals and Materials International*, vol. 19, pp. 1259–1266, 2013.
- [32] S. Tierce, N. Pebere, C. Blanc, C. Casenave, G. Mankowski, and H. Robidou, “Corrosion behaviour of brazed multilayer material AA4343/AA3003/AA4343: Influence of coolant parameters,” *Corrosion Science*, vol. 49, pp. 4581–4593, 2007.
- [33] J. Lacaze, S. Tierce, M.-C. Lafont, Y. Trebault, N. Pebere, G. Mankowski, C. Blanc, H. Robidou, D. Vaumousse, and D. Daloz, “Study of the microstructure resulting from brazed aluminium materials used in heat exchangers,” *Material Science and Engineering A*, vol. 413-414, pp. 317–321, 2005.
- [34] M. Slámová, M. Karlík, M. Cieslar, B. Chalupa, and P. Merle, “Structure Transformation during Annealing of Twin-roll Cast Al-Fe-Mn-Si (AA8006) Alloy Sheets I. Effect of Cold Rolling and Heating Rate,” *Kovové Materiály*, vol. 40, pp. 389–400, 2002.
- [35] ———, “Structure Transformation during Annealing of Twin-roll Cast Al-Fe-Mn-Si (AA8006) Alloy Sheets II. Effect of Homogenization and Heating Rate,” *Kovové Materiály*, vol. 41, pp. 51–62, 2003.
- [36] F. Khakbaz and M. Kazeminezhad, “Work hardening and mechanical properties of severely deformed AA3003 by constrained groove pressing,” *Journal of Manufacturing Processes*, vol. 14, pp. 20–25, 2012.
- [37] ———, “Strain Rate Sensitivity and Fracture Behavior of Severely Deformed Al-Mn Alloy Sheets,” *Materials Science and Engineering A*, vol. 532, pp. 26–30, 2012.
- [38] K. X. Wei, W. Wei, Q. B. Du, and J. Hu, “Microstructure and Tensile Properties of Al-Mn Alloys Processed by Accumulative Roll Bonding,” *Materials Science and Engineering A*, vol. 525, pp. 55–59, 2009.
- [39] J. Veselý, “Disperzní částice v hliníkových slitinách,” Master’s thesis, Charles University in Prague, 2006.

- [40] P. Lukáš, “Studium rozdělení disperzních částic v nerovnovázně utužených hliníkových slitinách,” Master’s thesis, Charles University in Prague, 2009.
- [41] I. Nikulin, A. Kipelova, S. Malopheyev, and R. Kaibyshev, “Effect of Second Phase Particles on Grain Refinement During Equal-channel Angular Pressing of an Al-Mg-Mn Alloy,” *Acta Materialia*, vol. 60, pp. 487–497, 2012.
- [42] M. V. Kral, H. R. McIntyre, and M. J. Smilie, “Identification of intermetallic phases in a eutectic Al-Si casting alloy using electron backscatter diffraction pattern analysis,” *Scripta Materialia*, vol. 51, pp. 215–219, 2004.
- [43] Y. Birol, “Interannealing twin-roll cast Al-Fe-Si strips without homogenization,” *Scripta Materialia*, vol. 61, pp. 185–188, 2009.
- [44] N. Wang, J. E. Flato, Y. Li, and K. Marthinsen, “Evolution in microstructure and mechanical properties during back-annealing of AlMnFeSi alloy,” *Transactions of nonferrous Metals Society of China*, vol. 22, pp. 1878–1883, 2012.
- [45] M. Vlach, I. Stulikova, B. Smola, J. Piesova, H. Cisarova, S. Danis, J. Plasek, R. Gemma, D. Tanprayoon, and V. Neubert, “Effect of cold rolling on precipitation processes in Al-Mn-Sc-Zr alloy,” *Materials Science and Engineering A*, vol. 548, pp. 27–32, 2012.
- [46] M. M. R. Jaradeh and T. Carlberg, “Solidification studies of 3003 aluminium alloys with Cu and Zr additions,” *Journal of Materials Science & Technology*, vol. 27, pp. 615–627, 2011.
- [47] A. M. Zahkarov, I. T. Guldin, A. A. Arnold, and Y. A. Matsenko, “Phase Diagram of the Al-Si-Fe-Mn System in the 10-14% Si, 0-3% Fe, and 0-4% Mn Concentration Range,” *Metally*, vol. 4, pp. 214–218, 1989.
- [48] C. Gras, M. Meredith, and J. D. Hunt, “Microdefects formation during the twin-roll casting of Al-Mg-Mn aluminium alloys,” *Journal of Materials Processing Technology*, vol. 167, pp. 62–72, 2005.
- [49] Y. Birol, “Thermomechanical processing of a twin-roll cast Al-1Fe-0.2Si alloy,” *Journal of Materials Processing Technology*, vol. 202, pp. 564–568, 2008.
- [50] T. Gao, Y. Wu, C. Li, and X. Liu, “Morphologies and Growth Mechanisms of α -Al(FeMn)Si in Al-Si-Fe-Mn Alloy,” *Materials Letters*, vol. 110, pp. 191–194, 2013.
- [51] A. M. F. Muggerud, Y. Li, and R. Holmestad, “Orientation studies of α -Al(Fe,Mn)Si dispersoids in 3xxx Al alloys,” *Materials Science Forum*, vol. 794-796, pp. 39–44, 2014.
- [52] J. Chen, W. J. Poole, and N. C. Parson, “The effect of homogenization conditions on extrusion texture and microstructure evolution in AA3003,” *Materials Science Forum*, vol. 794-796, pp. 1127–1132, 2014.

- [53] M. Yoshino, S. Iwao, and M. Edo, “Recrystallization behavior of twin-roll cast 3xxx series aluminium alloy,” *Materials Science Forum*, vol. 794-796, pp. 1257–1262, 2014.
- [54] H. Ahmed, J. Kadali, K. Gatenby, and A. Howells, “The development of a brazing sheet core alloy with excellent post braze properties,” *Materials Science Forum*, vol. 794-796, pp. 1103–1108, 2014.
- [55] H.-W. Huang, B.-L. Ou, and C.-T. Tsai, “Effect of Homogenization on Recrystallization and Precipitation Behavior of 3003 Aluminum Alloy,” *Materials Transactions*, vol. 49, pp. 250–259, 2008.
- [56] W. Wu, X. Zhang, D. Sun, G. Hu, and G. Liu, “Microstructural evolution of aluminium alloy 3003 during annealing,” *Transactions of Nonferrous Metals Society of China*, vol. 16, pp. 1309–1313, 2006.
- [57] V. Očenášek, P. Homola, M. Kolář, J. Uhlíř, and M. Cieslar, “Effect of Sc and Zr on the structure and properties of Al-Mn1.5 alloy,” in *Metal 2009 Conference Proceedings*. Tanger spol. s r. o., 2009, pp. 91–98.
- [58] Y. S. Sato, M. Urata, H. Kokawa, and K. Ikeda, “Hall-Petch relationship in fraction stir welds of equal channel angular-pressed aluminium alloys,” *Materials Science and Engineering A*, vol. 354, pp. 298–305, 2003.
- [59] N. Sun, B. R. Patterson, J. P. Suni, E. A. Simielli, H. Weiland, and L. F. Allard, “Microstructural evolution in twin roll cast AA3105 during homogenization,” *Materials Science and Engineering A*, vol. 416, pp. 232–239, 2006.
- [60] P. Kratochvíl, P. Lukáč, and B. Sprušil, *Úvod do fyziky kovů I*, 1st ed. Praha: SNTL, 1984.
- [61] A. Lens, C. Maurice, and J. H. Driver, “Grain boundary mobilities during recrystallization of Al-Mn alloys as measured by in situ annealing experiments,” *Materials Science and Engineering A*, vol. 403, pp. 144–153, 2005.
- [62] H.-W. Huang and B.-L. Ou, “Evolution of precipitation during different homogenization treatments in a 3003 aluminum alloy,” *Materials and Design*, vol. 30, pp. 2685–2692, 2009.
- [63] O. Engler, “On the Influence of Dispersoids on the Particle Stimulated Nucleation of Recrystallization in an Al-Fe-Si Model Alloy,” *Materials Science Forum*, vol. 273-275, pp. 483–488, 1998.
- [64] Y. Birol, “Recrystallization of a supersaturated Al-Mn alloy,” *Scripta Materialia*, vol. 59, pp. 611–614, 2008.
- [65] B. Benum and E. Nes, “Effect of Precipitation on the Evolution of Cube Recrystallization Texture,” *Acta Materialia*, vol. 45, pp. 4593–4602, 1997.
- [66] M. Poková, M. Cieslar, and M. Slámová, “The influence of dispersoids on the recrystallization of aluminium alloys,” *International Journal of Materials Research*, vol. 100, pp. 391–394, 2009.

- [67] M. Slámová, J. Politello, and M. Cieslar, “Effect of iron content on the structural transformations in Al-Mn-Fe-Si twin-roll cast alloys during annealing,” in *Aluminium Alloys: Their Physical and Mechanical Properties*, J. Hirsch, G. Gottstein, and B. Skrotzki, Eds., no. 1, Aachen, Germany, 2008, pp. 555–560.
- [68] P. Málek, M. Cieslar, and V. Očenášek, “Deformation Behaviour of the Al-Mn-Sc-Zr Alloy Produced Using ECAP,” in *Metal 2010 Conference Proceedings*. Rožnov pod Radhoštěm: Tanger, 2010, ISBN 978-80-87294-15-4.
- [69] H.-E. Ekström, S. Tangen, O. V. Mishin, and L. Östensson, “The Softening of a Dispersoid-Rich Commercial Al-Mn Alloy,” *Materials Science Forum*, vol. 550, pp. 351–356, 2007.
- [70] M. Slámová, V. Očenášek, and V. V. Voort, “Polarized light microscopy: utilization in the investigation of the recrystallization of aluminium alloys,” *Materials Characterization*, vol. 52, pp. 165–177, 2004.
- [71] G. Gottstein and L. S. Shvindlerman, *Grain Boundary Migration in Metals*, 2nd ed. New York: CRC Press, 2010.
- [72] B. Forbord, H. Hallem, N. Ryum, and K. Marthinsen, “Precipitation and recrystallization in Al-Mn-Zr with and without Sc,” *Materials Science and Engineering A*, vol. 387-389, pp. 936–939, 2004.
- [73] H. Jazarei and F. J. Humphreys, “The Transition from Discontinuous to Continuous Recrystallization in Some Aluminium Alloys II – Annealing Behaviour,” *Acta Materialia*, vol. 52, pp. 3251–3262, 2004.
- [74] F. J. Humphreys, “A Unified Theory of Recovery, Recrystallization and Grain Growth, Based on the Stability and Growth of Cellular Microstructures–I. The Basic Model,” *Acta Materialia*, vol. 45, pp. 4231–4240, 1997.
- [75] —, “A Unified Theory of Recovery, Recrystallization and Grain Growth, Based on the Stability and Growth of Cellular Microstructures–II. The Effect of Second Phase Partilces,” *Acta Materialia*, vol. 45, pp. 5031–5039, 1997.
- [76] H. G. Kang, J. P. Lee, M. Y. Huh, and O. Engler, “Stability against coarsening in ultra-fine grained aluminum alloy AA 3103 sheet fabricated by continuous confined strip sheering,” *Materials Science and Engineering A*, vol. 486, pp. 470–480, 2008.
- [77] S. P. Chen, A. Miroux, and S. Zwaag, “Influence of concurrent precipitation on the nucleation kinetics during recrystallization in AA3003,” *Materials Science Forum*, vol. 519-521, pp. 1605–1610, 2006.
- [78] R. D. Doherty, D. A. Hughes, F. J. Humphreys, J. J. Jonas, D. J. Jensen, M. E. Kassner, W. E. King, T. R. McNelley, H. J. McQueen, and A. D. Rollett, “Current issues in recrystallization: a review,” *Materials Science and Engineering A*, vol. 238, pp. 219–274, 1997.

- [79] Y. Birol, “Impact of homogenization on recrystallization of a supersaturated Al-Mn alloy,” *Scripta Materialia*, vol. 60, pp. 5–8, 2009.
- [80] J. J. Nah, H. G. Kang, M. Y. Huh, and O. Engler, “Effect of strain states during cold rolling on the recrystallized grain size in an aluminum alloy,” *Scripta Materialia*, vol. 58, pp. 500–503, 2008.
- [81] E. Nes and H. Billdal, “Non-equilibrium solidification of hyperperitectic Al-Zr alloys,” *Acta Metallurgica*, vol. 25, pp. 1031–1037, 1977.
- [82] K. S. Vecchio and D. B. Williams, “Convergent beam electron diffraction study of Al_3Zr in Al-Zr and Al-Li-Zr alloys,” *Acta Metallurgica*, vol. 35, pp. 2959–2970, 1987.
- [83] K. E. Knipling, D. C. Dunand, and D. N. Seidman, “Precipitation evolution in Al-Zr and Al-Zr-Ti alloys during aging at 450–600 °C,” *Acta Materialia*, vol. 56, pp. 1182–1195, 2008.
- [84] N. Ryum, “Precipitation and Recrystallization in an Al-0.5 wt.% Zr-Alloy,” *Acta Metallurgica*, vol. 17, pp. 269–278, 1969.
- [85] S. Ceresara, M. Conserva, and P. Fiorini, “Recovery and Recrystallization of an Al-0.18 wt.% Zr Alloy Cold Worked at -196 °C,” *Materials Science and Engineering*, vol. 9, pp. 19–22, 1972.
- [86] E. Nes and S. Slevolden, “Mechanical properties of new strip-cast AlMnZr alloys,” *Aluminium*, vol. 55, pp. 398–400, 1979.
- [87] K. E. Knipling, D. C. Dunand, and D. N. Seidman, “Precipitation evolution in Al-Zr and Al-Zr-Ti alloys during isothermal aging at 375–425 °C,” *Acta Materialia*, vol. 56, pp. 114–127, 2008.
- [88] Z. Jia, G. Hu, B. Forbord, and J. K. Solberg, “Effect of homogenization and alloying elements on recrystallization resistance of Al-Zr-Mn alloys,” *Materials Science and Engineering A*, vol. 444, pp. 284–290, 2007.
- [89] Z. Jia, G. Hu, B. Forbord, and J. K. Solberg, “Enhancement of recrystallization resistance of Al-Zr-Mn by two-step precipitation annealing,” *Materials Science and Engineering A*, vol. 483–484, pp. 195–198, 2008.
- [90] M. Karlík, M. Slámová, and T. Mánik, “Influence of Fe and Si on the microstructure of the Al-Mn alloy with Zr addition,” *Kovové Materiály*, vol. 47, pp. 139–146, 2009.
- [91] D. Jiang, J. Ning, J. Sun, Z. Hu, and Y. Hou, “Annealing Behavior of Al-Mg-Mn Alloy Processed by ECAP at Elevated Temperature,” *Transaction of Nonferrous Metals Society of China*, vol. 18, pp. 248–254, 2008.
- [92] T. Sato, A. Kamio, and G. Lorimer, “Effects of Si and Ti additions on the nucleation and phase stability of the L_{12} -type Al_3Zr phase in Al-Zr alloys,” *Materials Science Forum*, vol. 217–222, pp. 895–900, 1996.

- [93] H. Weiland and S. Cheong, “The Role of Zirconium Additions in Recrystallization of Aluminium Alloys,” *Materials Science Forum*, vol. 558-559, pp. 383–387, 2007.
- [94] SGTE, “Alloy Phase Diagrams,” [online], cited 12/5/2011, revised 2004, <http://www.crct.polymtl.ca/fact/documentation/sgte/>.
- [95] P. Furrer and H. Warlimont, “Crystalline and Amorphous Structures of Rapidly Solidified Al-Cr Alloys,” *Materials Science and Engineering*, vol. 28, pp. 127–137, 1977.
- [96] M. J. Cooper, “The structure of the intermetallic phase Θ (Cr-Al),” *Acta Crystallographica*, vol. 13, pp. 257–263, 1960.
- [97] M. Audier, M. Durand-Charre, E. Laclau, and H. Klein, “Phase equilibria in the Al-Cr system,” *Journal of Alloys and Compounds*, vol. 220, pp. 255–230, 1995.
- [98] T. Ohnishi, Y. Nakatani, and K. Okabayashi, “Crystal Structures of Intermetallic h, g and e Phases in Al-Cr System,” *Bulletin of University of Osaka Prefecture. Series A*, vol. 24, pp. 183–191, 1975.
- [99] Y. Liang, C. Guo, C. Li, and Z. Du, “Thermodynamic modeling of the Al-Cr system,” *Journal of Alloys and Compounds*, vol. 460, pp. 314–319, 2008.
- [100] X. M. Li and M. J. Starink, “Identification and analysis of intermetallic phases in overaged Zr-containing and Cr-containing Al-Zn-Mg-Cu alloys,” *Journal of Alloys and Compounds*, vol. 509, pp. 471–476, 2011.
- [101] P. Tezcan and H. Jones, “The effect of alloy composition on the hardness and ageing response of rapidly solidified Al-Cr-Zr-Mn alloy powder particulate,” *Materials Letters*, vol. 10, pp. 231–234, 1990.
- [102] T. Schenk, M. Durand-Charre, and M. Audier, “Liquid-solid equilibria in the Al-rich corner of the Al-Mn-Cr system,” *Journal of Alloys and Compounds*, vol. 281, pp. 249–263, 1998.
- [103] L. Lodgaard and N. Ryum, “Precipitation of dispersoids containing Mn and/or Cr in Al-Mg-Si alloys,” *Materials Science and Engineering A*, vol. 283, pp. 144–152, 2000.
- [104] R. A. Jeniski, “Effects of Cr addition on the microstructure and mechanical behaviour of 6061-T6 continuously cast and rolled redraw rod,” *Materials Science and Engineering A*, vol. 237, pp. 52–64, 1997.
- [105] G. Timelli and F. Bonollo, “The influence of Cr content on the microstructure and mechanical properties of AlSi9Cu3(Fe) die-casting alloys,” *Materials Science and Engineering A*, vol. 528, pp. 273–282, 2010.
- [106] W. C. Liu, T. Zhai, and J. G. Morris, “Texture evolution of continuous cast and direct chill cast AA 3003 aluminum alloys during cold rolling,” *Scripta Materialia*, vol. 51, pp. 83–88, 2004.

- [107] C. Gras, M. Meredith, and J. D. Hunt, “Microstructure and texture evolution after twin roll casting and subsequent cold rolling of Al-Mg-Mn aluminium alloys,” *Journal of Materials Processing Technology*, vol. 169, pp. 156–163, 2005.
- [108] Y. Birol, “Analysis of macro segregation in twin-roll cast aluminium strips via solidification curves,” *Journal of Alloys and Compounds*, vol. 486, pp. 168–172, 2009.
- [109] A. Kawahara, A. Niikura, and T. Doko, “Development of Aluminum Alloy Fin Stock for Heat Exchangers Using Twin-Roll Continuous Casting Method,” *Furukawa Review*, vol. 24, pp. 81–87, 2003.
- [110] M. Yun, S. Lokyer, and J. D. Hunt, “Twin roll casting of aluminium alloys,” *Materials Science and Engineering A*, vol. 280, pp. 116–123, 2000.
- [111] Y. Iwahashi, Z. Horita, M. Nemoto, and T. G. Langdon, “An Investigation of Microstructural Evolution During Equal-Channel Angular Pressing,” *Acta Materialia*, vol. 45, pp. 4733–4741, 1997.
- [112] V. M. Segal, “Materials processing by simple shear,” *Materials Science and Engineering A*, vol. 1995, pp. 157–164, 197.
- [113] K. Nakashima, Z. Horita, M. Nemoto, and T. G. Langdon, “Development of a multi-pass facility for equal-channel angular pressing to high total strain,” *Materials Science and Engineering A*, vol. 281, pp. 82–87, 2000.
- [114] Y. Iwahashi, Z. Horita, M. Nemoto, and T. G. Langdon, “The Process of Grain Refinement in Equal-Channel Angular Pressing,” *Acta Materialia*, vol. 46, pp. 3317–3331, 1997.
- [115] I. Sabirov, M. Y. Murashkin, and R. Z. Valiev, “Nanostructured aluminium alloys produced by severe plastic deformation: New horizons in development,” *Materials Science and Engineering A*, vol. 560, pp. 1–24, 2013.
- [116] Z. Horita, T. Fujinami, M. Nemoto, and T. G. Langdon, “Improvement of mechanical Properties for Al Alloys using Equal-channel Angular Pressing,” *Journal of materials Processing Technology*, vol. 117, pp. 288–292, 2001.
- [117] K. Turba, P. Málek, and M. Cieslar, “Superplasticity in a Zr and Sc Modified AA7075 Aluminium Alloy Produced by ECAP,” *Kovové Materiály*, vol. 45, pp. 165–170, 2007.
- [118] K. Dám, P. Lejček, and A. Michalcová, “In situ TEM investigation of microstructural behavior of superplastic Al-Mg-Sc alloy,” *Materials Characterization*, vol. 76, pp. 69–75, 2013.
- [119] P. Málek, K. Turba, and M. Cieslar, “High-temperature Deformation Characteristics of ECAP Al-based Alloys Stabilized by Sc+Zr,” in *Nanocon 2010 Conference Proceedings*. Tanger spol. s r. o., 2010, pp. 523–528.

- [120] A. B. Naizabekov, V. A. Andreyachshenko, and R. Kocich, “Study of deformation behavior, structure and mechanical properties of the AlSiMnFe alloy during ECAP-PBP,” *Micron*, vol. 44, pp. 210–217, 2013.
- [121] J. L. Ning, D. M. Jiang, X. G. Fan, Z. H. Lai, Q. C. Meng, and D. L. Wang, “Mechanical properties and Microstructure of Al-Mg-Mn-Zr Alloy Processed by Equal Channel Angular Pressing at Elevated Temperature,” *Materials Characterization*, vol. 59, pp. 306–311, 2008.
- [122] J. L. Ning and D. M. Jiang, “Influence of Zr addition on the microstructure evolution and thermal stability of Al-Mg-Mn alloy processed by ECAP at elevated temperature,” *Materials Science and Engineering A*, vol. 452-453, pp. 552–557, 2007.
- [123] P. Málek and M. Cieslar, “The influence of processing route on the plastic deformation of Al–Zn–Mg–Cu alloys,” *Materials Science and Engineering A*, vol. 324, pp. 90–95, 2002.
- [124] M. Hájek, J. Veselý, and M. Cieslar, “Precision of electrical resistivity measurements,” *Materials Science and Engineering A*, vol. 462, pp. 339–342, 2007.
- [125] EDAX, “TLS OIM Analysis,” [software], cited 12/3/2014, version 6.
- [126] K. Turba, P. Málek, E. F. Rauch, and M. Cieslar, “High strain rate superplasticity in a Zr and Sc modified 7075 aluminum alloy produced by ECAP,” *Material Science Forum*, vol. 584-586, pp. 164–169, 2008.
- [127] P. Málek and M. Cieslar, “Microstructure and deformation behaviour of the ECAP Al-Mn-Sc-Zr alloy,” *Kovové Materiály*, p. In press, 2014.
- [128] X. Huang, N. Hansen, and N. Tsuji, “Hardening by Annealing and Softening by Deformation in Nanostructured Metals,” *Science*, vol. 312, pp. 249–251, 2006.
- [129] X. Huang, N. Kamikawa, and N. Hasen, “Strengthening mechanism in nanostructured aluminium,” *Materials Science and Engineering A*, vol. 483-484, pp. 102–104, 2008.

A. DVD content

Part of this work are videos from in-situ heating in transmission electron microscope. All samples were isochronally annealed with step 50 °C/50 min. The videos can be found on the enclosed DVD.

Following materials were subjected to in-situ heating:

- Dinit = alloy C470, as-cast
- D1P = alloy C470, after 1 ECAP pass
- D4P = alloy C470, after 4 ECAP passes
- DZ4P = alloy C470, annealed with heating rate 0.5 K/min to 450 °C + 8 h/450 °C, 4 ECAP passes
- AZ4P = alloy C412, annealed with heating rate 0.5 K/min to 450 °C + 8 h/450 °C, 4 ECAP passes

Corresponding images from in-situ heating are on pages 80 and 106 and in the Figures.pdf file.

Further on the DVD:

- Pokova-PhD.pdf – Text of the thesis.
- Figures.pdf – Supplementary figures and charts.